UNIVERSITY OF SOUTHAMPTON

Fabrication of Deep UV Laser Written Integrated Devices for Quantum Technology

by

Qazi Salman Ahmed

ORCID: 0000-0003-0731-5390

Supervisors: Dr James Gates, Dr Paul Gow and Prof. Peter G.R. Smith

A thesis submitted in partial fulfillment for the degree of Doctor of Philosophy

in the
Faculty of Engineering and Physical Science
Optoelectronics Research Centre

18/07/23

UNIVERSITY OF SOUTHAMPTON

ABSTRACT

FACULTY OF ENGINEERING AND PHYSICAL SCIENCE
OPTOELECTRONICS RESEARCH CENTRE

Doctor of Philosophy

by Qazi Salman Ahmed

ORCID: 0000-0003-0731-5390
Supervisors: Dr James Gates, Dr Paul Gow and Prof. Peter G.R. Smith

The interest in quantum technologies has gained tremendous scientific attention due to their potential applications in quantum information processing, and sensing. Previous studies on quantum science primarily focused on utilising many laser beams and bulk optics, which makes optical setups sensitive to vibrations and limit scalability. Recently, integrated optics have shown promise in increasing the scalability and portability of many existing quantum optical systems. This work recognises blazed gratings on an integrated platform as a viable method to generate integrated large-scale (mm) free-space beams. We propose a design and fabrication route for an integrated and portable device using small spot direct UV writing to deliver free-space beams for quantum technology.

Extensive system calibration and characterisation of the pulsed 213 nm laser in small spot direct UV writing is provided. The waveguides and gratings were fabricated in planar silica, with and without hydrogen loading. A new UV fabrication approach is developed, where UV radiative fluence builds up in multiple passes. The technique suggested that the photosensitivity and grating strength can be substantially improved using the multi-pass writing technique. This writing technique is crucial for inscribing larger and more complex devices, providing a robust photosensitive platform via pre-exposure, and minimising the artefacts associated with hydrogen out-gassing and the stability of the interferometer.

The writing dynamics of the pulsed 213 nm laser are investigated in detail, including the non-typical effects of writing power and fluence on the induced effective change in the refractive index and grating strength. Suitable writing regimes (avoiding damage) are identified where the photosensitivity mechanism is dominant by photochemical changes.

Furthermore, a state-of-the-art fabrication system is introduced to develop large-area out-of-plane blazed grating couplers. This is the first example of a holographically fabricated grating coupler to provide large-scale (mm) free-space beams. The fabricated device produces a large-area (4.4 mm $\times$ 3.9 mm) free-space beam with dimensions significantly larger than those obtained from etched grating couplers. The coupling efficiency (fibre to free space) of the device was less than 1%. However, the fabricated device was the first prototype, and its efficiency can be significantly enhanced with several improvements in the fabrication process.

Declaration of Authorship

I, Q. Salman Ahmed, declare that this thesis, 'Fabrication of Deep UV Laser Written Integrated Devices for Quantum Technology' and the work presented in it is my own and has been generated by me as the result of my original research.

I confirm that:

- This work was done wholly or mainly while in candidature for a research degree at this University
- Where any part of this thesis has previously been submitted for a degree or any other qualification at this University or any other institution, this has been clearly stated
- Where I have consulted the published work of others, this is always clearly attributed
- Where I have quoted from the work of others, the source is always given. Except for such quotations, this thesis is entirely my work;
- I have acknowledged all main sources of help. Where the thesis is based on work done by myself jointly with others, I have made clear exactly what was done by others and what I have contributed myself
- Parts of this work have been published. A list of publications is provided in Appendix 2.

Signed:

Date: 18/07/23

Acknowledgements

While this thesis bears my name on the front, I would like to express my gratitude to the many people who have supported me along the way.

First and foremost, I would like to thank James Gates for his unwavering politeness, guidance and for helping me transform my ideas into coherent research. He provided valuable feedback and suggestions at every stage of my PhD, which helped to increase my scientific knowledge and develop the necessary skills to become a better scientific learner.

I am also grateful to Peter Smith for his valuable feedback on my research articles and continuous support throughout my PhD. I want to thank Corin Gawith for his generosity and encouragement throughout my studies.

I would like to express my appreciation to Paul Gow and James Field for welcoming me into their lab and being fantastic supervisors and friends.

To Paula Smith, who made my life easier, and she always was like a family to me.

To Davina for always being generous in providing administrative support.

To all the group members, both past and present, including Chris, Paolo, Rex, Shahrzad, Bruno, Glenn, Goronwy, Matt, Alex Flint, Dom, Noe, Peter Iveson, James Washak, Matt Whitaker, Charlie, Senta, Alan, Alex Jantzen, Rod, Devin, Sam, and Lewis, I am grateful for the enjoyable moments we shared and for the opportunity to work alongside you and learn from you.

I would like to thank Wanvisa, Tam, and Sergei for being lovely friends in ORC.

Special thanks to Peter Horak and Anna Peacock for addressing all project and funding issues at the beginning of my PhD.

I would also like to thank all my Pakistani friends, including Ayesha, Sohail, Tanzeela, Wajeeha, Ali, Kaif, Abouzar, and Wasif for their love, care, and beautiful memories.

To my Master's supervisors Dr Shazia, Dr Mahreen at Government College University Lahore, and Dr Faheem K. Butt at the University of Education, Lahore, Pakistan, for their countless contributions towards my success. Without their efforts, I would not have opted for a scientific career.

Finally, I must express my deepest gratitude to my Mom and Dad (Asma and Raess) and my brothers (Aneeque and Laeeque) for their unwavering support and prayers throughout my academic journey. I would not have made it this far without their unconditional love and support.

To all those who have been mentioned in these paragraphs and to those who may have been inadvertently left out, I would like to express my heartfelt gratitude for your love and friendship.

Salman Ahmed

Contents

List of Figures

List of Tables

List of acronyms

CW continous wave

EOM electro-optic modulator

DUV direct ultra-violet writing

FBG fibre Bragg gratings

FHD flame hydrolysis deposition

FWHM full-width half maximum

LBL line-by-line

NA numerical aperture

OOP out-of-plane

OSA optical spectrum analyser

PECVD plasma enhanced chemical vapour deposition

Pbp point-by-point

PBP plane-by-plane

PIC photonic integrated circuit

PM polarisation maintaining

PSO position-synchronised output

SOI silicon-on-insulator

SM single mode

SSDUW small-spot direct UV writing

TE transverse electric

THOX thermal oxide

TM transverse magnetic

Dedicated to my parents, (Asma and Raees), as well as my brothers (Aneeque and Laeeque), to whom I owe my life.

"Happiness can be found even in the darkest of times if one only remembers to turn on the light".

–Albus Dumbledore-Harry Potter and the Prisoners of Azkaban

Chapter 1

Introduction

1.1 Motivation

Previous studies on science at the quantum scale were mainly realised by using traditional bulk optics, which restricted their scalability. Within the last twenty years, development to overcome this limitation has enabled larger-scale applications of this technology in potential areas such as on-chip atomic clocks [1], and quantum sensors [2]. Compared with the traditional approach, these miniaturised devices are promising in terms of stability, compactness and robustness. Recently a promising approach to miniaturise atom trap systems has been demonstrated [3]. The presented design of a microfabricated atom chip requires laser beams independent of bulk optics for the complete portability of the system. By developing integrated grating couplers on chips, it is anticipated that these devices can be used to manufacture a fully integrated optical platform for quantum optics. Etched grating couplers are commonly used for integrated free-space beam delivery [4]. However, the stringent phase matching required in these components typically limits the dimensions of etched grating devices. Etched grating and waveguide couplers exhibit small-scale inconsistencies, which are often intensified by the high index contrast of these devices [5]. These inconsistencies can lead to effective index variations and result in phase errors across the fabricated devices. As a result, the successful size of these devices is typically restricted to a few-millimeter length.

The motivation for the current project is to develop a UV fabrication system capable of fabricating large-area grating couplers for integrated free-space beam delivery. This work will discuss a detailed investigation of the writing dynamics of the 213 nm laser source for waveguide and grating fabrication over a large parameter space provided by the UV-written flame hydrolysis deposited platform. A state-of-the-art fabrication system will be developed to inscribe out-of-plane 45° blazed gratings in planar doped silica for integrated free-space beam delivery.

We hope that our fabricated device will be utilised for quantum technology by providing a route for complete integration and portability of atom trap systems.

1.2 Platforms for integrated optics

Integrated optics is manipulating light on a micro-scale using optical components integrated onto a single substrate. Platforms for integrated optics are materials or substrates used to fabricate photonic integrated circuits (PICs). PICs use light to perform various functions, such as data communication, sensing, and signal processing. Each platform has its own set of advantages and disadvantages, and the choice of platform depends on the specific application and requirements of the device. The passive optical materials commonly used for PICs are silicon, silicon nitride, and silica.

1.2.1 Silicon

Silicon is an attractive material with excellent transmission over a wavelength range of 1.2 to 6 microns [6]. Its high refractive index allows for strong light confinement and efficient coupling between different components. Additionally, silicon is compatible with complementary metal-oxide-semiconductor (CMOS) fabrication techniques [7], meaning that integrated optical components can be manufactured using the same processes are used to create electronic circuits on silicon chips. This compatibility can lead to significant cost savings and scalability for mass production. Using a silicon-on-insulator (SOI) platform, different components such as waveguides, filters, modulators, detectors, and light sources can be integrated onto a single chip, allowing for compact and efficient optical devices [8]. These components can be designed and optimised using computer-aided design (CAD) tools and simulations, and the final devices can be fabricated using advanced lithography and etching techniques [9]. Silicon photonics has many potential applications, including in data communications [10], sensing [11], and biomedical imaging. It can potentially revolutionise data centres by enabling high-speed optical communication between servers, improving bandwidth and reducing power consumption.

1.2.2 Silicon nitride

Silicon nitride (SiN) is a well-known platform for integrated optics due to its high refractive index and transmission over the visible wavelength range (down to about 500 nm) [12], [13]. The most common components fabricated on the SiN platform include waveguides, resonators, filters, and modulators [14]. One of the key advantages of using SiN for integrated optics is its high refractive index, which allows for tighter mode confinement and enables the fabrication of high-quality, compact photonic circuits. SiN also has a low propagation loss, which results in high transmission efficiency and low noise. SiN is also compatible with CMOS processing [15], making integrating with other electronic components on the same chip easy.

1.2.3 Silica glass

SiO_2 glass is mostly used for integrated optics due to its excellent optical properties, low loss, and transparency across a wide range of wavelengths (0.2 to 4 microns for low hydroxyl content (water)) [16]. SiO_2 glass, also known as silica, is a non-crystalline material that can be fabricated using various techniques, including lithography, etching,

and film deposition. The most common components fabricated on the SiO_2 glass platform include waveguides, couplers, and filters [17]. Couplers and filters can be created using grating formation techniques. One of the key advantages of using SiO_2 glass for integrated optics is its high optical quality, which results in low loss and high transmission efficiency. SiO_2 glass also has a low coefficient of thermal expansion [18], which means it is highly stable over a wide temperature range, making it suitable for applications in harsh environments. Additionally, SiO_2 glass is biocompatible [19], making it a suitable platform for biomedical sensing and imaging applications. SiO_2 glass integrated optics is a promising platform for various applications, including telecommunications, sensing, and fibre-coupled integrated portable devices.

1.3 Prior work on out-of-plane gratings couplers

However, the following literature review briefly overviews recent work to fabricate out-of-plane grating couplers on integrated platforms (i.e. SOI, silica, and silicon nitride) to miniaturise optical systems in various research areas. This review is not exhaustive but provides an overview of current approaches. To the best of my knowledge, no significant work has been reported on fabricating a grating coupler for an atom trap system. In atom traps, the trapping region is typically created using magnetic or optical fields, which confine the atoms in a small volume of space. The beam dimensions of atom traps can vary depending on the specific configuration of the trap, but they are typically on the order of a few millimeters to a few centimeters. In ion traps, on the other hand, the trapping region is created by applying a combination of electric and magnetic fields to confine ions in a specific location. The beam dimensions of ion traps are typically much smaller than those of atom traps, typically on the order of micrometers. Below, I will provide a summary of work on grating couplers for various applications (i.e. integration of ion trap, biomedical detection and telecommunication).

Mehta *et al.* [20] have demonstrated an ion trap design based on lithographically defined nanophotonic waveguide for guiding light and Sr^+ ions addressing that are integrated within an ion trap chip. The waveguides were fabricated with a cross-section area of 120×540 nm^2 on a quartz substrate in a SiN film for single mode operation at $\lambda = 674$ nm with a TE polarisation. In their proposed design, light from the waveguide was coupled to free space via grating couplers. Ions were addressed at multiple locations by using grating couplers; these focus through trap electrodes to ions trapped 50 µm above the chip. Using grating couplers, the light was focused out with a $1/e^2$ radius of 2 µm.

The same group has also presented a compact design methodology and characterisation of grating couplers to focus beam out of plane [21].The designed structure is again targeted at 674 nm wavelength and fabricated in Si_3N_4. In their fabricated designs, the electric field of the coupled light was tailored via the control of the local grating period and the duty cycle which collectively define the angle of emitted beam and the diffraction efficiency. The characterisation to estimate the beam dimension coupling out of the waveguide was performed at a height of 50 µm. Gaussian fits were applied to extract the $1/e^2$ beam waist of 2 µm in the x-axis and 2.3 µm in the y-axis.

Becker *et al.* [22] have proposed and demonstrated a design of an integrated waveguide and gratings which couples 1550 nm light from single mode waveguide to free space. In this work, they have demonstrated one-dimensional focusing grating coupler to couple

linearly polarised light out of the plane. Later, their design was extended to 2-D grating structures based on phase-matching conditions using two separate input optical ports. The main idea behind the designed methodology was to launch a TE polarised light through two different input ports and, by using resistive heaters, thermally controlling the relative phase so that resulting outcoupled beams were circularly polarised. In experimental characterisation, uniform and circular focusing beams were coupled out with $1/e^2$ diameter of 2.3 µm along the x-axis and 2.1 µm in the y-axis at focus.

Kim *et al.* [4] have demonstrated an integrated design for a SiN grating coupler to provide a free space beam coupling out of the plane. Their design consists of an extreme mode converter providing the interface with the photonic mode in the waveguide and the free space beam (see Fig. 1.3 taken from [4]). In the first step, a mode expander was fabricated to convert the channel waveguide mode to slab mode via evanescent coupling. In the second step, large grating lines with an apodisation profile were fabricated to couple the slab mode into a free-space collimated beam, as shown in the Fig. 1.3 . The mode profiling showed a Gaussian beam with a beam waist of 160 µm in both x- and y-axis coupled out of the device into free space. The same research group has presented a modified scheme [23] where Si metasurfaces were used on the top of the etched grating footprint to focus light at 475 nm spot size.

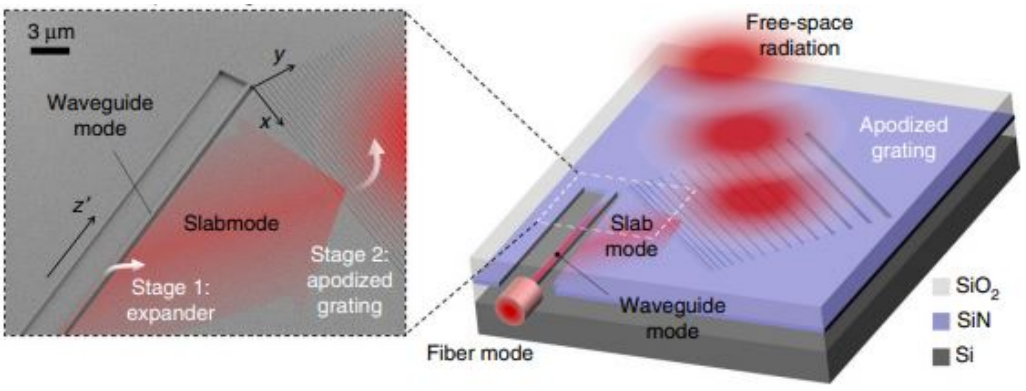

FIGURE 1.1: Schematic of an integrated grating coupler to provide a free space beam (taken from [4]).

Kerman et al. [24] investigated an integrated SiN photonics circuit that could excite and collect fluorescence from microparticles flowing in a microfluidic channel over the photonics circuit. The structure comprised of one focusing grating coupler (FGC) for fluorescence excitation and three other FGCs for collection. The focused spot of FGCs was measured experimentally to be 0.75 µm × 3.64 µm in the vertical plane, comparable to the spot size of a 0.33 NA objective. This structure successfully detected polystyrene particles of 1 and 15 µm. The maximum system collection efficiency was inversely proportional to the size of the particle due to the small detection volume. The in-line collection FGC had a system collection efficiency of 0.088%, 0.010%, and 0.033% for 1 and 15 µm particles.

Van et al. [25] presented experimental results for compact and broadband FGCs in silicon-on-insulator (SOI) and gold on SOI. The coupling structure in SOI achieves an eight-fold length reduction from fibre to photonic wire compared to a linear grating and adiabatic taper without any performance penalty. They have also demonstrated a focusing grating coupler in gold on SOI, which achieves 20% fibre-to-focus efficiency.

Source	Application	Fabrication	Targeted wavelength (nm)	Platform	Beam / footprint size	Coupling efficiency/loss
[20]	Integrated ion trap	Etched gratings	674	SiN	2 µm beam	losses=33 dB
[21]	Integrated ion trap	Etched gratings	674	Si_3N_4	2.3 µm beam	70±15 %
[22]	Magneto-resistive random access memory	Etched gratings	1550	Si-on-insulator	2.3 µm beam	-13.7 dB
[4]	Miniaturisation of hybrid devices	Etched gratings	780	SiN	160 µm beam	Coupling loss $\lesssim$ 4.5 dB
[23]	Miniaturisation of hybrid devices	Integrated metasurfaces on etched gratings	780	SiN with SiO_2 clad for an extreme mode converter and Si metasurface on SiO_2 for focusing	200 µm collimated, 473 nm focused spot	Coupling loss $\lesssim$ 6.4 dB
[24]	Bio-medical detection	Etched gratings	638	SiN	0.75 × 3.64 µm focused spot	0.033 %
[26]	Miniaturised integration	364 nm UV holographic recording	632	fused silica	10.49 µm focused spot	95 %
[27]	Out-of-plane beam delivery	364 nm UV holographic recording	850	substrate BK-7 glass, Summers Optical cement J-91 waveguide, and Omnidex HRF600 photopolymer	3.32 µm focused spot	92.9 %
[25]	Miniaturised footprint for beam delivery	Etched gratings	1550	silicon-on-insulator (SOI) and gold on SOI	18.5 × 28 µm footprint	20 %

TABLE 1.1: Summary of previous work related to the fabrication of grating couplers and resultant out-coupled beam specifications.

Schultz et al. [26] designed, fabricated and characterised a volume grating focusing waveguide coupler. The purpose of the volume grating was to preferentially couple a 633 nm light in a single-mode polyimide waveguide into the air cover. The beam was outcoupled perpendicular to the surface of the waveguide and focused to a line 25 mm above the waveguide. The slanted-fringe volume grating was holographically recorded by dual-beam interferometry using a coherent 364-nm UV laser, focused with a cylindrical lens to produce the chirped grating. The 1-mm-long volume grating coupler exhibited a coupling efficiency of 95% and an almost diffraction-limited focused spot with an FWHM of 10.49 µm. The same group has also presented a volume grating focusing waveguide coupler [27] to couple 850 nm wavelength with a 92.9% coupling efficiency. From a 1000 µm grating coupler, they managed to get a focused spot of 3.32 µm, 4 mm above the grating.

Most of the grating-based devices discussed above were fabricated using conventional lithography and etching to form both the waveguide and grating structures and provide a free space beam with µm dimensions. A summary of the above-reported work is given in Table 1.1. Etched grating components typically require a precise definition of the waveguide dimensions and the grating period – demanding extremely high fabrication accuracy. Variation in the waveguide thickness and grating period due to fabrication inconsistencies and etching process leads to phase errors across the fabricated devices [5]. These typically restrict the size of successful devices to a few-millimetre length. To overcome this limitation, the current work will present the fabrication of large-area grating couplers by UV writing for an integrated ($\sim$ 10 mm) large beam delivery. Here we propose a geometry for a UV-written gratings coupler to integrate with an atom trap chip. The proposed scheme uses a fibre pigtail to launch a 780 nm laser source into a planar waveguide which contains grating couplers to couple the light out of the plane (see Fig.1.2). The complete specifications of the device are given in Table 1.2. We expect a low index contrast with better phase stability in UV-written devices than etched grating couplers. It is hoped that our device can provide a route to increasing the scalability of the next-generation optical components for quantum technology.

Parameter	**Requirement**
Beam profile	Ideally Gaussian
Beam diameter	10 mm
Launch	Fibre coupled
Launch fibre type	PM-780 nm
Polarisation	Linear

TABLE 1.2: Specifications for a device for integration for atom trap system.

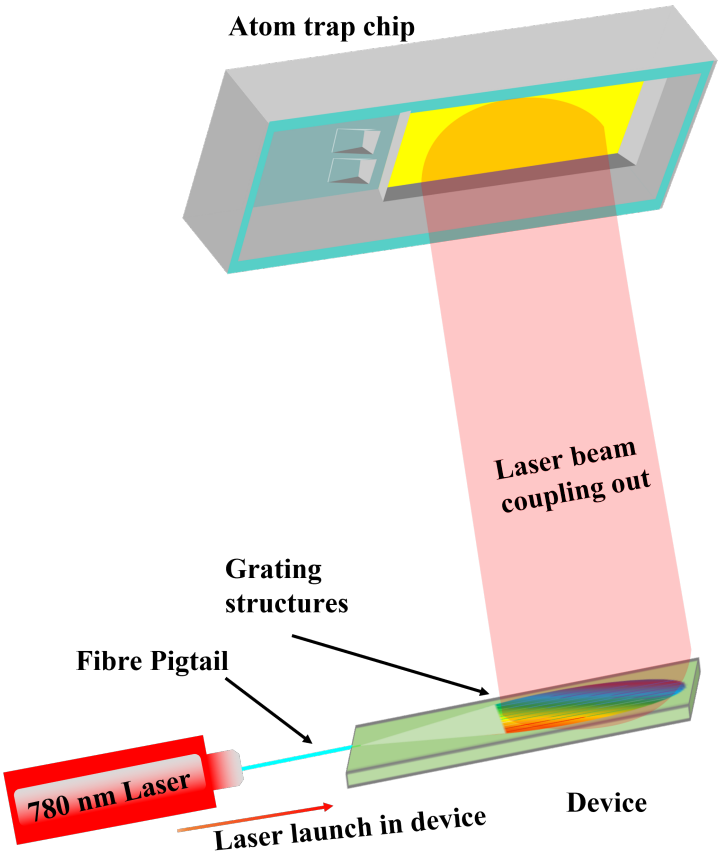

FIGURE 1.2: Schematic of the required fibre-coupled integrated device geometry, projecting the laser beam into a miniaturised atom trap chip.

1.4 Outline of thesis

The thesis consists of six chapters. Chapter 2 introduces Bragg gratings with an overview of the grating fabrication methods. It also discusses the fabrication systems such as flame hydrolysis deposition (FHD) and small spot direct UV writing (SSDUW).

Chapter 3 provides detail of SSDUW using a phase-control technique. We provide a complete system calibration and characterization of waveguides and Bragg gratings that were holographically fabricated using a 213 nm laser.

Chapter 4 presents valuable information on the ideal writing regimes for using a 213 nm laser to inscribe planar Bragg gratings. We discuss the mechanisms of photosensitivity and compare them to other UV processing techniques, such as 244 nm, picosecond 213 nm, and excimer lasers. Additionally, we present details on the damage caused by 213 nm laser-induced processing.

Chapter 5 introduces blazed gratings and presents an approach for fabricating an out-of-plane 45° blazed grating coupler, as well as a discussion on the tolerances of blazed gratings. The chapter broadly encompasses the work done to overcome the fabrication challenges associated with the holographic fabrication of out-of-plane 45° blazed gratings. Various devices based on blazed gratings, including 1D channel waveguides and gratings, as well as 2D large-area gratings, are fabricated and characterized.

Chapter 6 provides a summary of the findings in this thesis and discusses potential future work.

1.5 References

[1] P. Treutlein, P. Hommelhoff, T. Steinmetz, T. W. Hänsch, and J. Reichel, "Coherence in microchip traps," *Physical Review Letters*, vol. 92, no. 20, p. 203 005, 2004.

[2] S. Wildermuth, S. Hofferberth, I. Lesanovsky, S. Groth, P. Krüger, J. Schmiedmayer, and I. Bar-Joseph, "Sensing electric and magnetic fields with Bose-Einstein condensates," *Applied Physics Letters*, vol. 88, no. 26, p. 264 103, 2006.

[3] J. A. Rushton, M. Aldous, and M. D. Himsworth, "Contributed review: The feasibility of a fully miniaturized magneto-optical trap for portable ultracold quantum technology," *Review of Scientific Instruments*, vol. 85, no. 12, p. 121 501, 2014.

[4] S. Kim, D. A. Westly, B. J. Roxworthy, Q. Li, A. Yulaev, K. Srinivasan, and V. A. Aksyuk, "Photonic waveguide to free-space Gaussian beam extreme mode converter," *Light: Science & Applications*, vol. 7, no. 1, pp. 1–13, 2018.

[5] L. Chrostowski and M. Hochberg, *Silicon photonics design: from devices to systems*. Cambridge University Press, 2015.

[6] D. F. Edwards, "Silicon (si)," in *Handbook of optical constants of solids*, Elsevier, 1997, pp. 547–569.

[7] N. Izhaky, M. T. Morse, S. Koehl, O. Cohen, D. Rubin, A. Barkai, G. Sarid, R. Cohen, and M. J. Paniccia, "Development of CMOS-compatible integrated silicon photonics devices," *IEEE Journal of Selected Topics in Quantum Electronics*, vol. 12, no. 6, pp. 1688–1698, 2006.

[8] K. Yamada, T. Tsuchizawa, H. Nishi, R. Kou, T. Hiraki, K. Takeda, H. Fukuda, Y. Ishikawa, K. Wada, and T. Yamamoto, "High-performance silicon photonics technology for telecommunications applications," *Science and Technology of Advanced Materials*, 2014.

[9] K. Peng, M. Zhang, A. Lu, N.-B. Wong, R. Zhang, and S.-T. Lee, "Ordered silicon nanowire arrays via nanosphere lithography and metal-induced etching," *Applied physics letters*, vol. 90, no. 16, p. 163 123, 2007.

[10] Y. A. Vlasov, "Silicon CMOS-integrated nano-photonics for computer and data communications beyond 100G," *IEEE Communications Magazine*, vol. 50, no. 2, s67–s72, 2012.

[11] Y. Xu, X. Hu, S. Kundu, A. Nag, N. Afsarimanesh, S. Sapra, S. C. Mukhopadhyay, and T. Han, "Silicon-based sensors for biomedical applications: A review," *Sensors*, vol. 19, no. 13, p. 2908, 2019.

[12] G. De Paoli, S. L. Jantzen, T. D. Bucio, I. Skandalos, C. Holmes, P. G. Smith, M. M. Milosevic, and F. Y. Gardes, "Laser trimming of the operating wavelength of silicon nitride racetrack resonators," *Photonics Research*, vol. 8, no. 5, pp. 677–683, 2020.

[13] A. R. Zanatta and I. B. Gallo, "The thermo optic coefficient of amorphous SiN films in the near-infrared and visible regions and its experimental determination," *Applied Physics Express*, vol. 6, no. 4, p. 042 402, 2013.

[14] J. S. Levy, K. Saha, Y. Okawachi, M. A. Foster, A. L. Gaeta, and M. Lipson, "High-performance silicon-nitride-based multiple-wavelength source," *IEEE Photonics Technology Letters*, vol. 24, no. 16, pp. 1375–1377, 2012.

[15] Y.-C. Yeo, Q. Lu, P. Ranade, H. Takeuchi, K. J. Yang, I. Polishchuk, T.-J. King, C. Hu, S. Song, H. Luan, *et al.*, "Dual-metal gate CMOS technology with ultra-thin silicon nitride gate dielectric," *IEEE Electron Device Letters*, vol. 22, no. 5, pp. 227–229, 2001.

[16] R. Kitamura, L. Pilon, and M. Jonasz, "Optical constants of silica glass from extreme ultraviolet to far infrared at near room temperature," *Applied optics*, vol. 46, no. 33, pp. 8118–8133, 2007.

[17] X. Chen, J. Lin, and K. Wang, "A review of silicon-based integrated optical switches," *Laser & Photonics Reviews*, p. 2 200 571, 2023.

[18] B. Deng, Y. Shi, and F. Yuan, "Investigation on the structural origin of low thermal expansion coefficient of fused silica," *Materialia*, vol. 12, p. 100 752, 2020.

[19] A. Kros, M. Gerritsen, V. S. Sprakel, N. A. Sommerdijk, J. A. Jansen, and R. J. Nolte, "Silica-based hybrid materials as biocompatible coatings for glucose sensors," *Sensors and Actuators B: Chemical*, vol. 81, no. 1, pp. 68–75, 2001.

[20] K. K. Mehta, C. D. Bruzewicz, R. McConnell, R. J. Ram, J. M. Sage, and J. Chiaverini, "Integrated optical addressing of an ion qubit," *Nature Nanotechnology*, vol. 11, no. 12, pp. 1066–1070, 2016.

[21] K. K. Mehta and R. J. Ram, "Precise and diffraction-limited waveguide-to-free-space focusing gratings," *Scientific Reports*, vol. 7, no. 1, pp. 1–8, 2017.

[22] H. Becker, C. J. Krückel, D. V Thourhout, and M. J. R. Heck, "Out-of-plane focusing grating couplers for silicon photonics integration with optical MRAM technology," *IEEE Journal of Selected Topics in Quantum Electronics*, vol. 26, no. 2, pp. 1–8, 2019.

[23] A. Yulaev, W. Zhu, C. Zhang, D. A. Westly, H. J. Lezec, A. Agrawal, and V. Aksyuk, "Metasurface-integrated photonic platform for versatile free-space beam projection with polarization control," *ACS photonics*, vol. 6, no. 11, pp. 2902–2909, 2019.

[24] S. Kerman, D. Vercruysse, T. Claes, A. Stassen, M. Mahmud ul Hasan, P. Neutens, V. Mukund, N. Verellen, X. Rottenberg, L. Lagae, *et al.*, "Integrated nanophotonic excitation and detection of fluorescent microparticles," *ACS Photonics*, vol. 4, no. 8, pp. 1937–1944, 2017.

[25] F. Van Laere, T. Claes, J. Schrauwen, S. Scheerlinck, W. Bogaerts, D. Taillaert, L. O'Faolain, D. Van Thourhout, and R. Baets, "Compact focusing grating couplers for silicon-on-insulator integrated circuits," *IEEE Photonics Technology Letters*, vol. 19, no. 23, pp. 1919–1921, 2007.

[26] S. M. Schultz, E. N. Glytsis, and T. K. Gaylord, "Volume grating preferential-order focusing waveguide coupler," *Optics letters*, vol. 24, no. 23, pp. 1708–1710, 1999.

[27] S. M. Schultz, E. N. Glytsis, and T. K. Gaylord, "Design of a high-efficiency volume grating coupler for line focusing," *Applied optics*, vol. 37, no. 12, pp. 2278–2287, 1998.

Chapter 2

Background of Bragg grating fabrication techniques

2.1 Introduction

Chapter 1 has provided the overall motivations for the current PhD project, including why this research area is essential and what has been done already in this field. The fundamentals of the fabrication techniques used in this work are described in this chapter, with more detail in the relevant later chapters.

2.2 Bragg grating

The work in this thesis embraces a key technology: Bragg gratings, which are structures with periodicity in only one dimension. Interacting waves with these structures are either transmitted or reflected depending upon their wavelength and the angle of incidence to the gratings. Bragg gratings are considered as a special case of diffraction gratings having wave propagation normal to the interface of period. The first proof for Bragg structures was introduced by Lawrence Bragg and Henry Bragg [1]. In their work, X-rays were used to investigate the structure of an atomic lattice by deriving the Bragg's law in the equation 2.1 which defines the angle of the reflection from a periodic structure. This equation explains the constructive interference of waves reflecting from the periodic structure.

$$2dsin(\theta) = m\lambda \tag{2.1}$$

Here d is the distance between atoms in a crystal lattice, m is an integer and θ is the angle of the incident wave. Bragg's law is not limited to the interaction of X-rays to the atoms but can be applied to any electromagnetic radiation interacting with a periodic structure. The Bragg equation for optically fabricated gratings can be derived by wave vector logic. Fig. 2.1 shows a schematic of a material with a one dimensional periodic change of refractive index with period Λ, where K_i and K_r are the k vectors of the incident and reflected wave respectively. According to the law of conservation,

both incident and reflected vectors can be equated as equation 2.2 and lead to Bragg expression in equation 2.3.

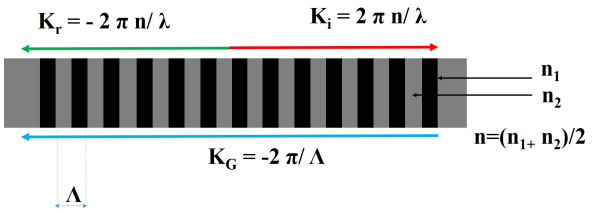

FIGURE 2.1: Diagram of Bragg gratings within channel waveguide, where K_i and K_r are the wavevectors of the incident and reflected light, whereas K_G is the grating vector.

$$K_i + K_G = K_r \tag{2.2}$$

$$\lambda_B = 2n\Lambda \tag{2.3}$$

Here λ_B is the wavelength of reflected wave and n is the average refractive index of the material.

2.3 Gratings fabrication methods

2.3.1 Phase Masks

The phase mask technique is one of the most well-known techniques to define Bragg grating structures into optical fibres. Phase masks are fundamentally diffractive elements, and provide a spatial phase modulation of an incident UV beam. They are normally made from silica having one side of the surface etched to provide a periodic platform to behave as a grating structure. The first fibre Bragg gratings were made using this approach in 1993 [2]. In planar fabrication, waveguides are defined first via chemical etching, and Bragg gratings are fabricated on the stationary sample using a phase mask with a large UV beam exposure. The method is suitable for mass production of grating-based devices and with the addition of translation stages extensively long high quality gratings can be produced. However, the predefined pattern of the phase mask limits the method. To fabricate more complex grating profiles, such as apodised and chirped gratings requires a more expensive phase mask.

2.3.2 Femtosecond laser writing

Another technique to define grating structures is the Point-by-Point (PbP) writing and is commonly achieved with femtosecond laser inscription. In this technique, a tightly focused laser pulse is incident on the fibre core and ideally, a single laser pulse is employed to define the modulation of refractive index in the fibre core [3]. However, Pbp inscribed fibre Bragg gratings (FBGs) exhibit noticeable polarisation-dependent response and relatively high insertion loss [4]. This is primarily due to the fact that each period modification is inscribed using a single laser shot, and the uniformity of the inscription is unreliable since the laser energy can vary between pulses. As a result, an uneven

index change occurs, leading to significant spectral noise. Moreover, the alignment process for writing first-order Pbp FBGs in the centre of the fibre core is demanding and time-consuming [4]. This is because the focused laser beam is small, requiring considerable effort to align the fibre parallel to the motion direction of the translation stage. Additionally, longer gratings necessitate even more precise alignment. In contrast, line-by-line (LBL) FBG structures, created using a femtosecond laser, allow for relatively coarse alignment and exhibit lower insertion loss and polarisation dependency [4]. Another method of writing is plane-by-plane (PBP) direct writing using femtosecond laser inscription [5]. This technique provides flexibility in creating gratings with control over their period, as well as the length, width, and depth of the individual grating planes. The width of the laser-inscribed planes is determined by the numerical aperture (NA) of the lens used, while the other dimensions can be controlled through precise motion of the translation stage. As a result, this approach enables the creation of three-dimensional refractive index changes with controlled plane length, depth, and grating plane angle [5]. The other notable difference is that the femtosecond laser typically interacts with silica via avalanche ionisation; hence removing the necessity for material photosensitivity [6]. High thermal stability (at temperatures > 1000 °C) [7], [8] is a promising advantage of this writing approach. Femtosecond writing also provides a unique ability to fabricate 3D photonic structures [9]. However, femtosecond lasers can be quite expensive. The use of femtosecond lasers can be challenging to inscribe large-area and complex devices due to excessive fabrication time and non-uniformity of devices originating from the nonlinear laser material interaction (avalanche ionisation).

2.3.3 Etched gratings

Integration of Bragg structures within planar or integrated waveguides most often employs lithography and etching to fabricate periodic Bragg structures [10]. This has been demonstrated in all the major integrated optics platforms. In this technique, the modulation of the refractive index is achieved by physically varying the dimensions of the waveguide (Fig. 2.3.3). In a strip waveguide geometry, the waveguide and sidewall gratings structures can be fabricated in a single lithography process [10]. This technique yields a higher refractive index modulation than the laser-written approaches. However, the processes involved in clean room fabrication require a high level of precision. For example, during photolithography, a mask is used to transfer a pattern onto a substrate. The alignment and exposure of the mask must be extremely accurate to achieve the desired results. Similarly, during etching, the removal of specific material layers requires precise control to avoid damaging the underlying structures. Achieving this level of precision takes time and meticulous attention to detail. Additionally, clean room processes require thorough optimisation and quality control to ensure consistent and reliable results. Fine-tuning process parameters and conducting quality control checks at various stages are essential. These optimisation and quality control measures contribute to the overall processing time and hence not flexible for device prototyping. Besides the processing time, phase errors across waveguide thickness and grating period limit the size of integrated devices.

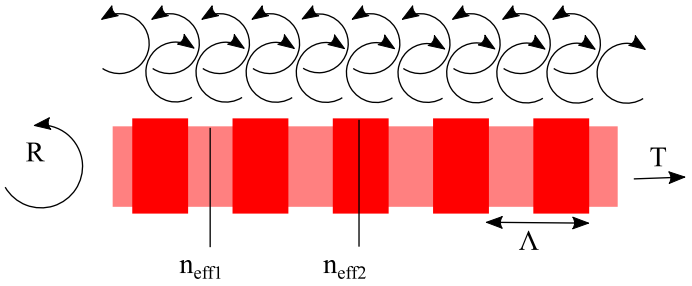

FIGURE 2.2: Demonstration of uniform Bragg gratings based on Silicon-on-Insulator (SOI) waveguide. n_{eff1} and n_{eff2} are low and high effective indices respectively. T and R stand for transmission and reflection and Λ is the grating period.

2.3.4 Direct UV writing

Direct UV Writing (DUW) is a technique to permanently change the refractive index in fibre and planar silica on UV exposure without a phase mask or etching.

Technique	Advantages	Disadvantages
Etched gratings	High index contrast lead to higher coupling efficiencies	Require extremely high fabrication accuracy, phase errors limit the size of the device
Femtosecond writing	Independent of photosensitivity. Enables to inscribe gratings to survive at high temperatures	Refractive index change is based on non-linear avalanche ionisation, which leads to a non-uniform grating profile
Phase mask method	Stable interference pattern, which leads to high-quality gratings	Limited by the spot of the laser source. Not suitable where a complex grating profile is required
Direct UV writing	Phase controlled system in small spot UV writing provides ability to detune the grating period, enabling fabrication of complex grating profiles such as Gaussian apodised and chirped grating only via software control. Fabrication of channel waveguides and gratings in a single step is more flexible	Weak gratings due to low index contrast , highly sensitive to a thermal drift

TABLE 2.1: Grating fabrication methods with pros and cons.

The first waveguides made using this approach were by Svalgaard et al. [11] in 1994. Later, the University of Southampton modified the technique, allowing the simultaneous fabrication of waveguides and Bragg gratings. The details of this writing technique will be discussed in Chapter 3. The method relies on the photosensitivity of the substrate, which is achieved by adding dopants into the silica by flame hydrolysis deposition or plasma enhanced chemical vapour deposition. We expect a low index contrast with better phase stability in UV-written devices compared to the etched grating couplers. This is the approach which will be developed and used in this work.

Each fabrication method has pros and cons, and are summarised in Table 2.1.

2.4 Fabrication of silica-on-silicon wafer by FHD

The first step of fabricating integrated grating couplers is depositing silica layers on a silicon substrate. For this purpose, 6-inch silicon wafers are the base substrate. In later stages, photosensitive core and cladding layers are deposited to achieve a silica-on-silicon platform for light guiding. An essential aspect of fabrication is the difference of thermal expansion coefficient between a core layer of silica ($\sim$ 0.4×10^{-6} $^{\circ}C^{-1}$) and silicon (2.5×10^{-6} $^{\circ}C^{-1}$) [12], which causes compression on the silica core layer induced during cooling in the consolidation process. To counter this problem, a layer $\sim$ 14-17 µm of thermal oxide (THOX) is introduced as a buffer layer on the silicon wafer before the deposition of the core and cladding silica. The thermal oxide layer is grown by placing silicon wafers in high temperature $\sim$ 1100 °C wet furnace for 3-4 weeks and often acts as the underclad. This buffer layer provides better adhesion to subsequent deposited layers of silica. The thermally oxidised wafers with the required thickness are purchased commercially.

Flame Hydrolysis Deposition (FHD) is a commercial method to depositing silica layers onto a substrate. Halides-based precursors react chemically in an oxy-hydrogen flame, leaving silica soot on the substrate. Silicon Tetrachloride ($SiCl_4$) is used as a precursor for producing and depositing silica soot. The following chemical reactions can describe temperature-dependent chemical reactions involved in the process.

$$\text{Direct Oxidation} > 1200^{\circ}C \quad SiCl_4 + O_2 \rightarrow SiO_2 + 2Cl_2$$

$$\text{Hydrolysis} < 1200^{\circ}C \quad SiCl_4 + 2H_2O \rightarrow SiO_2 + 4HCl_2$$

At the centre of the flame, where the temperature is greater than 1200 °C, direct oxidation occurs, while at temperatures lower than 1200 °C hydrolysis takes place. Halide dopants, including phosphorous trichloride (PCl_3), germanium tetrachloride ($GeCl_4$) and boron trichloride (BCl_3) are introduced via similar chemical vapours for the doping of phosphorous, germanium and boron respectively. Boron and germanium are specifically used to increase the photosensitivity of the core layer. Ge increases the refractive index of the core layer, while Boron decreases the refractive index. Boron increases the photosensitivity of the layer and leads the more change in refractive index upon laser exposure. It also lowers down the melting/consolidation temperature of glass matrix. The role of dopants on the properties of glass matrix is given in Table 2.2 Variation in the dopant concentration in the oxy-hydrogen flame provides control of the photosensitivity and refractive index of the deposited layers. As shown in Fig. 2.3, substrate

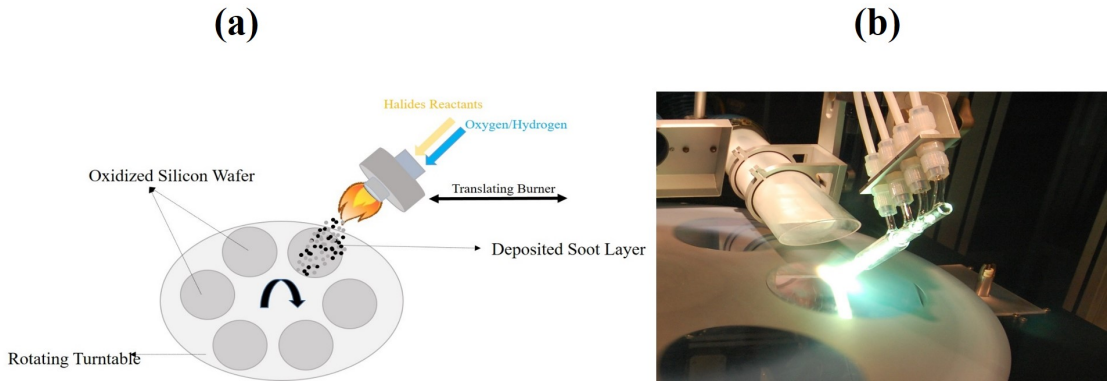

FIGURE 2.3: (a) Schematic of FHD deposition on a silicon wafer. (b) Photograph of deposition setup (Courtesy: Dr Paolo Mennea).

wafers are mounted on a rotating plate, over which the FHD flame makes several passes to and fro. Variation in the number of passes provides control of the deposited layer thickness according to the requirement of single-mode operation. Thermal consolidation, soot structure and dopant concentration define the structure of the final glass layer [13]. Figure 2.4 shows a scanning electron microscope image of a typical silica-on-silicon wafer consisting of multiple silica layers deposited by FHD.

Dopant	Photosensitivity	Refractive index	Melting point
Germanium	↑	↑	↓
Boron	↑	↓	↓
Phosphorous	–	↑	↓

TABLE 2.2: Role of dopants on the properties of glass matrix

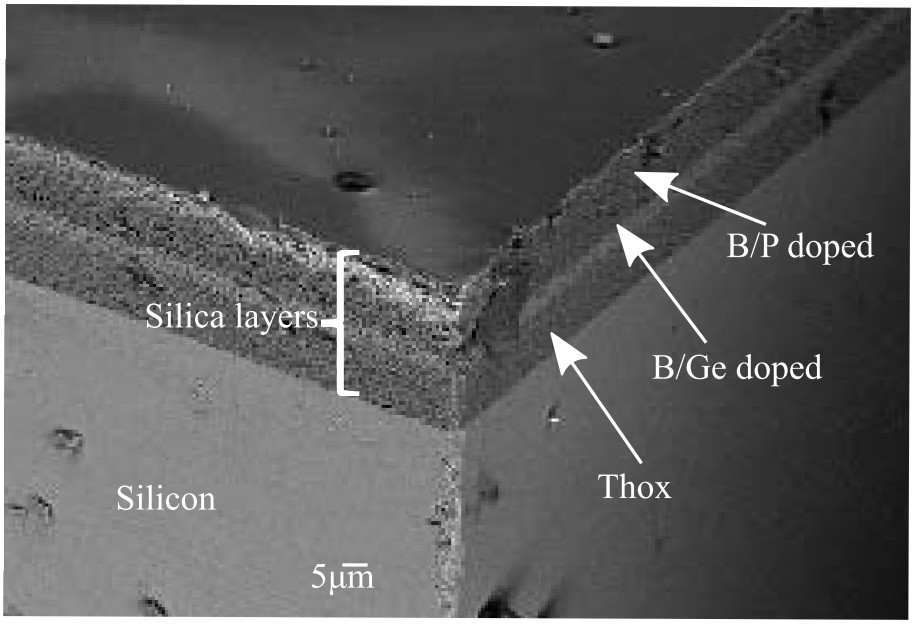

FIGURE 2.4: Scanning electron microscope image of a typical silica-on-silicon wafer, consisting of multiple silica layers upon a 1-mm thick silicon substrate.

2.4.1 Photosensitivity of the core layer

Photosensitivity in planar layer refers to a permanent change in the refractive index when the core layer is exposed to photons with certain characteristic wavelengths and intensities. Direct UV writing phenomena depend strongly on photosensitivity, which is exploited to inscribe the integrated waveguides and Bragg grating structures in the core layer. The physical mechanisms which lead to photosensitivity are complex and not well understood. One of the explanations behind the intrinsic photosensitivity of the core layer is attributed to the defects inside the glass matrix, which the doping of germanium and boron can generate. The addition of dopants leads to point defects in the post-consolidated glass matrix. Pure silica has a tetrahedral structure with a silicon atom in Fig. 2.5 (a), bonded with four oxygen atoms within the glass matrix. Consolidation of the glass matrix in an oxygen-deficient environment leads to silica Neutral Oxygen Vacancy (NOV) defects, which are formed due to the wrong bonds between two silicon atoms [14](as shown in Fig. 2.5 (b)). Since germanium has identical valency as silicon, similar NOV defects are present due to Si-Ge and Ge-Ge wrong bonds inside the glass (as shown in Fig. 2.5 (c and d)). Colour centres formed in the germanosilicate matrix are associated with absorption at characteristic wavelengths, making the glass photosensitive in the UV region. Mechanisms behind photosensitivity predict the variation in NOV centres upon UV exposure, consequently exciting or releasing an electron [14].

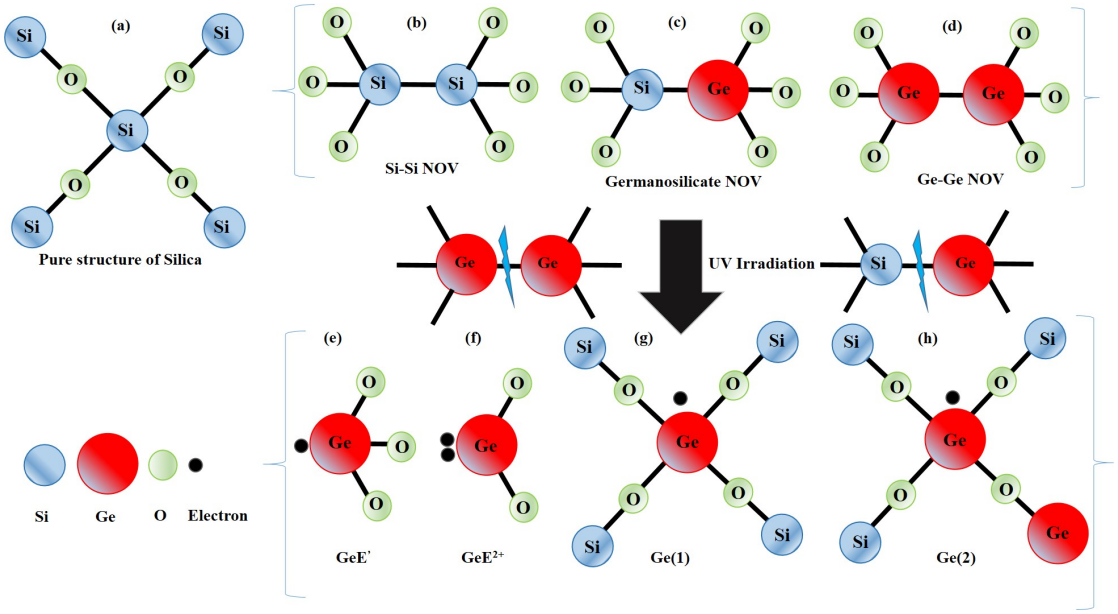

FIGURE 2.5: Illustration of various kinds of germanosilicate defects with UV radiation.

In the case of NOV defects, UV radiation breaks the bonds between Ge-Ge or Si-Ge, ultimately leading to GeE' centres (Fig. 2.6(e)). The released electron can either recombine with GeE' to generate luminescence or it can propagate through a glass matrix, leading to Ge(1) and Ge(2) electron trap centres (as shown in Fig. 2.6 (g and h)). E' centres correspond to a 5.8 eV optical absorption band in silica and are considered as the mechanism for the UV photosensitivity at 213 nm [15]. Another defect in germanium doped silica is Ge^{+2}, both Ge^{+2} and NOV-related defects are associated to photosensitivity with absorption in the UV region between 240-245 nm [16]. UV-induced stresses

and densification alongside these defects cause a change in the refractive index of silica [17], [18].

2.4.2 UV induced photochemical refractive index changes

Amorphous glasses do not have a repeating unit cell but possess a recurrent bond structure, as illustrated in Fig. 2.5. This bond structure imposes certain angular conditions and limits the lengths of the bonds, which can lead to the formation of defects in the amorphous form due to doping or dangling oxygen bonds. Silica glass exhibits several absorptions ranging from 4 eV to 6 eV [19], corresponding to photochemical changes in the bonding structure. The changes in material absorption properties lead to a variation in the refractive index of the material due to the Kramers-Kronig relation. Adding dopants to the glass increases the variety of absorption defects and disrupts the structure, increasing the probability of bonding defects. Despite extensive research, the defects responsible for photosensitivity at 244 nm in germane-silicate glasses remain disputed [19]–[21]. Identification of defects in amorphous structures is challenging for techniques designed for crystalline structures since the electronic configuration surrounding the defect has a substantial influence on its response. However, understanding the underlying glass chemistry is not essential for device fabrication as the refractive index response can be characterised. In addition to dopants, 244 nm laser processing requires hydrogen loading to achieve a significant photosensitive response. Lemaire et al. found that hydrogen in diffusion doubled the refractive index contrast from 3×10^{-3} to 5.9×10^{-3} in germanium-doped fibres. Indiffused hydrogen is believed to interact with defect-induced index changes by stabilising UV-induced chemical changes with hydroxyl groups [22]. Earlier research group members discovered that 244 nm laser processing does not induce appreciable refractive index contrast in FHD glass samples without hydrogen loading. Therefore, we put FHD samples in a high-pressure (approximately 120 bar) hydrogen environment for at least five days before UV writing. The group members also investigated Deuterium loading since previous studies suggest it may lead to a lower propagation loss than hydrogen at 1550 nm due to the shift in the OH overtone from 1.4 µm to 1.9 µm for oxygen deficiency [22]. Initial tests conducted in Southampton have not revealed substantial differences between hydrogen and deuterium loading. Therefore, due to its lower cost, hydrogen is typically preferred over deuterium for integrated chips. Once we remove the planar silica chips from the high-pressure cell, hydrogen rapidly starts outgassing. Previous investigations based on modelling have shown that within an hour, the hydrogen concentration inside a planar layer with a 15 µm thick cladding layer has reduced by 50 % [23]. A strict limit of 2 hours is typically used for 244 nm UV processing to ensure waveguide and grating fabrication. After removal from the hydrogen cell, planar chips are stored in liquid nitrogen or a freezer; modelling investigation from previous group members suggests the outgassing rate becomes insignificant at a low-temperature environment [23]. Methods of eliminating hydrogen outgassing have been investigated for applications where UV fabrication times exceed the outgassing time. One such technique involves 'thermally locking'hydrogen into a sample using a rapid thermal annealing process; this enables the UV process without a limit of fabrication time [24]–[26]. As an alternative, our research group has explored direct UV writing using a nanosecond pulsed 213 nm laser. Prior work on channel waveguide inscription in planar silica suggests, 213 nm UV processing could achieve similar induced refractive indices without hydrogen loading [27].

2.4.3 Densification

Densification refers to a process in which the density of glass varies upon UV exposure. This change in density leads to a corresponding change in the refractive index [17] and is also associated with photochemical alterations. Densification closely relates to stress variations within the glass, affecting the refractive index. An explicit indication of densification in the core layer has been observed in unclad FHD samples after UV exposure [23] in the form of trenches. In contrast, under UV exposure, PECVD samples have been found to exhibit localised density reductions [28]. Typically, densification and stress effects cause changes in grating growth dynamics (e.g., blue shift of Bragg wavelength, partial erasure of gratings) at high exposures below the damage threshold.

2.4.4 Small spot direct UV writing (SSDUW)

The Optical Engineering and Quantum Photonics group in Southampton has been working for over 20 years on fabricating Bragg gratings in fibre and planar silica for various applications in integrated optics containing components such as couplers, beamsplitters, polarisers and sensors. The technique is small spot direct UV writing, which uses dual-beam interferometry with a phase-controlled system to simultaneously inscribe both waveguides and Bragg grating in doped silica (see Fig. 2.6(a)), using a continuous-wave (CW) frequency-doubled Ar-ion laser operating at a wavelength of 244 nm.

Figure 2.6(b) demonstrates the refractive index profile of the Bragg gratings fabricated in silica using SSDUW. Silica has a core refractive index before grating fabrication and is labelled as n_{core}. After fabrication, the refractive index changes to a higher value, called n_{avg}. In the simultaneous fabrication of gratings and waveguides, these refractive indices are considered equivalent to the effective index of the waveguide and denoted by n_{eff}. The dc (direct current, a term taken from electronics) part of the change in refractive index (Δn_{dc}) is the difference between the pre and post fabrication refractive index of the core. The refractive index contrast or the grating contrast is denoted by Δn_{ac}, which is the amplitude of the sinusoidal or ac (alternating current) component of the gratings. The complete details of the writing technique with the relationship between Δn_{ac} and Δn_{dc} will be discussed in Chapter 3.

One of the limitations of CW 244 nm laser writing is the need for hydrogen loading to induce sufficient change in the refractive index. The continuous out-gassing of hydrogen limits the UV writing time to $\sim$ 2 hours, after which a significant variation in the properties of the fabricated devices is observed due to reduced photosensitivity and hydrogen out-gassing. In 2016, the group purchased a pulsed laser source which operates at a wavelength of 213 nm. This system allows work on various potential applications, including fabricating grating-based devices without hydrogen loading and micro-machining. The system is a 5^{th} harmonic Q-switched laser with a wavelength of 213 nm, 0.1-30 kHz repetition rate, $\sim$ 7 ns pulse duration and a maximum average output power $\sim$ 125 mW. Due to the pulsed nature, the peak power of this laser source is much higher than the CW 244 nm laser. This source was first employed to fabricate Bragg gratings in hydrogen-free SMF-28 fibre using a phase mask technique [29]. In this work, the authors suggested that two-photon absorption is the dominant mechanism for the photosensitivity of B/Ge doped fibre. The photosensitivity mechanisms of 213 nm laser in planar doped silica with a comparison against other picoseconds 213 nm, CW 244 nm and excimer lasers will be discussed in Chapters 3 and 4.

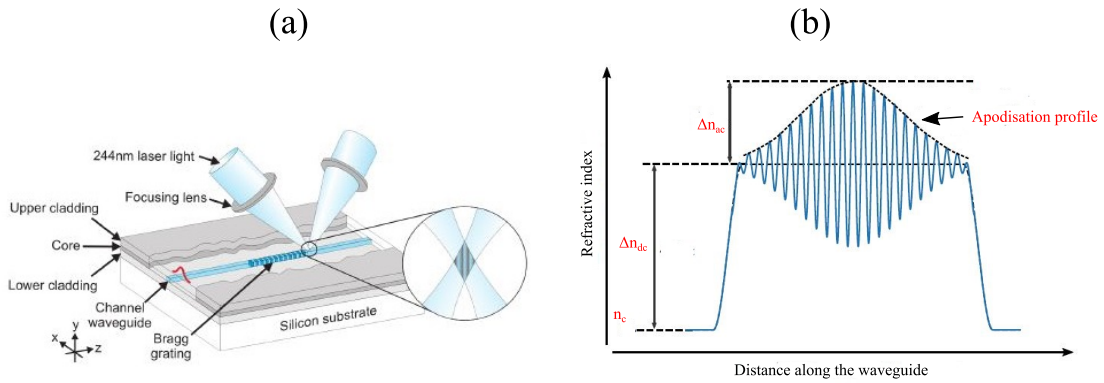

FIGURE 2.6: (a) Schematic of SSDUW to simultaneously fabricate waveguides and Bragg gratings in planar silica. (b) Schematic of refractive index modulation in SSDUW waveguides and gratings. Before writing the glass has a refractive index of n_c. Small spot direct UV writing induces an ac and dc refractive index modulation. The dc component creates a waveguide and is typically constant across a waveguide. The EOM phase control system controls the ac refractive index modulation and defines the apodisation across the grating.

2.4.5 Training and my contribution

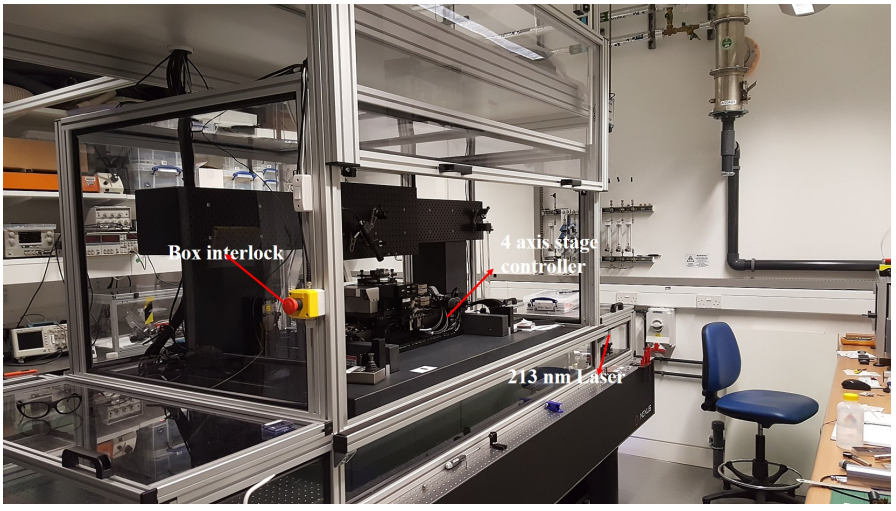

FIGURE 2.7: Photograph of 213 nm UV writing system when I joined the project (Courtesy: Dr Paul Gow).

At the start of this project, I received extensive training in equipment handling with all risk assessments from Dr Paul Gow. Training included wafer dicing, hydrogen loading of diced chips, fibre splicing, 213 nm and 244 nm UV processing, and UV-written Bragg gratings and waveguides characterisation. Before I joined the research group, the 213 nm UV writing system was already established (see Fig. 2.7). Dr Paul Gow had done extensive work on single-mode 213 nm written waveguides. However, this work did not contain gratings. Part way through my project the group also received funding to use 213 nm laser for fabricating large-area out-of-plane grating coupler. Using a pulsed 213 nm source to fabricate large-area grating couplers, my research goals were sub-categorised into several research questions.

- How does a 213 nm laser compare with a 244 nm laser system for planar waveguide and grating fabrication?
- Can we write planar Bragg gratings without hydrogen loading using a 213 nm laser? If yes, how do the devices and parameters compare to hydrogen-loaded fabricated devices?
- Does a 213 nm source generate non-linearity in photosensitivity or grating response, as previously reported in [29]?
- Considering the pulse nature of the 213 nm laser, what is the suitable regime (combination of laser power and fluence) to operate for waveguide and grating fabrication?
- Do holographically fabricated blaze gratings diffract enough light to make large out-of-plane grating couplers?
- What is the best proposed geometry for fabricable large-area devices?

I will address all these questions in the following chapters.

2.5 References

[1] W. H. Bragg and W. L. Bragg, "The reflection of X-rays by crystals," in *Proceeding of the royal society A*, 1913, pp. 428–438.

[2] K. O. Hill, B. Malo, F. Bilodeau, D. C. Johnson, and J. Albert, "Bragg gratings fabricated in monomode photosensitive optical fiber by UV exposure through a phase mask," *Applied Physics Letters*, vol. 62, no. 10, pp. 1035–1037, 1993.

[3] G. D. Marshall, R. J. Williams, N. Jovanovic, M. J. Steel, and M. J. Withford, "Point-by-point written fiber-Bragg gratings and their application in complex grating designs," *Optics Express*, vol. 18, no. 19, pp. 19 844–19 859, 2010.

[4] K. Zhou, M. Dubov, C. Mou, L. Zhang, V. K. Mezentsev, and I. Bennion, "Line-by-line fiber Bragg grating made by femtosecond laser," *IEEE Photonics Technology Letters*, vol. 22, no. 16, pp. 1190–1192, 2010.

[5] A. Ioannou, A. Theodosiou, C. Caucheteur, and K. Kalli, "Direct writing of plane-by-plane tilted fiber Bragg gratings using a femtosecond laser," *Optics letters*, vol. 42, no. 24, pp. 5198–5201, 2017.

[6] R. R. Gattass and E. Mazur, "Femtosecond laser micromachining in transparent materials," *Nature photonics*, vol. 2, no. 4, pp. 219–225, 2008.

[7] D. Grobnic, C. W. Smelser, S. J. Mihailov, and R. B. Walker, "Long-term thermal stability tests at 1000°C of silica fibre Bragg gratings made with ultrafast laser radiation," *Measurement Science and Technology*, vol. 17, no. 5, p. 1009, 2006.

[8] A. Martinez, I. Y. Khrushchev, and I. Bennion, "Thermal properties of fibre Bragg gratings inscribed point-by-point by infrared femtosecond laser," *Electronics letters*, vol. 41, no. 4, pp. 176–178, 2005.

[9] M. Lancry, B. Poumellec, J. Canning, K. Cook, J.-C. Poulin, and F. Brisset, "Ultrafast nanoporous silica formation driven by femtosecond laser irradiation," *Laser & Photonics Reviews*, vol. 7, no. 6, pp. 953–962, 2013.

[10] L. Chrostowski and M. Hochberg, *Silicon photonics design: from devices to systems*. Cambridge University Press, 2015.

[11] M. Svalgaard, C. V. Poulsen, A. Bjarklev, and O. Poulsen, "Direct UV writing of buried singlemode channel waveguides in Ge-doped silica films," *Electronics Letters*, vol. 30, no. 17, pp. 1401–1403, 1994.

[12] W. D. Callister, D. G. Rethwisch, *et al.*, *Materials science and engineering: an introduction*. John wiley & sons New York, 2007, vol. 7.

[13] M. Kawachi, M. Yasu, and T. Edahiro, "Fabrication of SiO_2-TiO_2 glass planar optical waveguides by flame hydrolysis deposition," *Electronics letters*, vol. 15, no. 19, pp. 583–584, 1983.

[14] A. S. Othonos and K. Kalli, *Fiber Bragg gratings fundamentals and applications in telecommunications and sensing*. Artech house, 1999.

[15] R. H. Magruder III, A. Stesmans, K. Clémer, R. A. Weeks, and R. A. Weller, "Sources of optical absorption between 5.7 and 5.9 eV in silica implanted with Si or O," *Journal of applied physics*, vol. 100, no. 3, p. 033 517, 2006.

[16] G. Meltz, W. W. Morey, and W. H. Glenn, "Formation of Bragg gratings in optical fibers by a transverse holographic method," *Optics Letters*, vol. 14, no. 15, pp. 823–825, 1989.

[17] M. Douay, W. Xie, T. Taunay, P. Bernage, P. Niay, P. Cordier, B. Poumellec, L. Dong, J. Bayon, H. Poignant, *et al.*, "Densification involved in the UV-based photosensitivity of silica glasses and optical fibers," *Journal of Lightwave technology*, vol. 15, no. 8, pp. 1329–1342, 1997.

[18] L. Zheng, J. C. Lambropoulos, and A. W. Schmid, "UV-laser-induced densification of fused silica: A molecular dynamics study," *Journal of non-crystalline solids*, vol. 347, no. 1-3, pp. 144–152, 2004.

[19] L. Skuja, "Optically active oxygen-deficiency-related centers in amorphous silicon dioxide," *Journal of NON-crystalline Solids*, vol. 239, no. 1-3, pp. 16–48, 1998.

[20] J. Canning, "Fibre gratings and devices for sensors and lasers," *Laser & Photonics Reviews*, vol. 2, no. 4, pp. 275–289, 2008.

[21] L. Skuja, H. Hosono, and M. Hirano, "Laser-induced color centers in silica," in *Laser-Induced Damage in Optical Materials: 2000*, SPIE, vol. 4347, 2001, pp. 155–168.

[22] J. Stone, "Interactions of hydrogen and deuterium with silica optical fibers: A review," *Journal of Lightwave technology*, vol. 5, no. 5, pp. 712–733, 1987.

[23] R. H. S. Bannerman, "Microfabrication of waveguide-based devices for quantum optics," Ph.D. dissertation, University of Southampton, 2019.

[24] A. Jantzen, "The design, fabrication and development of micromechanical integrated optical pressure sensors for aerospace," Ph.D. dissertation, University of Southampton, 2019.

[25] M. Fokine and W. Margulis, "Large increase in photosensitivity through massive hydroxyl formation," *Optics Letters*, vol. 25, no. 5, pp. 302–304, 2000.

[26] C. Holmes, "Direct UV written planar devices for sensing and telecommunication applications," Ph.D. dissertation, University of Southampton, 2009.

[27] P. C. Gow, Q. S. Ahmed, P. L. Mennea, R. H. S. Bannerman, A. Jantzen, C. Holmes, J. C. Gates, C. B. Gawith, and P. G. R. Smith, "213 nm laser written waveguides in Ge-doped planar silica without hydrogen loading," *Optics Express*, vol. 28, no. 21, pp. 32 165–32 172, 2020.

[28] F. Knappe, "Waveguide structuring and Bragg grating fabrication by ultraviolet light induced refractive index changes in photosensitive optical materials," Ph.D. dissertation, University of Southampton, 2019.

[29] M. Gagné and R. Kashyap, "New nanosecond Q-switched Nd:VO_4 laser fifth harmonic for fast hydrogen-free fiber Bragg gratings fabrication," *Optics Communications*, vol. 283, no. 24, pp. 5028–5032, 2010.

Chapter 3

Characterisation of 213 nm channel waveguides and Bragg gratings in planar silica

Chapter 2 introduced Bragg gratings and their fabrication methods with the associated pros and cons. The small spot UV writing technique in doped planar silica was also briefly discussed. This chapter will discuss the calibration and characterisation of the pulsed 213 nm laser source for writing gratings and waveguides in planar-doped silica.

The current project aims to fabricate the large area grating couplers using a pulsed 213 nm laser. Following that direction, it is essential to fully understand the dynamics of this new laser system as a first step. When investigating a large parameter space (such as the UV-written FHD platform provides), characterisation methods must give as much information as possible to optimise devices quickly. This chapter discusses in-depth system calibration of the 213 nm laser to inscribe waveguides and Bragg gratings in planar silica with and without hydrogen loading. We fully calibrate the system for grating writing using the dual-beam technique, where one arm of an interferometer is phase modulated using an electro-optic modulator (EOM). We also provide a detailed characterisation of our UV-written devices, including the fluence dependence of photosensitivity, gratings strength, and hence modulated change in the refractive index (Δn_{ac}), the bandwidth of detuning, and the propagation loss in the waveguide. We also address some of the constraints of UV writing in non-hydrogen-loaded samples, which takes a long fabrication time. Finally, we present a favourable writing approach in hydrogen-loaded samples over a long period, which is crucial for defining large-area grating-based structures.

James Gates and Paolo Mennea fabricated the FHD layers discussed in this chapter. Paul Gow provided all the initial training for UV fabrication and device characterisation. Modelling was performed in conjunction with James Gates, James Field and Rex Bannerman. Waveguide and grating fabrication, characterisation and data analysis were solely my own work.

3.1 Experimental setup and system calibration

The DGW system using a 213 nm laser (shown in Fig. 3.1(a)) operates with the same principle as prior work using a 244 nm CW laser [1]. However, the geometry and components have been modified to account for the change in UV operating wavelength.

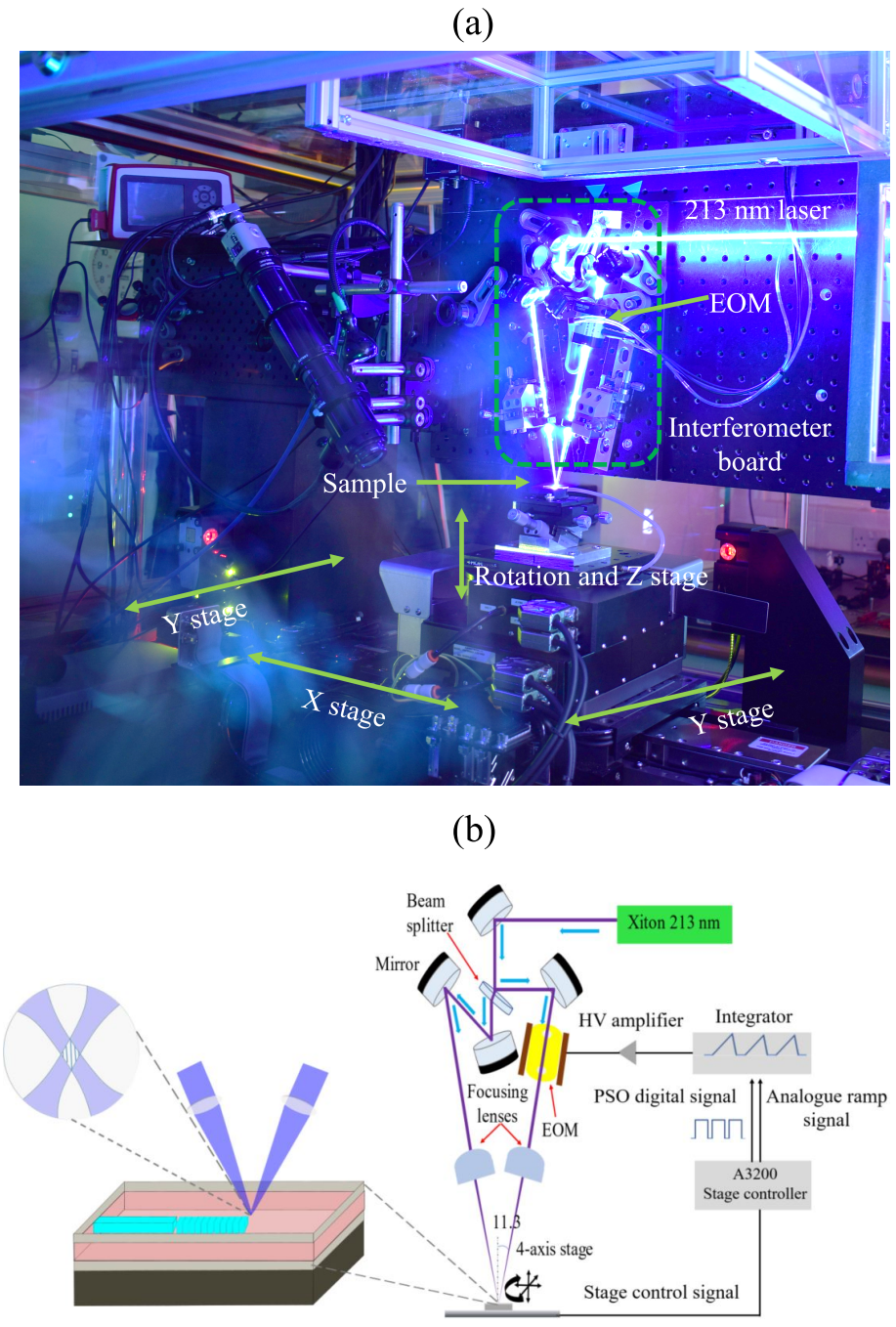

FIGURE 3.1: (a) Photograph of the 213 nm UV writing setup. (b) Schematic of the 213 nm UV writing setup for simultaneously defining channel waveguides and Bragg gratings in planar silica.

Fig. 3.1(b) shows a schematic of the phase-controlled DGW technique, which relies on precision translation stages and a UV laser. The UV pattern was generated by the interference of two UV beams from a fifth harmonic solid-state Nd: YVO_4 laser operating at a wavelength of 213 nm (Xiton Photonics, Impress 213). The laser beam was spatially filtered and beam expanded before splitting by a beam splitter to supply the two arms of the interferometer. One beam of the interferometer passed through a bespoke DKDP electro-optic modulator (EOM, Leysop Ltd.) to provide spatial control of the interference pattern. A pair of planoconvex CaF_2 lenses were used to focus both laser beams at the same point in space, where the UV inscription pattern is formed. The period of the fringes is related to the crossing angle of the beams.

In this chapter, the target Bragg grating wavelength is the 1550 nm telecommunication band and equates to a period of 535.6 nm and a crossing angle of $\sim 22.6°$ (half angle $\sim 11.3°$). This angle is achieved through the alignment of the interferometer. However, as we will discuss later, the bandwidth of the system is such that accurate alignment is not critical. Via applied voltage to the EOM, it is possible to control the position of the fringe pattern within the foci of the two beams. Therefore, precise modulation of the EOM voltage can be used to translate the interference pattern in phase with the translation speed of the sample [1]. This technique allows the simultaneous fabrication of channel waveguide and grating structures during constant sample translation.

In this work, three-layer silica-on-silicon was used as the photosensitive platform. Flame hydrolysis deposition (FHD) was used to deposit a 4.2 µm thick core layer of germanium and boron-doped silica core onto a silicon wafer with a 15 µm thermal oxide acting as an underclad. The core layer was capped with index-matched 15.1 µm thick boron and the phosphorous-doped over-clad layer. The resulting refractive indices of core and upper-cladding layers were 1.447 and 1.4446 at 1550 nm. The wafer identifier number of the used deposition recipe was PX 198 (see Appendix 1 for complete deposition details). Individual chips measuring 10 × 20 mm were diced from this wafer using a Loadpoint Microace 3 dicing machine and loaded in a hydrogen cell at a pressure of 120 bar for five days before writing to improve photosensitivity.

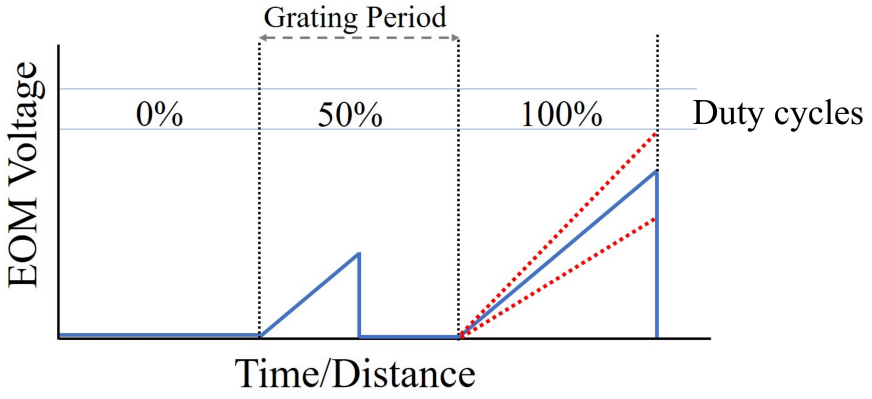

FIGURE 3.2: Schematic of the sawtooth signal at different duty cycles to drive EOM. Red dotted lines show different ramp rates corresponding to peak voltage applied to EOM

Chips for UV writing were placed on an Aerotech four-axis air-bearing stage, which translates the sample through the static UV beams. The stage uses glass encoders to

provide nanometer-resolution feedback to the stage driver to control the position of the stage. The feedback is also used to generate a position-synchronised output (PSO), which generates electrical trigger pulses at pre-programmed positions. Software controls the location of these firing positions in such a way to match the grating period being written.

An integrating amplifier is used to convert the trigger signal from the PSO to a sawtooth wave, which drives the EOM via a high-voltage amplifier, as shown in Fig. 3.2. The slope of this sawtooth wave, often referred to as ramp rate, is controlled to translate the interference fringes at the same velocity as the sample. Once the UV fringes have translated a single grating period, the fringes jump back to the original position. A key advantage of small spot DGW is the control of the written period, which allows the fabrication of gratings with different grating periods to that of the inherent UV interference fringe period – the PSO firing positions defines the grating period. However, the bandwidth of the period detuning is finite and is defined by the spot diameter in the writing direction. In this work, the fabrication parameters are pre-programmed in G-code, a standard computer programming software. Precise fabrication of gratings requires calibration and knowledge of the system's operation. The following section details the experiments to calibrate the system.

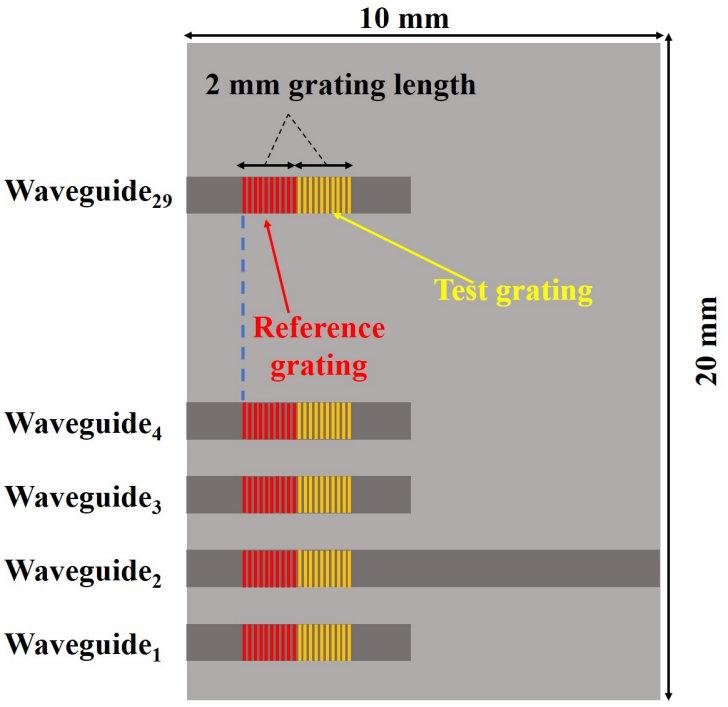

FIGURE 3.3: Schematic of methodology used for writing reference and test gratings.

3.2 Ramp voltage and duty cycle calibration

To achieve the highest modulated refractive index, the gradient of the saw-tooth signal must match the translation speed of the sample. This ramp rate is controlled by an analogue voltage supplied to the integrator circuit and is calculated using the combination of the grating period, stage translation speed and a calibration factor. Translation speed

and grating period are computed within the G-code program and are dependent on the selected writing fluence and target grating wavelength. The ramp calibration factor is a parameter which controls the peak voltage applied to EOM and can be changed to optimise the gradient of the sawtooth wave [2].

Another factor affecting modulated refractive index is the duty cycle of the sawtooth function, as shown in the Fig. 3.2 This is defined as the ratio of the time (or distance) the EOM signal is integrating during one grating period. A duty cycle of 100% fully synchronizes the fringe and stage translation, producing the strongest grating modulation, while 0% corresponds to an off state in which no gratings are created. In reality, the finite slew rate of the high voltage amplifier limits the duty cycle to slightly less than the theoretical 100%. The duty cycle provides a convenient route to apodise and restrict the local modulation of the refractive index.

The modulated refractive index was optimised through experiments that determined the best parameters for driving the EOM and the relationship between the duty cycle and refractive index modulation. Two chips were UV written with a series of integrated waveguides to characterise the required voltage for EOM and duty cycle. The waveguides contained two 2 mm long uniform gratings with central Bragg wavelengths at 1540 and 1560 nm. Two 80 mm planoconvex lenses were used to focus the UV beams, producing spot diameters of 7.4 µm, measured using a knife-edge technique. In each waveguide, the 1540 nm grating served as a reference, and the ramp calibration factor was kept constant, whereas the parameter under test was varied for the 1560 nm test gratings, as shown in Fig. 3.3. The gratings were fabricated with a duty cycle of 100%. In order to minimize the effect of hydrogen out-diffusion on the photosensitivity of the sample, writing time was reduced by minimizing the length of the waveguides. In these tests, the laser fluence was maintained at 0.3 kJ cm^{-2} with an average laser power of 1 mW (at the surface of the chip) and a 30 kHz repetition rate.

3.2.1 Characterisation method

For characterisation, an Er-doped fibre ASE source was launched into the UV-written waveguides. A polariser oriented to the principal axis and polarising maintaining fibre V-groove assembly as shown in Fig. 3.4 were used to ensure only the TE polarisation was coupled into the device. All data presented in this report is from the TE mode of the planar waveguides.

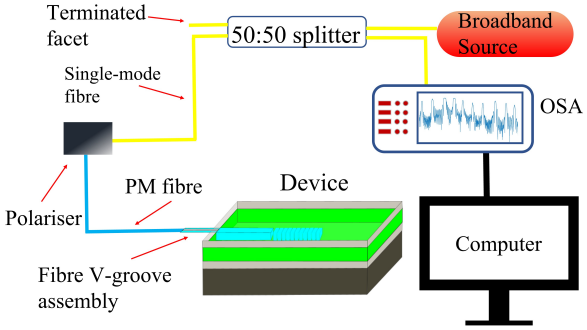

FIGURE 3.4: Schematic of the Characterisation setup to obtain reflection spectra from UV written device.

A 3dB fused fibre coupler was used to collect the reflected light, and the grating spectra were measured on an optical spectrum analyser (OSA).

3.2.2 Analysis of grating response

After grating characterisation, the spectral response was fitted using a Gaussian distribution to obtain the peak reflectivity from each grating. To obtain the trend of grating reflectivity with varying EOM drive voltage, the peak reflectivity of the 1560 nm grating was referenced with respect to the reflectivity of the associated 1540 nm grating. This relative measurement removes any additional errors due to coupling loss at the fibre-chip interface due to misalignment or facet defects.

A chip was designed to explore the optimum ramp rate for the EOM. A total of 29 waveguides were written, varying the peak voltage for the 1560 nm test gratings from 0.6 to 5.3 kV. The differing peak voltages were tested in a pseudo-random order to reduce the effects of any sample misalignment or hydrogen outgassing effects that may cause additional errors in the results. Fig. 3.5 shows normalised reflectivity as a function of peak voltage applied to EOM. The error bars in the plot show the percentage standard error, estimated from the waveguides and gratings written with the same experimental parameters. The maximum gratings reflectivity are observed at a peak voltage of 3.5 kV applied to EOM at 100% duty cycle. In a similar UV writing system using a 244 nm laser, the same size DKDP EOM requires 4.2 kV peak voltage to obtain full-cycle translation [2].

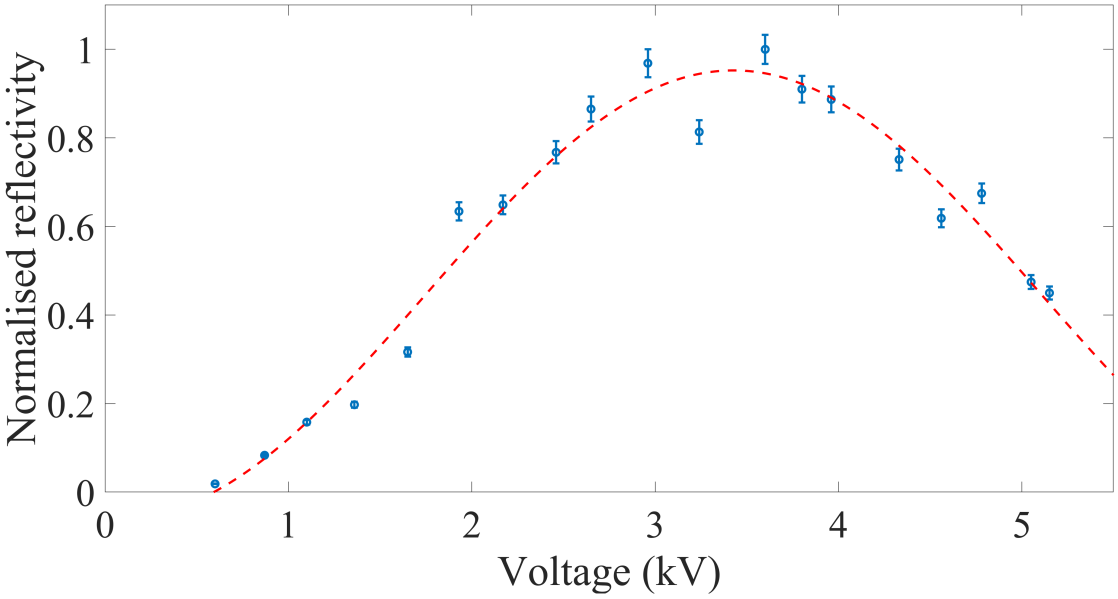

FIGURE 3.5: (a) Testing of EOM driving voltage in order to get maximum grating contrast and reflectivity carried out by 2 mm long uniform gratings. The trendline is plotted using a sinusoidal function to obtain the voltage corresponding to maximum grating strength.

Another planar chip was written to investigate the relationship of the duty cycle to refractive index modulation. This device uses a similar methodology as previously. However, all gratings were written with the peak voltage to EOM of 3.6 kV, whereas the

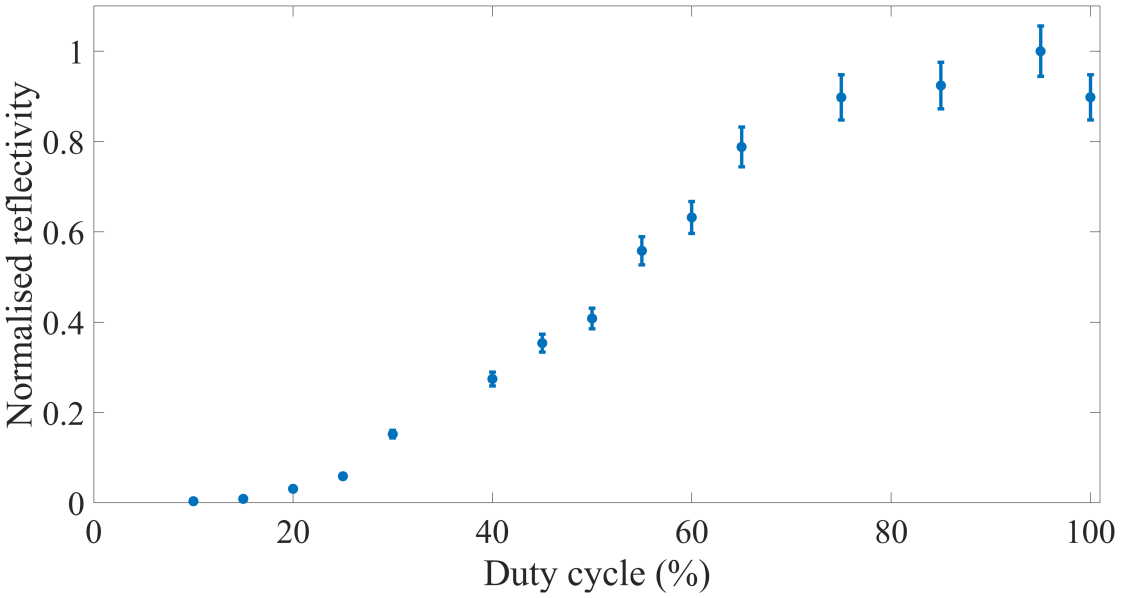

FIGURE 3.6: Plot of a duty cycle test by writing a chip with waveguides and 2mm long uniform gratings.

duty cycle for the 1560 nm grating was varied between 5% and 100%. Again the reference grating at 1540 nm has a fixed duty cycle of 100%. Fig. 3.6 illustrates the behaviour of the normalised reflectivity as a function of increasing the duty cycle. Reflectivity increases with an increasing duty cycle up to 70 %, from whereon the reflectivity saturates, and rising duty cycle does not improve the grating contrast. The grating written with 5% duty cycle was too weak to observe spectrally. The same trend has been observed for 244 nm DGW [1], and a recent study explains the origin of this S-shape trend (paper in preparation by Rex Bannerman). When using the duty cycle to control the apodisation of gratings precisely, knowledge of this transfer function is critical for achieving high-quality gratings.

After calibrating the 213 nm dual-beam grating writing setup, a chip was fabricated with 1.5 mm long uniform and gaussian apodised gratings. Fig. 3.7 shows a photograph of the planar chip containing eight waveguides with gratings to produce a spectral response between 1520 nm and 1590 nm UV written at different fluences. The image shows the strong diffracted nature of gratings and provides a quick, crude method to check for successful fabrication. The assorted observed colours are due to the different grating periods and the incidence angle dependence of the white light illumination source. The apodisation profiles of the gratings are visible.

3.3 Device characterisation via Bragg grating interrogation

This section will use the Bragg gratings as a route to characterise the UV written devices. The first investigation looks at the effect of laser fluence on the waveguide and grating properties.

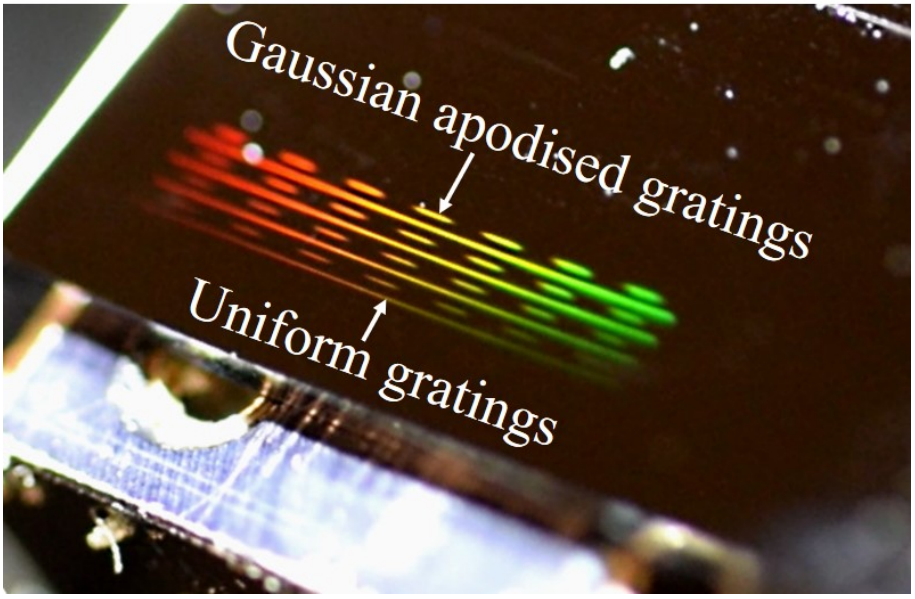

FIGURE 3.7: Photograph of UV written chip taken during characterisation, which shows a colourful scattering of white light illumination source from 1.5 mm long uniform and Gaussian apodised gratings.

The detuning bandwidth is then investigated, and finally, the integrated Bragg gratings will be used to measure the waveguide propagation losses. The previously discussed experiments were performed with an average laser power of 1 mW, and the resulting chips demonstrated high-quality gratings without any observable surface damage. For the next investigations, it was necessary to fabricate longer waveguides containing multiple gratings. For faster fabrication, to minimize the effect of hydrogen outgassing, we increased the laser power by lowering the repetition rate of the laser from 30 kHz to 25 kHz. In order to avoid the damage threshold of FHD silica, the 80 mm UV focusing lenses were replaced by 100 mm. The resulting focused laser beam had a spot size of 8.2 µm.

3.3.1 Fluence test

The fluence of the laser is defined as the total energy deposition per unit area inside a focused spot of two crossed beams. In the writing code, the fluence is calculated by using the following relation.

$$F = \frac{I_{\mathrm{UV}} \times d}{V_{\mathrm{trans}}} \tag{3.1}$$

Here, $\mathrm{I_{UV}}$ is the average intensity of UV laser in kW, d is the spot diameter of laser in cm, $\mathrm{V_{trans}}$ is the translation speed of the sample in cm $\mathrm{s^{-1}}$ and F denotes laser fluence in kJ $\mathrm{cm^{-2}}$.

Prior DUW with 213 nm light suggests a similar fluence response to 244 nm DUW; a linear trend followed by saturation of the photosensitivity mechanism [2], [3]. Previously the fluence response was estimated from the waveguide mode size and numerical aperture measurements. The ability to write Bragg gratings allows a precise measurement of the

induced refractive index change. To perform a fluence test, another chip was written with a 1 mm long uniform grating at 100 % duty cycle, with a reference grating approach used in section 2.1. Writing fluence for each test grating was varied by manipulating the stage translation speed from 0.03 kJ cm^{-2} to 4.5 kJ cm^{-2}. Each written waveguide starts with the same fluence of 1 kJ cm^{-2}, the same as the reference grating. The remaining waveguide and test grating were written with a fluence ranging for 0.03 to 4.5 kJ cm^{-2}. This experiment used an average UV laser power of 2 mW.

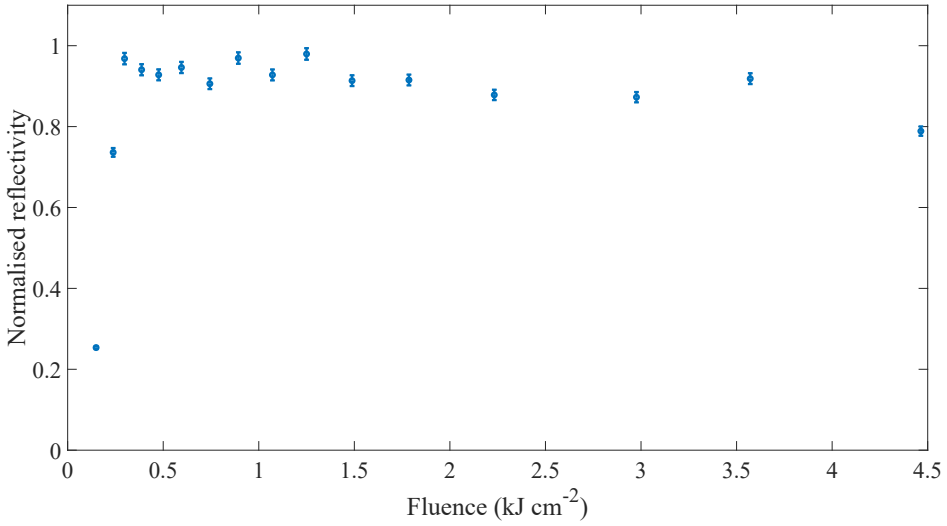

FIGURE 3.8: Fluence curve for a chip written 1mm long uniform gratings, which shows the behaviour of reflectivity at 100 % duty cycle and various fluences.

Fig. 3.8 illustrates the resulting measurements of normalised relative reflectivity (as previously defined) as a function of writing fluence. At low fluences, the linear trend in reflectivity is expected with the increasing fluence up to 0.3 kJ cm^{-2} (see section 3.3.1.1 for details). At high fluences ranging form 0.3 to 4.5 kJ cm^{-2}, reflectivity covers a flat region where no noticeable variation is observed. The origin of the saturation, at fluences above 0.3 kJ cm^{-2}, can be explained by looking at the estimated reflectivity of the gratings. The reflectivity of the test grating was referenced to the 3.3% reflection of the polished connector facet prior to the V-groove assembly. This reference provides an approximate estimate of the absolute reflectivity of the grating and does not consider the coupling and propagation loss. Fig. 3.9 shows the estimated reflectivity of the test grating written with a fluence of 0.3 kJ cm^{-2}. Surprisingly, the spectrum shows a peak reflectivity of 86%, despite the grating only being 1 mm in length. This high reflectivity of the gratings provides a poor regime for interrogating the properties of the grating and explains the saturated response observed in Fig. 3.8.

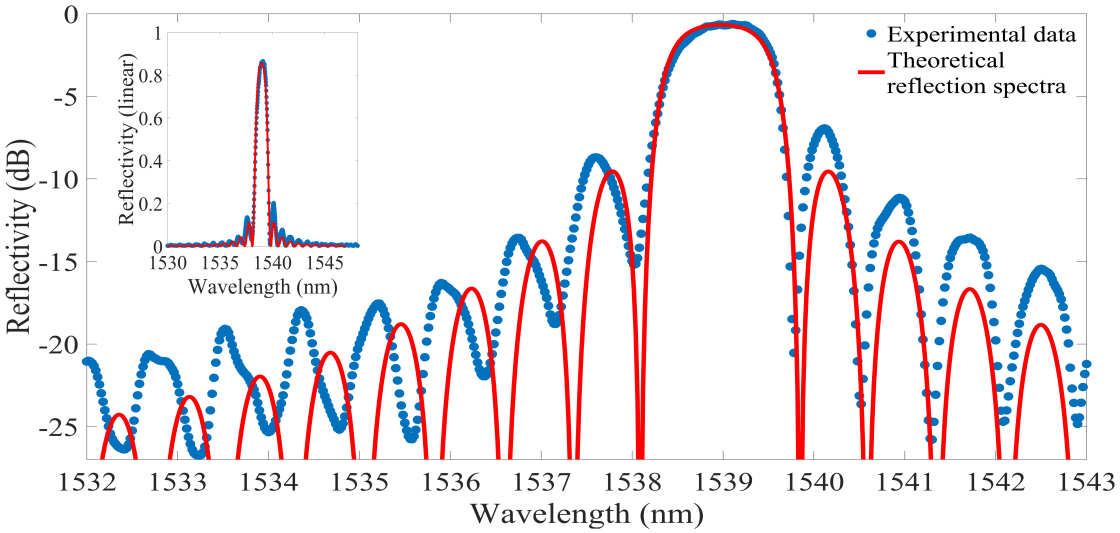

FIGURE 3.9: Example spectrum of a grating written with 100% duty cycle and laser fluence of 0.3 kJ cm^{-2}, showing reflectivity (dB) normalised to 3.3% reflection of the polished connector. Inset shows the same data on a linear scale and a peak reflectivity of 86%. In both plots, experimental data points are shown in blue and theoretical reflection spectra of an ideal uniform Bragg reflector is plotted in red. The theoretical reflection spectra fit nicely at central peak and the side lobes at higher wavelengths of the Bragg grating. However, the experimental data at the shorter wavelengths is slightly out-of-phase possibly due to the cladding modes originating from a strong (flat-topped) grating and Fabry–Pérot cavity effect.

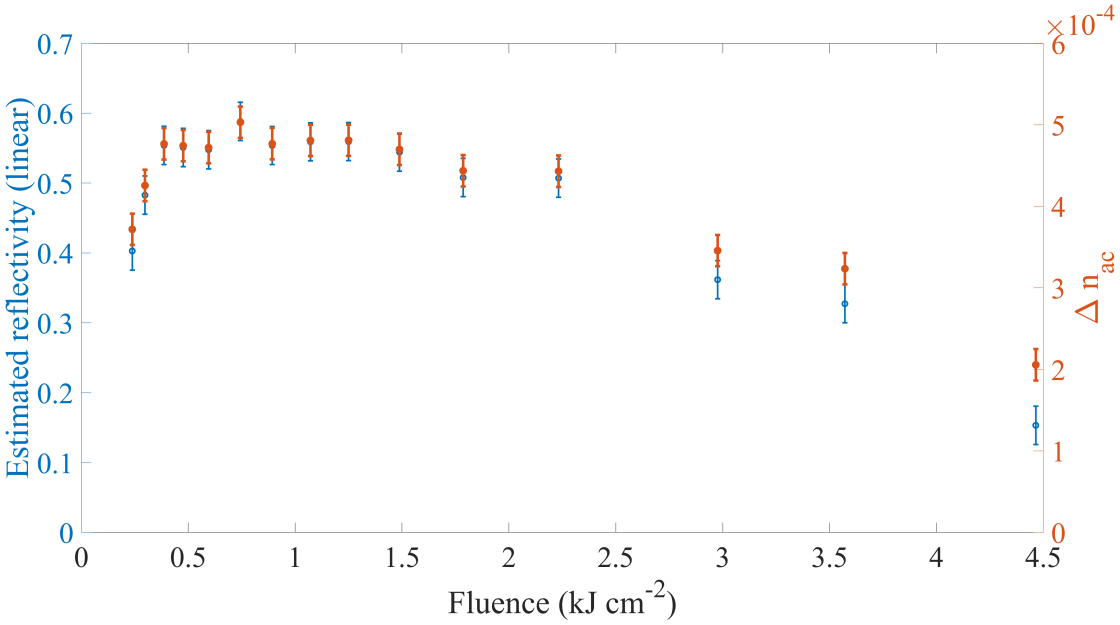

FIGURE 3.10: Fluence dependence of gratings strength for a chip written 1mm long uniform gratings, which shows the behaviour of reflectivity at 50 % duty cycle and various fluences.

The fluence test was repeated to avoid saturation. The same experimental parameters were used, except the duty cycle, which was reduced to 50% to reduce the grating contrast. Fig. 3.10 shows the estimated reflectivity (without considering the coupling

loss) from the revised device at various fluences ranging from 0.15 kJ cm^{-2} to 4.5 kJ cm^{-2}. The second y-axis also shows the modulated refractive index (Δn_{ac}), which is calculated from the estimated reflectivity using coupled-mode theory [4]. The reflectivity increases linearly with fluences up to 0.39 kJ cm^{-2} and then ceases until 1.19 kJ cm^{-2}. This termination is not due to grating reflectivity saturation, as shown in Fig. 3.9; it is associated with the saturation in photosensitivity. For fluences above 1.19 kJ cm^{-2}, a gradual reduction in reflectivity is observed.

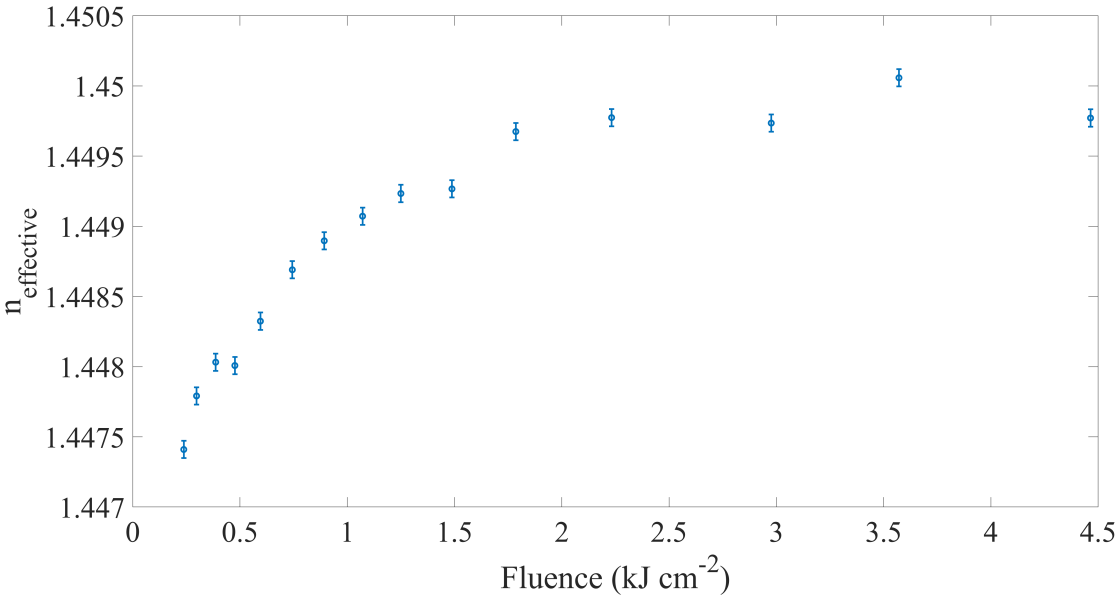

FIGURE 3.11: Plot of the effective refractive index of the optical mode as a function of laser fluence.

The reflectivity trend in Fig. 3.10, can be better understood by looking at the effective refractive index (n_{eff}) of the waveguide, which is calculated from the central Bragg wavelength and fabricated grating period. Fig. 3.11 plots the test grating n_{eff} against laser fluence. At fluences below 1.19 kJ cm^{-2}, a nearly linear trend is observed, after which the photosensitivity begins to saturate. Beyond fluences of 2.98 kJ cm^{-2} no appreciable change is noted; this corresponds to a maximum UV-induced effective refractive index change of $3.3x10^{-3}$. With a 244 nm laser, we have observed the same change in refractive index at saturation. The trend and magnitude of the refractive index change are also similar to that of 244 nm DGW using a continuous wave laser source [2]. The photosensitivity saturation, seen in Fig. 3.11, explains the grating reflectivity observed in Fig. 3.10. At low fluences ($<$ 0.39 kJ cm^{-2}), a linear photosensitivity response generates a linear increase in modulated refractive index (Δn_{ac}). As the photosensitivity begins to saturate, at 0.39 kJ cm^{-2}, the increasing fluence does not increase the net grating modulation, resulting in a termination of the reflectivity. As the nonlinear response increases above 1.19kJ cm^{-2} the modulated refractive index (Δn_{ac}) depletes, and so does the reflectivity. The reflectivity trend increases linearly with the increasing fluence up to 0.3 kJ cm^{-2}, and then it follows the saturated regime from 0.3 to 4.5 kJ cm^{-2}. The (Δn_{ac}) in Fig. 3.10 was analytically calculated from gratings reflectivity without incorporating the coupling loss. The actual (Δn_{ac}) was numerically estimated (see Fig. 3.12(a)) by plotting theoretical reflection spectra on the top of experimental data points. Figure 3.12)(b) shows the numerically estimated Δn_{ac} for a fluence range of 0.15 to 4.5 kJ cm^{-2} at 50 and 100 % duty cycle.

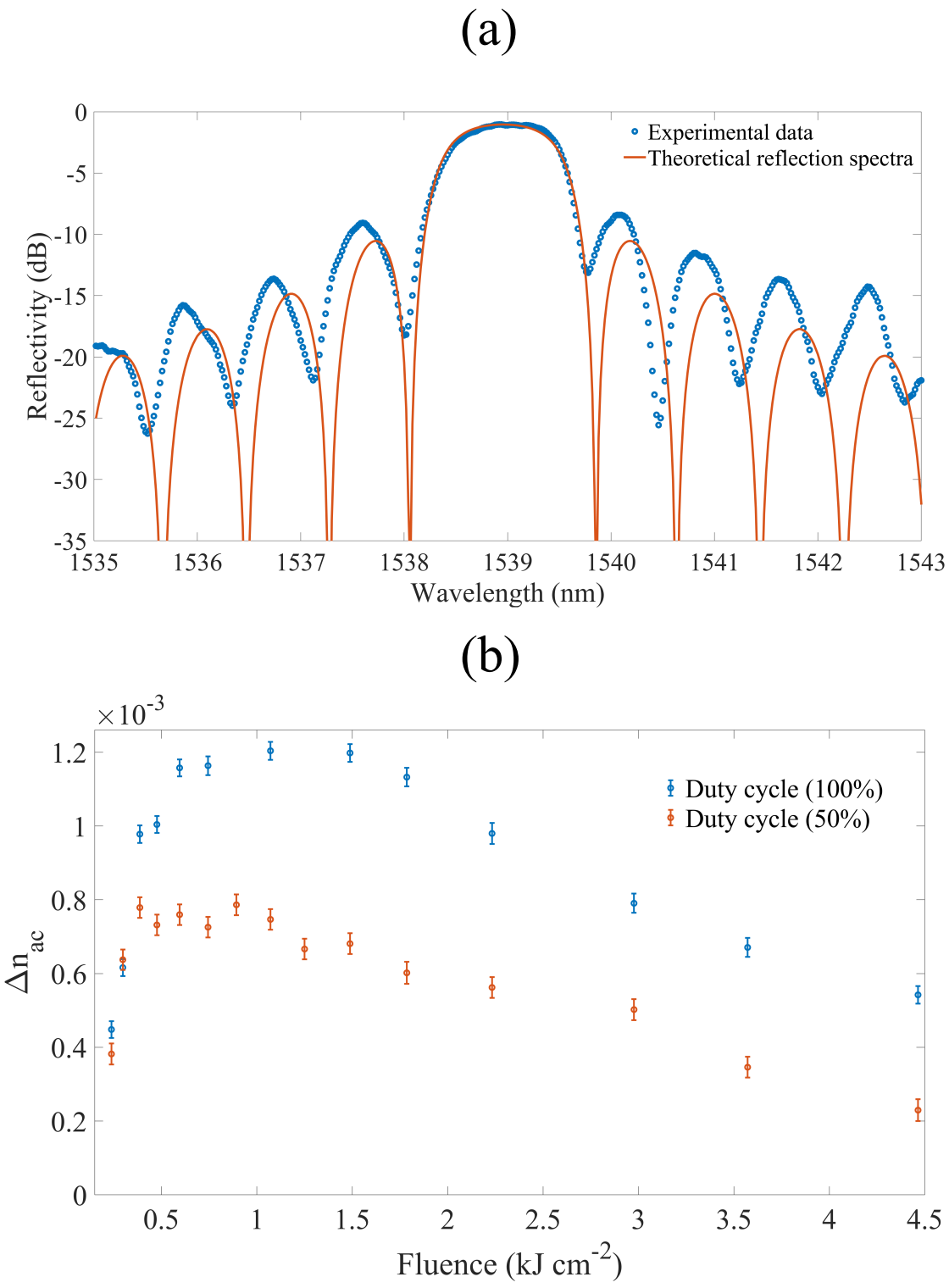

FIGURE 3.12: (a) In this plot, reflection spectra measured for 1 mm long gratings is shown in red and the theoretical reflection spectra of an ideal uniform Bragg reflector is plotted in blue.(b) Plot of Δn_{ac} (estimated using Rouard's method) as a function a laser fluence at 50 % and 100 % duty cycle.

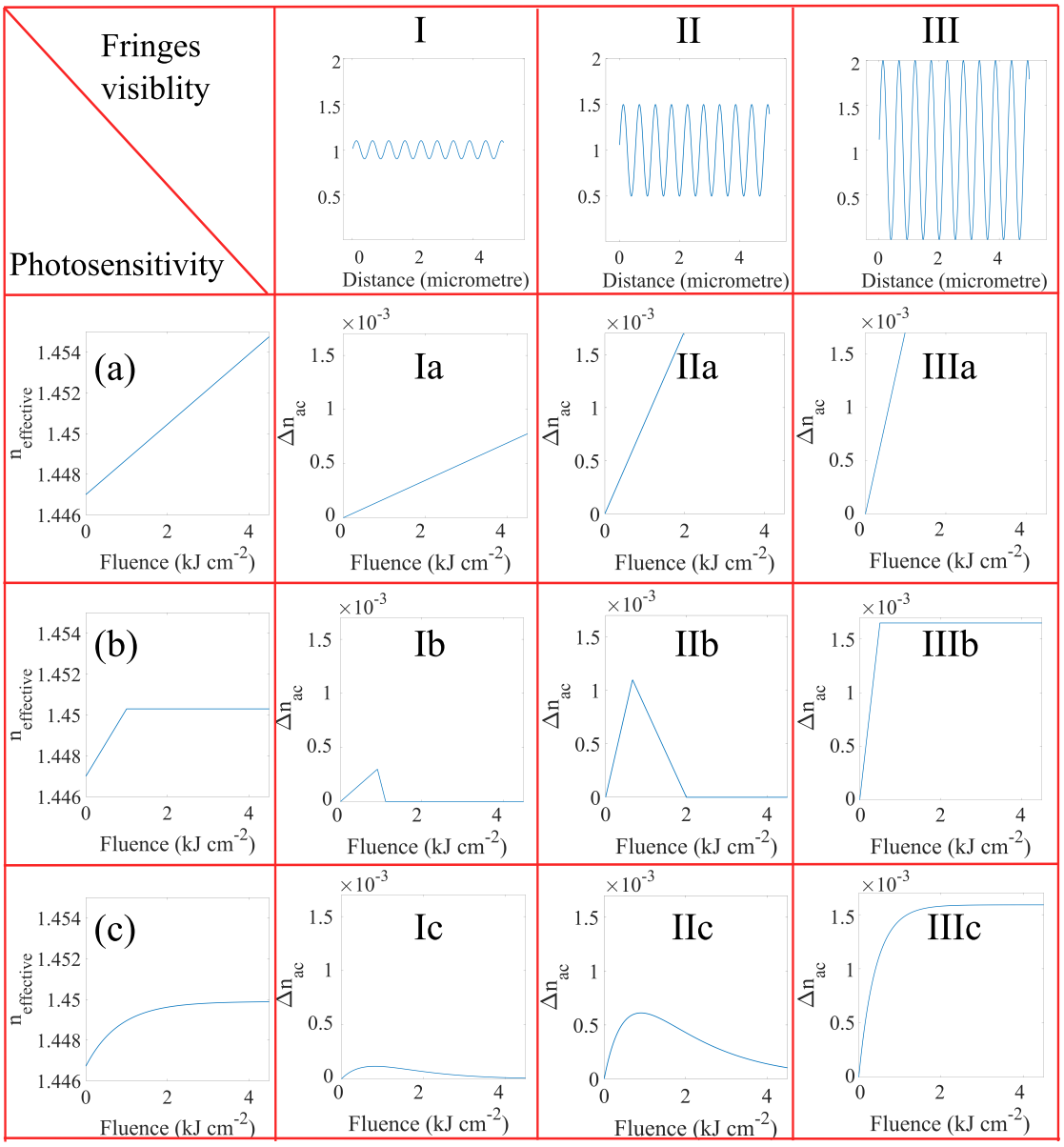

FIGURE 3.13: Demonstration of an intuitive model to investigate the relation between photosensitivity of material and gratings response. Three different cases (a,b,c) of photosensitivity were modelled, weak (10 %), medium (50 %) and perfect (100 %) fringe visibility in (I,II,III) respectively and the modelled results are demonstrated in a 3×3 matrix.

3.3.1.1 Intuitive model for understanding the relationship between photosensitivity and grating response

In the fluence test, we have seen an interesting relation between the variation in the effective index of the waveguide (n_{eff}) and the modulated refractive index of the gratings (Δn_{ac}). In order to gain an intuitive understanding of the relationship between photosensitivity and the modulated refractive index as a function of fluence, an intuitive model was explored in MATLAB. A sinusoidal wave was used to model the interference fringes with weak (10 %), medium (50 %) and perfect (100 %) visibility. Both n_{eff} and Δn_{ac} at different fluences were extracted through the modelled function. Three

different types of photosensitivity response in Fig.3.13(a,b,c) were investigated against three different scenarios of gratings with weak, medium and perfect fringe visibility in Fig. 3.13(I, II, III) respectively. Due to fluence build-up, the variation in the profile of modelled fringe pattern can be seen in Fig. 3.14.

Case (a) is the ideal photosensitive response, in which the refractive index of the material increases linearly as a function of fluence. The modelled output of Δn_{ac} for the case (a) are plotted in I(a), I(b) and I(c). In case (b), the photosensitive response is

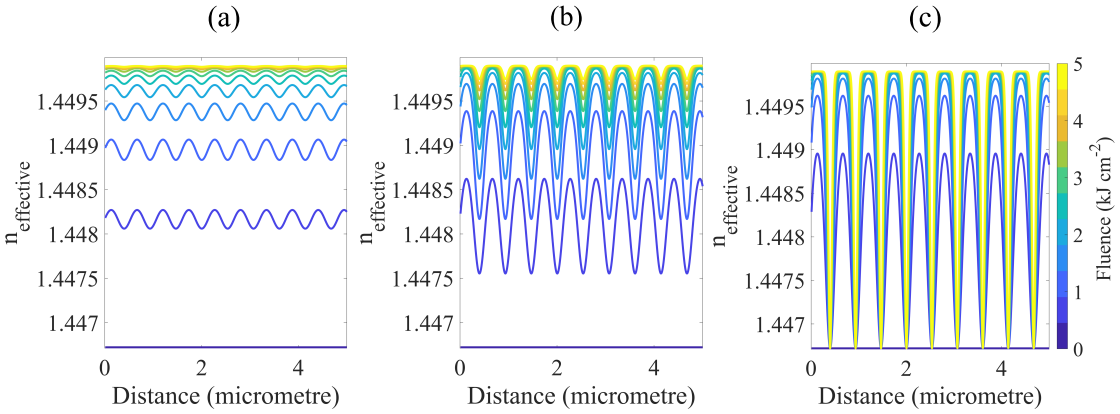

FIGURE 3.14: Demonstration of fluence build-up of localised modulated refractive index at (a) 10 % (b) 50 %, and (c) 100 % fringes visibility.

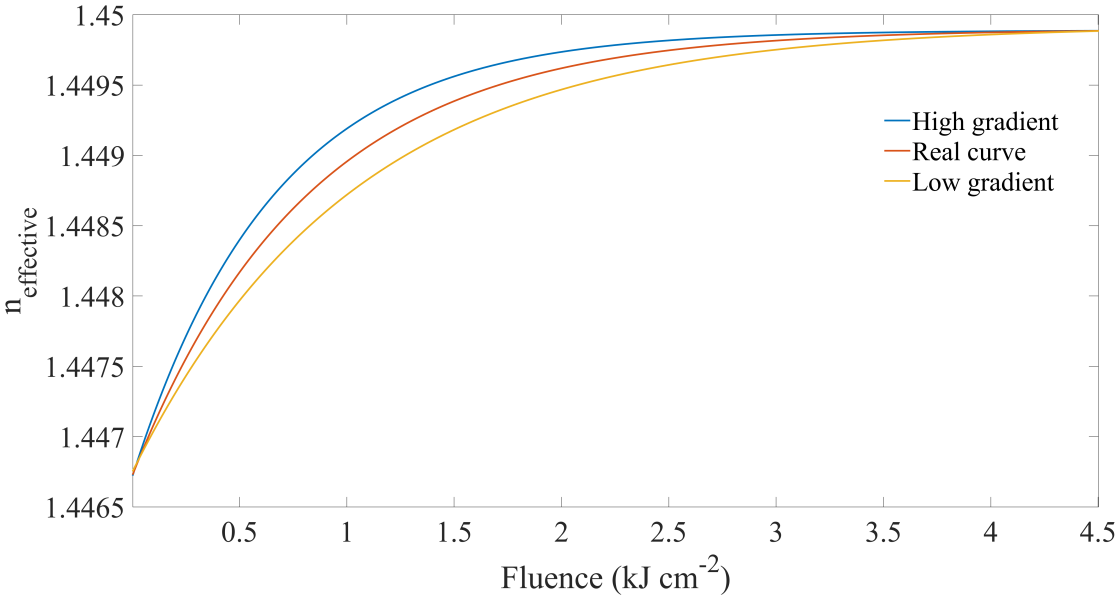

FIGURE 3.15: Graph showing the three different cases of change in the refractive index of a material with increasing fluence. Additional to the real curve, which is the fit of experimental data, two other variations of photosensitivity with different gradients in their linear section are plotted.

linear initially and abruptly saturates. Considering the weak fringe, Δn_{ac} increases linearly with increasing fluence. However, with an abrupt saturation of photosensitivity at the cut-off fluence, Δn_{ac} rapidly drops off to zero as shown in the Fig. 3.13(Ib). A similar response is observed in Fig. 3.13(IIb), where Δn_{ac} increases linearly and starts dropping off linearly at a slower rate opposed to Fig. 3.13 (Ib). From the plot, it

appears that the value of the fluence where Δn_{ac} becomes zero is higher than observed in Fig. 3.13(Ib). In Fig.3.13 (IIIb), Δn_{ac} increases initially, similar to the observed in Fig.3.13 (Ib and IIb)) and then becomes flat. With perfect fringe visibility, case III, the grating strength is maintained even at the higher fluences. In case (c) a realistic

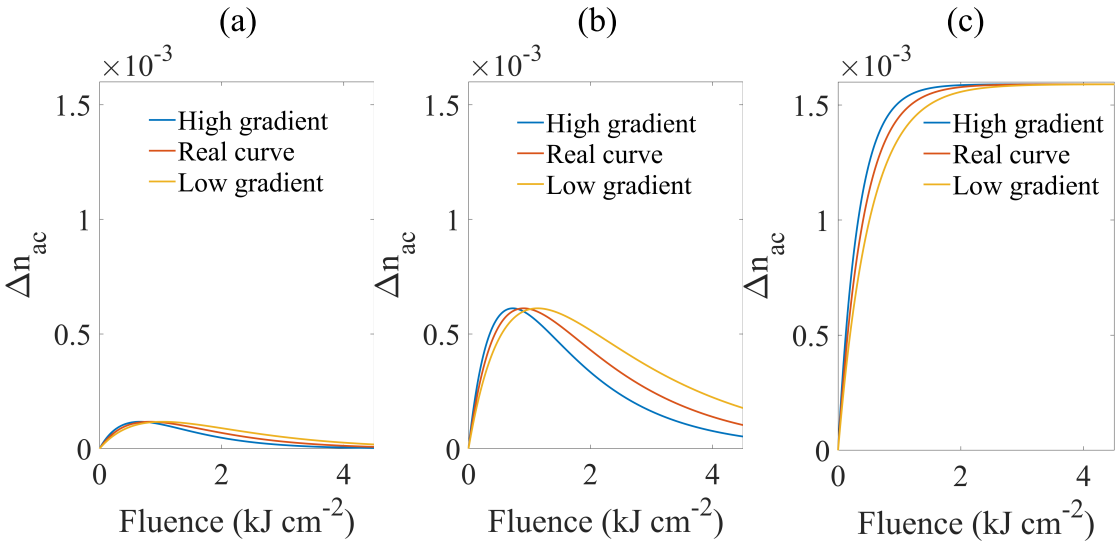

FIGURE 3.16: Plot showing modelled results of Δn_{ac} depending upon the gradient of linear section in the photosensitivity curve at weak, medium and perfect fringe visibility in a,b and c respectively.

response of photosensitivity is considered as experimentally observed in Fig. 3.11. Fig. 3.13(I c) shows a plot of Δn_{ac} as a function of fluence with weak fringe visibility. At low fluences, a linear region in the photosensitivity curve generates a linear increase in Δn_{ac}. As the photosensitivity begins to saturate, the increasing fluence does not increase the net modulation of refractive index and drops nonlinearly at higher fluences. Similar behaviour is observed in Fig.3.13 (Ic). However, when the photosensitivity saturates, the observed depletion of Δn_{ac} is slower than in Fig. 3.13 (Ic) due to the medium fringe visibility. Finally, with perfect grating visibility, photosensitivity saturation leads to saturation in Δn_{ac}, as shown in 3.13 (IIIc). This mechanism can be explained by the same effect observed in (IIIb).

From the previously discussed scenarios of photosensitive behaviour, only case (c)appears to be a matter of interest due to its similarity with experimental data shown in Fig 3.11. Therefore, we decided to look closer at the relationship of Δn_{ac} on the gradient of a linear region in the photosensitivity curve. In Fig. 3.15, three different curves of photosensitivity are plotted, the real curve is a fit of the experimental data. Two other variations with different gradients in their linear section also plotted against fluence. The corresponding Δn_{ac} response to these photosensitivity curves were modelled with weak, medium and perfect fringe visibility and shown in Fig.3.16 (a, b and c) respectively. In a case of weak and medium fringe visibility, Δn_{ac} increases to a maximum value and starts dropping off due to the saturation in corresponding n_{eff} response. However, the fluence range where Δn_{ac} sustains varies for each case depending upon the shapes of n_{eff} curve. In the case of perfect fringe visibility, Δn_{ac} typically follows the shape of photosensitivity observed in Fig. 3.15. Different shapes of photosensitivity response and corresponding gratings strength will be discussed in Chapter 4.

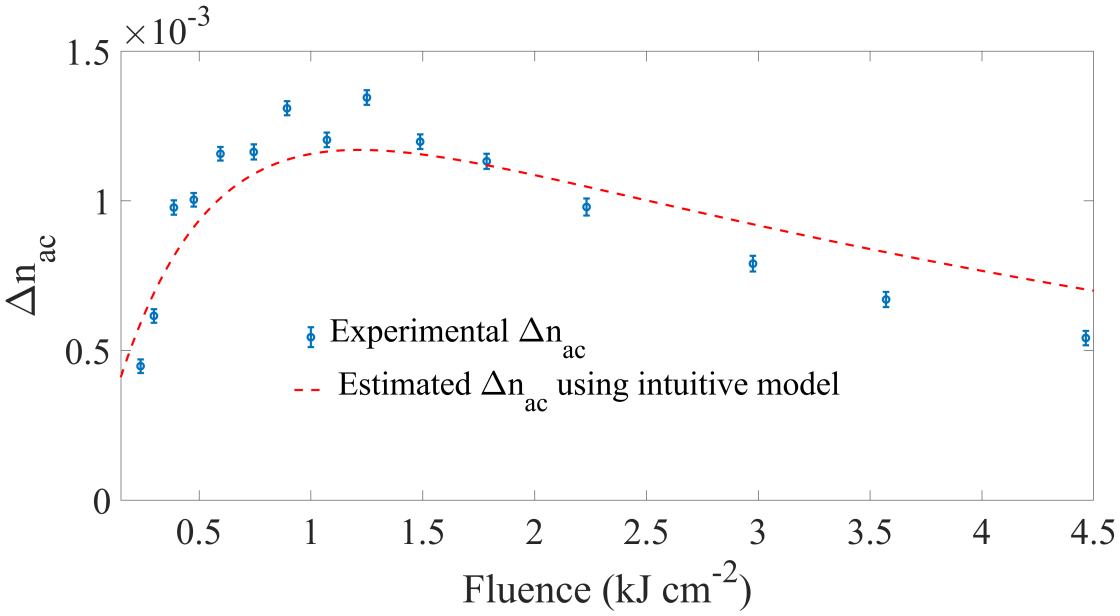

FIGURE 3.17: Experimental results of Δn_{ac} and as a function of fluence are showed by blue line where estimated values of Δn_{ac} using the intuitive model are plotted by red dotted lines.

Intuitive modelling was performed to understand the dependence of the modulated refractive index on photosensitivity. Several models of photosensitivity were explored, and the results show Δn_{ac} generated by the realistic photosensitivity curve considering medium fringe visibility, which best matches our experimental results. This plot agrees with our expectation, as experimentally, we cannot achieve perfect visibility of interference fringes due to the imbalance of laser power in the two beams of the interferometer and alignment of the spots. Fig. 3.17 demonstrates the experimental data of Δn_{ac} and modelled Δn_{ac} with 85% fringe visibility. Using this model, we should be able to verify if this response agrees with the estimated reflectivity. If this relationship differs greatly, this process may provide insight into other effects that reduce the fringe visibility, such as interferometer and stage instability; see section 3.5 for more discussion and experiments. However, this current data looks promising, with the higher fluence data showing no obvious signs of severe reduction in fringe visibility due to the instabilities of the fabrication system. But a more robust model with a numerical package is needed to strengthen that observation. This simple model shows that the trend seen in the reflectivity data agrees with the photosensitivity response extracted from the Bragg wavelength.

3.3.2 Detuning from the central wavelength of 1550 nm

Compared to other UV grating writing techniques, such as phase mask approaches, the small spot DGW technique allows for wide detuning of the grating wavelength over hundreds of nanometers without altering the interferometer [1]. In order to quantify the detuning of this system, a chip was fabricated with a 20 mm long waveguide containing ten 1 mm long uniform gratings. The written gratings were targeted from 1450 nm to 1648 nm with a wavelength interval of 22 nm. The writing was performed at a fluence of 0.27 kJ cm^{-2} and duty cycle of 40% to avoid saturation of the gratings. As previous

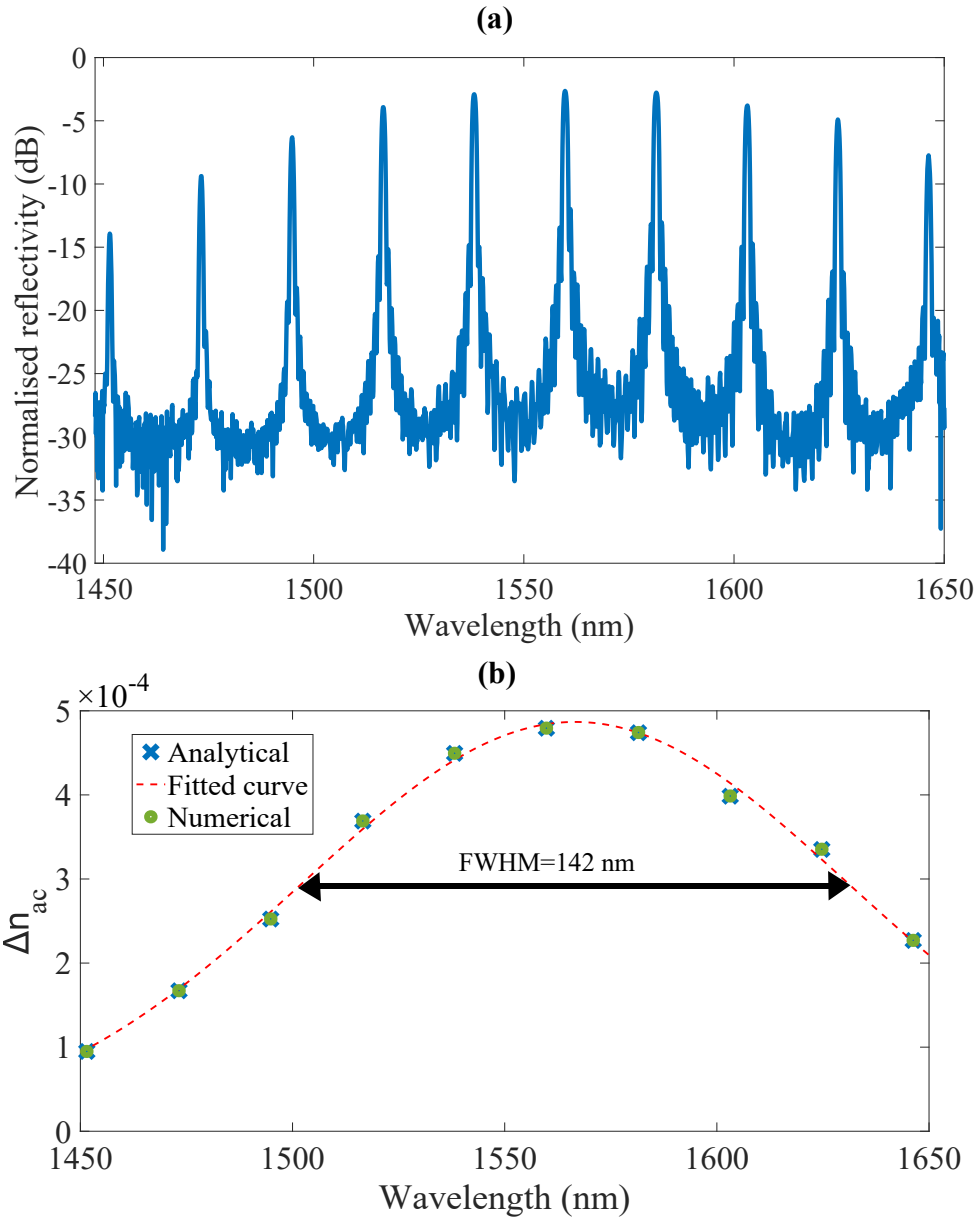

FIGURE 3.18: (a) Reflection spectra from a single waveguide containing ten 1-mm long uniform gratings with central Bragg wavelength from 1450 nm to 1648 nm. (b) Plot showing the spectral dependence of modulated refractive index (Δn_{ac}). Analytical and numerical methods derive these values from the peak reflectivity data in (a). The line is a Gaussian fit to the two sets of data which are indistinguishable.

devices, fabricated with 2 mW of average power, did not show evidence of surface damage, the writing power of the laser was increased to 5.8 mW. The reflection spectrum of the waveguide is presented in Fig.3.18(a) shows a normalised peak reflectivity of 54% for the Bragg grating at 1560 nm and corresponds to an estimated modulated refractive index (Δn_{ac}) of 0.49 x 10^{-3}. As previously, the reflectivity is normalised using the back-reflection from the fibre facet. Despite the number of gratings within the waveguide the spectrum has $>$ 25 dB of noise floor suppression. Fig.3.18(b) displays the Δn_{ac} of each grating plotted against the central Bragg wavelength. The value of Δn_{ac} is estimated both analytically and numerically using a Bragg grating model. Analytical values are calculated by using the peak reflectivity from each grating [4], while Rouard's method

[5] was used to fit a model to the reflection spectrum of each peak. The results from both methods are presented in Fig.3.18(b) and show good agreement. The data is fitted with a Gaussian curve in the frequency domain, which again exhibits excellent agreement and yields a 3 dB bandwidth (FWHM) of the modulated refractive index of 17.7 THz (142 nm). This bandwidth corresponds to a spot size of 6.0 µm and agrees with our spot size estimation in the writing direction (paper in preparation by Rex Bannerman).

3.3.3 Waveguide propagational losses

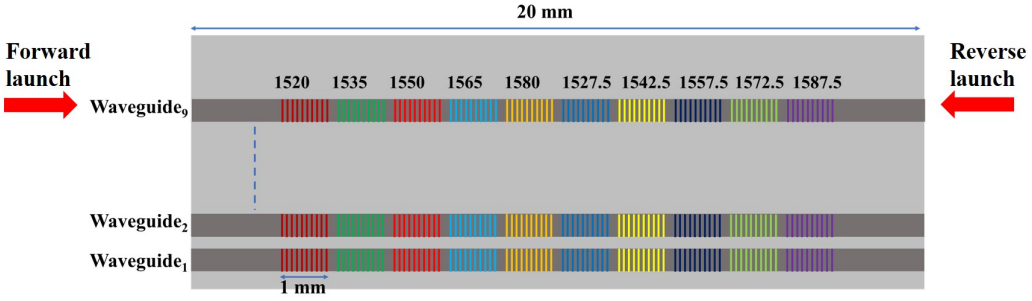

FIGURE 3.19: Schematic of chip fabricated for the loss measurement.

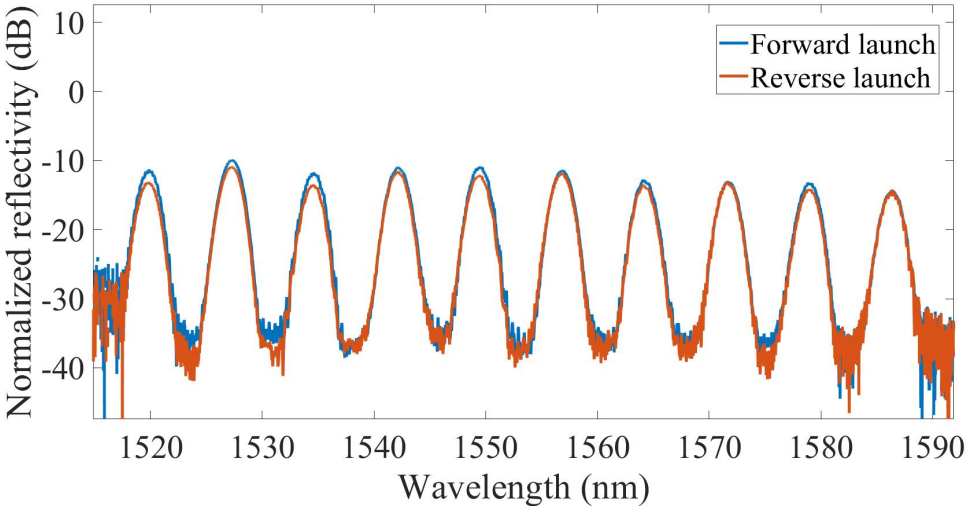

FIGURE 3.20: Shows the obtained reflection from launching light from both end facets of the chip.

Bragg gratings also provide a route to precisely and non-destructively measure propagation loss [6]. To investigate the relationship between fluence and propagational loss, a chip containing 10 waveguides was UV written with varying fluences in a pseudo-random order from 0.06 kJ cm^{-2} to 0.48 kJ cm^{-2}. The waveguides were each 20 mm in length and contained ten 1 mm Gaussian apodised gratings. The gratings had gaussian apodisation and central Bragg wavelengths from 1520 nm to 1590 nm with 7.5 nm spectral spacing. The gratings were written in pseudo-random wavelength order with a 0.5 mm inter-grating spacing, as shown in Fig.3.19. Reflection spectra were obtained as before from each waveguide. In this work reflection spectra were collected from both facets of the waveguides, example spectra from a waveguide with fluence of 0.23 kJ cm^{-2} is

shown in Fig.3.20. Propagational losses in each waveguide were calculated using the technique outlined in [6] and plotted against fluence, shown in Fig.3.21. Error bars on the data points correspond to the calculated error of the linear fit. The plot shows a gradual reduction of loss with increasing fluence. This is expected because higher laser fluences result in a greater change in the effective refractive index, ultimately defining waveguides with higher mode confinement [3]. However, there is a damage threshold for the fluence at a specific laser power. Increasing the laser fluence beyond this threshold could lead to additional scattering losses due to laser-induced damage. The lowest fluence of 0.06 kJ cm^{-2} did not induce sufficient refractive index change to support an optical mode. The lowest propagation loss of 0.28 ± 0.07 dB cm^{-1} was observed at the fluence of 0.23 kJ cm^{-2}. The measured propagation loss is lower compared to previous work, in which the cutback method was used for loss estimation [3]. However, the work here does not consider the optimisation of the mode size as previously [3], which led to the use of higher fluences to achieve the best mode matching to single-mode fibres.

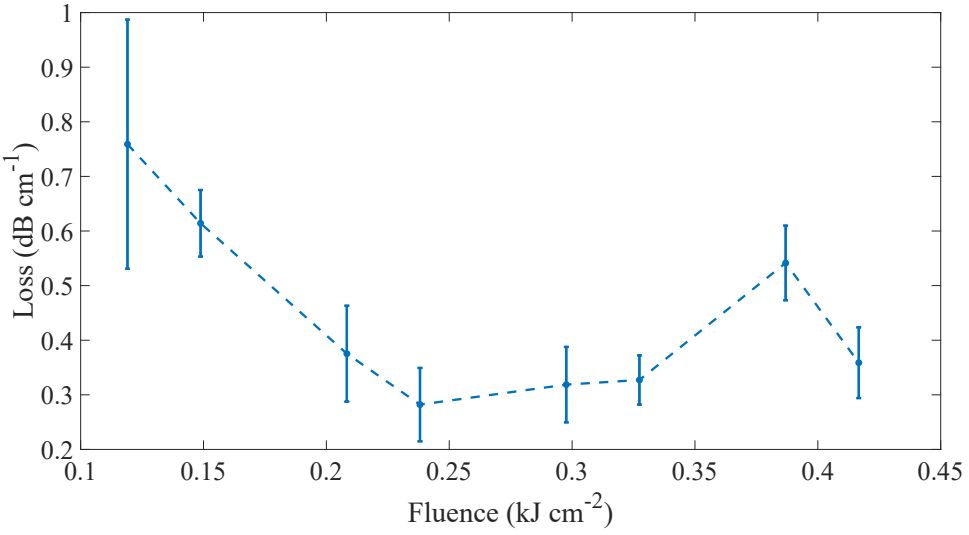

FIGURE 3.21: Illustration the measured propagation loss inside the waveguides at various writing fluences.

3.4 Waveguides and Bragg gratings fabrication in non-hydrogen loaded samples using a 213 nm laser

Previously, all the fabricated devices were hydrogen-loaded before the UV writing. There are a few challenges with hydrogen loading which limit the fabrication of large-area grating structures, especially with longer fabrication time. However, work on FBGs using 213 nm suggests strong gratings can be fabricated without hydrogen loading [7]. Here, we will discuss the fabrication of UV-written planar devices without hydrogen loading.

The conventional direct UV writing technique used in Southampton relies on hydrogen loading to enhance the photosensitivity of doped silica to induce sufficient refractive index change. Hydrogen loading adds extra complexity and time to the process, which requires leaving samples for several days in-diffusing in hydrogen at the pressure of ~120

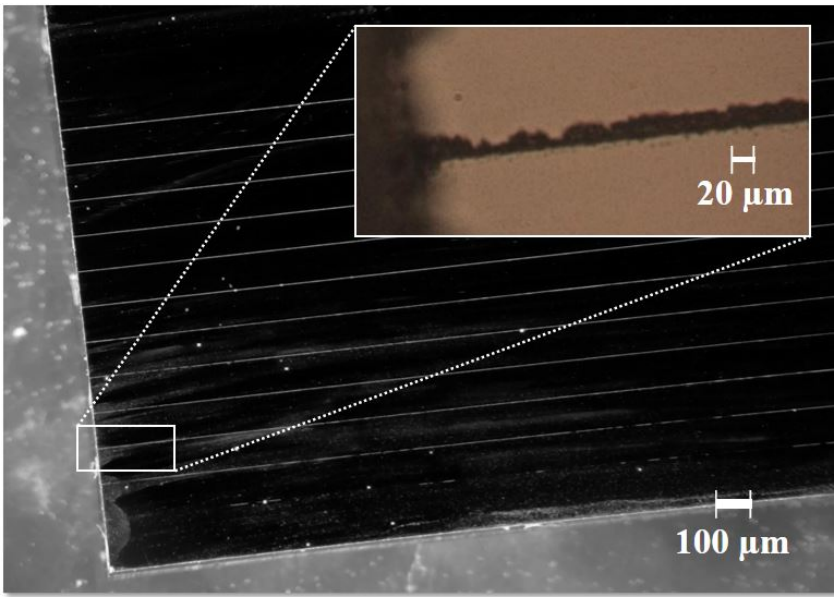

FIGURE 3.22: Optical micrograph of 213 nm UV written waveguides at 4 mW writing power; laser-induced damage is evident by white lines. The inset shows a higher magnification image of a waveguide, clearly showing the high peak power density causing ablation of the silica.

bar [8]. The technique does not only require hydrogen pre-processing, but, hydrogen within the silica samples diffuses during writing, generating a time dependent variation of photosensitivity. Additionally, hydrogen can be depleted during writing adjacent structures in close proximity, a critical artefact when writing the devices such as beam splitters. All these factors play a role in the variation of the final written structures and hence make the fabrication of precise and consistent structures more challenging. By using a system with a cooled stage and a nitrogen purge, it is possible to slow the rate of hydrogen out-diffusion, but this does not stop outgassing completely [9]. Another approach is to lock the hydrogen within silica through thermal processing, allowing the sample to maintain photosensitivity during the whole writing process. But, again this is an additional process that increases inconsistency between multiple batches and can introduce additional losses due to OH absorption within the silica [10]. In 2010, strong Bragg gratings in SMF-28 fibre were achieved without hydrogen loading using a pulsed nanosecond laser source operating at 213 nm wavelength [7]. The gratings were fabricated using a phase mask, and the results showed higher photosensitivity than 248 nm light.

Taking inspiration from the work reported on non-hydrogen-loaded fibre Bragg grating writing, [7], we wish to explore the use of the 213 nm laser source for direct grating writing in hydrogen-free planar silica. However, implementing the DWG technique using a high-intensity pulsed laser source raises several research questions. Previous work by Gow et al. [8] has shown that ∼20 times higher fluence is required to induce similar change index change as hydrogen-loaded samples. However, this work did not contain grating fabrication. Can gratings be written with such high peak power densities while avoiding the damage threshold of silica? And are the writing times suitable for the stability of the system, i.e. the interferometer and stages? To explore this parameter space, we again wrote channel waveguides and Bragg gratings to extract essential information as in section 3.3.1.

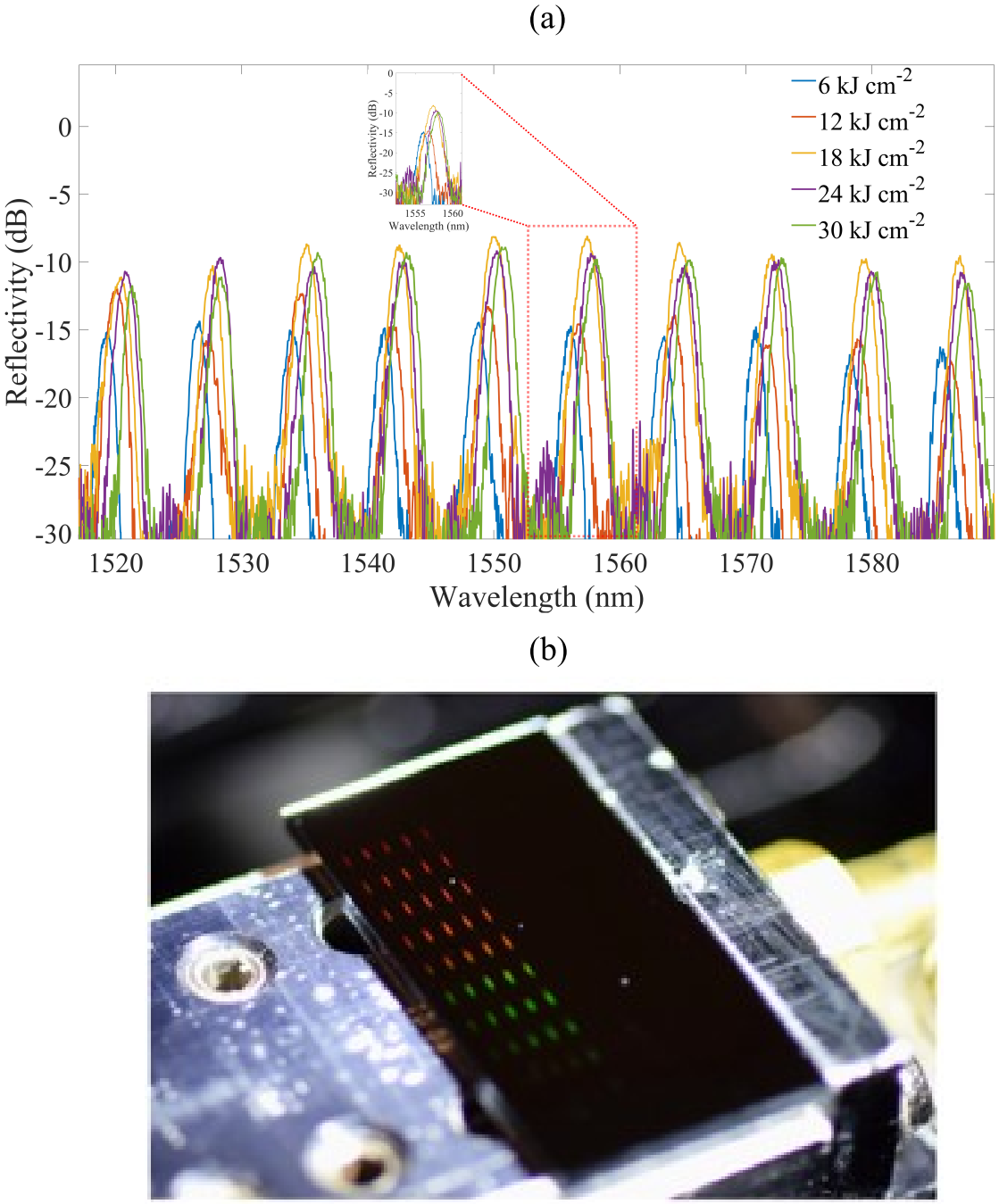

FIGURE 3.23: (a) Reflection spectra obtained from launching light from both end facets of the chip. The inset shows reflection spectra of a single grating fabricated at fluences ranging from 6 to 30 kJ cm^{-2}. (b) A photograph of a fabricated chip taken during characterisation shows the colourful diffraction of white light from the Gaussian apodised gratings.

The first fabrication trials of channel waveguides and Bragg gratings in non-hydrogen-loaded samples used an average laser power of 5 mW. However, the high peak power densities of the pulsed source and the long exposure times led to significant surface damage. Fig.3.22 is an optical microscope image of a chip that contains 213 nm UV written waveguides showing induced surface damage. The inset shows a higher magnification image of a waveguide, clearly showing the ablation of silica. In order to overcome this

challenge, one possibility is to reduce the average power of the laser. Still, writing will require a long exposure time to induce a sufficient change in the refractive index. In such a case, implementation of direct grating writing becomes more challenging due to stability issues of the interferometer over a longer period. Therefore, to employ such high energy sources for small spot grating writing, it is essential to find the optimum fluence and average power of the laser to obtain stable gratings without damaging the surface, especially for non-hydrogen-loaded samples.

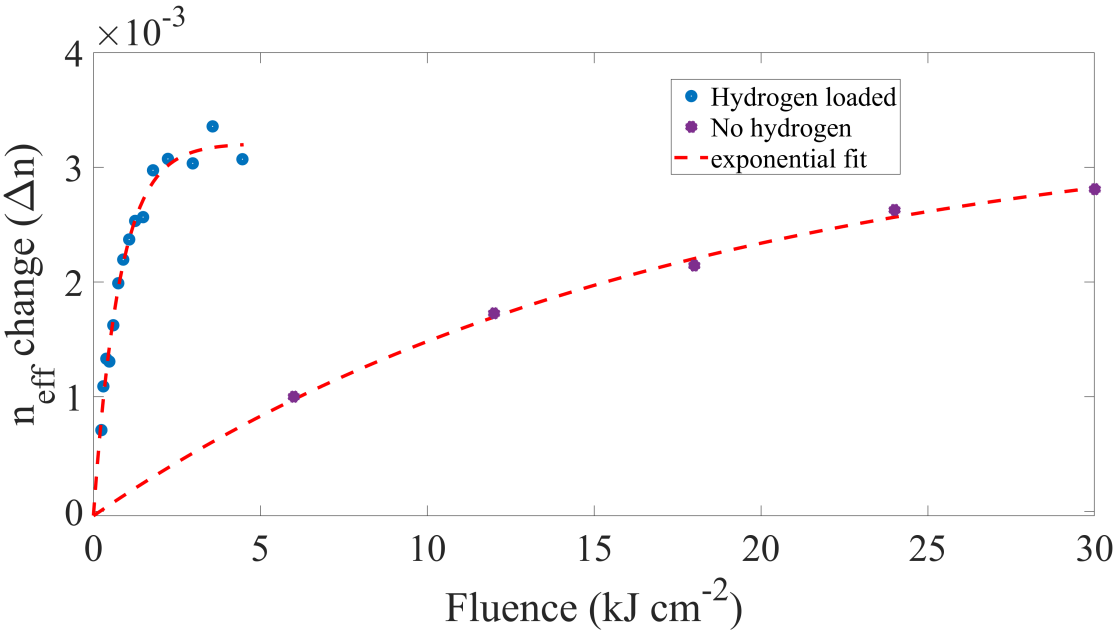

FIGURE 3.24: Comparison of photosensitivity of hydrogen and non-hydrogen-loaded doped silica.

In order to avoid the damage threshold of FHD glass, the average power of the laser was reduced to 2 mW. The experiment was repeated to define waveguides integrated with ten 1.5 mm-long gratings with a fluence range of 6 kJ cm^{-2} to 30 kJ cm^{-2}. The periods of written gratings were changed to produce a spectral response between 1520 and 1590 nm. Higher fluences were required to achieve a sufficient change in the refractive index. The total writing time for the five waveguides was about 17 hours. For characterisation, an Er-doped ASE broadband source was launched into the UV-written waveguides through a fibre V-groove assembly. The reflected grating spectra were collected on an optical spectrum analyser. Investigations using optical microscopy showed signs of laser-induced damage on the waveguides written with a high fluence of 24 and 30 kJ cm^{-2} which will be discussed in Chapter 4.

Fig. 3.23(a) shows the reflection spectra obtained from the gratings written at a fluence range of 6 kJ cm^{-2} to 30 kJ cm^{-2}. Fig. 3.23(b) is a photograph of the fabricated chip showing the colourful diffraction of white light from Gaussian apodised gratings. A comparison of the key UV writing parameters and device characteristics of both hydrogen and non-hydrogen-loaded silica is summarised in Table. 3.1. Non-hydrogen-loaded UV writing takes a long fabrication time because the required fluence is two orders of magnitude higher than hydrogen-loaded samples. Additionally, the shape of the photosensitivity response to the laser fluence is significantly different for hydrogen and non-hydrogen-loaded samples; the comparison of both is shown in Fig. 3.24. In

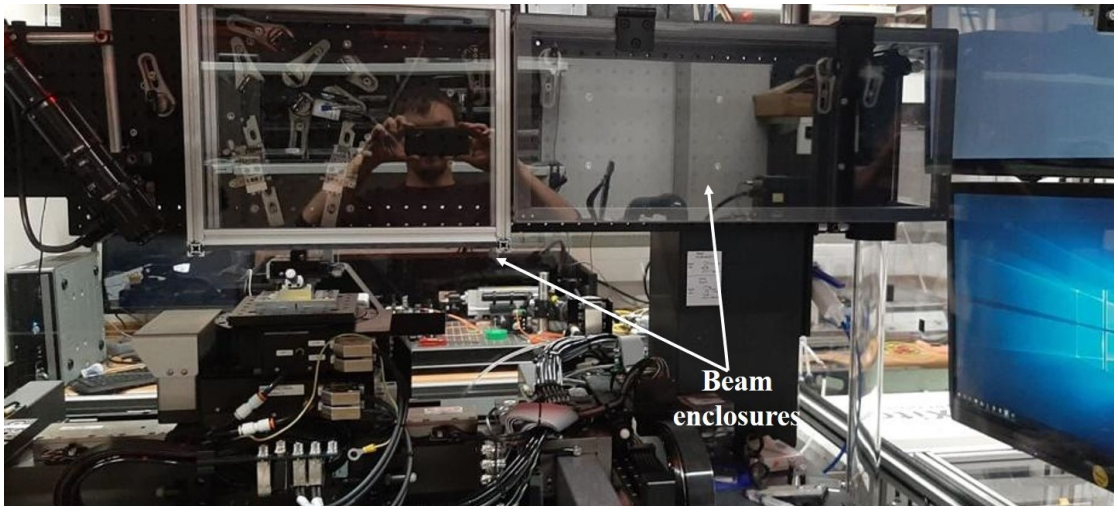

FIGURE 3.25: Photograph of some of the beam enclosures to isolate the beam path and interferometer.

	Without hydrogen	Hydrogen loaded
Average UV Power	2 mW	6 mW
Fluence range	6 kJ cm^{-2} to 30 kJ cm^{-2}	0.06 kJ cm^{-2} to 0.41 kJ cm^{-2}
Writing time for 20 mm waveguide	~17 hours (5 waveguides)	Few minutes (10 waveguides)
n_{eff} change Δn	$2.8x10^{-3}$	$3.3x10^{-3}$
Maximum Δn_{ac}	$0.75x10^{-3}$	$1.25x10^{-3}$
Minimum propagation loss	0.44±0.13 dB cm^{-1}	0.28±0.07 dB cm^{-1}

TABLE 3.1: Comparison based on writing parameters and characterisation of UV written devices with and without hydrogen loading.

hydrogen-loaded UV written devices, the change in the effective refractive index (Δn) increases abruptly and reaches a maximum of $3.3x10^{-3}$ at a fluence of 3.6 kJ cm^{-2}. However, the photosensitivity response in non-hydrogen-loaded UV written devices begins to saturate earlier and obtains a Δn of $2.8x10^{-3}$ observed at a fluence of 30 kJ cm^{-2}. In non-hydrogen-loaded UV written devices, we see a similar response in gratings strength with fluence, as discussed in section 3.3.1. However, due to the early saturation in photosensitivity, the strength of the grating starts to reduce with a peak Δn_{ac} of $0.75x10^{-3}$; the maximum value of Δn_{ac} was $1.25x10^{-3}$ in the hydrogen-loaded samples. In addition to the grating saturation effects, the excessively longer fabrication time may result in grating errors due to the instability of the dual-beam interferometer. The hunting errors from the air-bearing stage system can also lead to phase errors. We expected higher propagation loss in hydrogen-loaded UV-written devices due to the shift in OH overtone. However, the measured loss in non-hydrogen-loaded is double of hydrogen-loaded UV-written devices, possibly due to very high power densities, which lead to damage and possibly scattering defects.

During these experiments, the focus position of the UV laser beam was seen to move on the camera upon the UV writing system. Experiments suggested that environmental

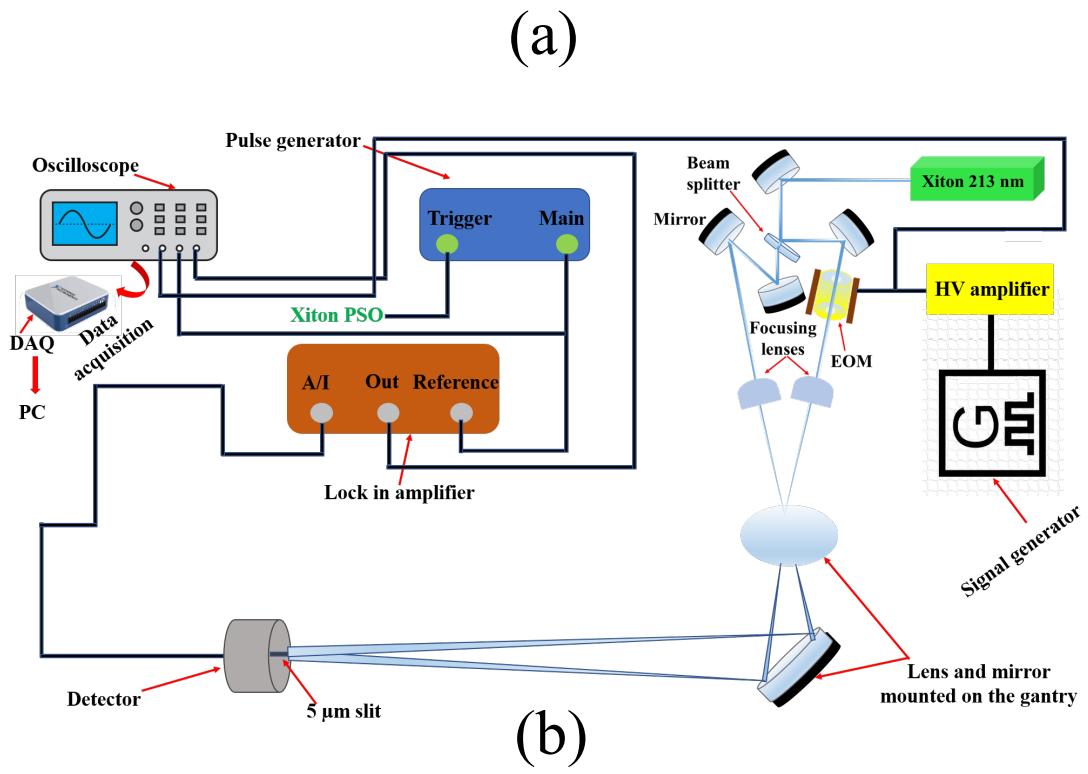

FIGURE 3.26: (a) Schematic of an experimental setup for measuring the fringes stability of interference pattern. (b) Photograph of the experimental setup.

parameters such as humidity, temperature and air currents from the room and air-bearing stages were causing the localised refractive index fluctuations and resulting in beam-pointing instability along the UV beam path. Small beam position fluctuations may not be a significant issue. Still, if the phase of the interference fringes fluctuates over a certain period, it may affect the quality of the gratings. To reduce these effects and improve laser safety, beam enclosures (see Fig. 3.25) are built and installed to enclose the beam path fully.

3.5 Fringe stability measurement

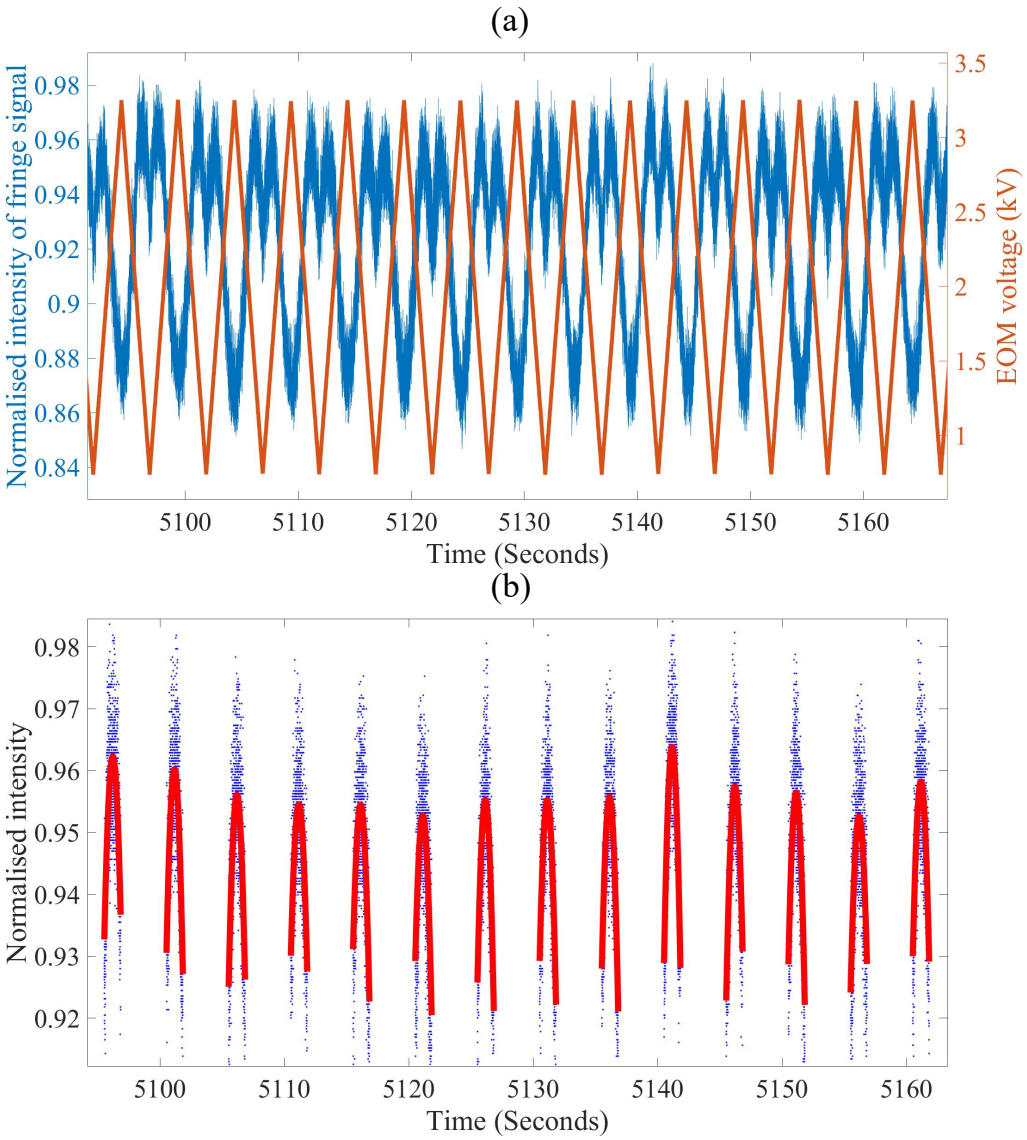

FIGURE 3.27: (a) Variation in fringes signal due to the applied voltage to EOM. (b) Polynomial fit is applied to extract the phase on the noisy signal of interference fringes.

In order to check the stability of the interferometer, an experimental setup was designed to investigate the fringe stability of the interferometer with respect to time. To magnify and reimage the interference pattern, a 25 mm planoconvex lens and a 45-degree mirror were mounted on the gantry in such a way that after reflecting from the mirror both beams focused onto a GaP detector (with a 5 μm slit), see Fig.3.26. The path lengths of the optical system provide ~40 times magnification. Hence the ~0.5μm period of the interference pattern becomes ~20μm. A signal generator was used to drive the EOM, translating the interference pattern by using a triangular waveform at a rate of 0.2 Hz. The output from the detector was fed into a lock-in amplifier with the laser pulse trigger signal (25 kHz), which was used as the reference. The output signals from the EOM high voltage amplifier and lock-in amplifier were collected via a LabVIEW program using a data acquisition card.

	Phase variation	Time
Case (1)	$\sim\pi/4$	1 hour
Case (2)	$<\pi/2$	1 hour
Case (3)	$\sim \pi/60$	1 hour

TABLE 3.2: Comparison of phase stability at three different environmental conditions.

Fig. 3.27(a) shows the waveform of the EOM driving voltage and the corresponding fringe signal as a function of time. The data shows that in a half cycle, as EOM driving voltage goes up, the interference fringes translate in one direction and when voltage comes down the fringes move in the opposite direction to the slit. A code in MATLAB was written to obtain the peak data from each half cycle of the fringe signal and a polynomial fit was applied to extract the phase (see Fig. 3.27(b)). The following cases were considered for investigation of the phase stability of fringes with respect to time.

Case (1): Beam enclosures open and stages off (stages off means no floating air across the stages)

Case (2): Beam enclosures closed and stages off

Case (3): Beam enclosures closed and stages on

Fig. 3.28 shows the comparison of variation in phase of interference pattern as a function of time with three different environmental conditions as discussed previously. The comparison of analysis is given in Table. 3.2. All the cases show reasonable long-term stability, but the variation does not seem to correlate with what would be expected from the conditions (i.e. increased air currents), and its clear the different conditions do not have a significant effect.

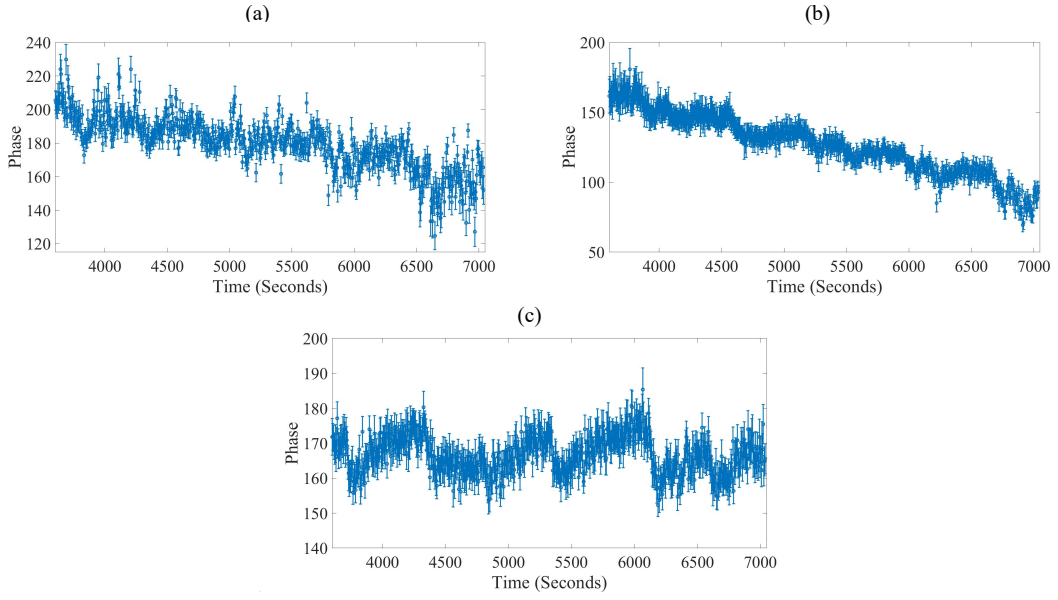

FIGURE 3.28: Comparison of phase stability of interference pattern over 60 minutes with three different ambient conditions (a) Case (1) (b) Case (2) (c) Case (3). The initial phase was omitted to allow the optical components to thermalise.

The interference pattern shows good stability in case (3), which is the typical environmental condition during UV writing experiments. These experiments provide a worse-case estimation of the phase stability in the system due to the extended path of the interferometer. More accurate determination of the phase stability will be derived from further Bragg grating studies which would also include the stage system stability. However, this study shows that the beam and interference drift is not substantial.

3.6 Multi-pass writing approach

Here we investigate a new writing regime where UV radiative fluence is built up over multiple passes, reducing the peak fluence. Figure 3.29 shows the schematic of fabrication using a multi-pass writing approach.

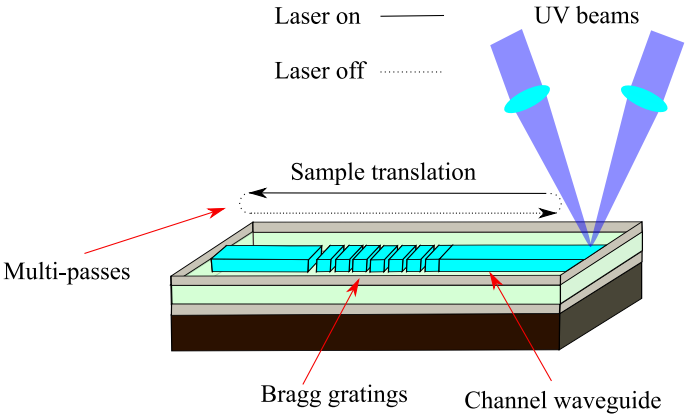

FIGURE 3.29: Schematic of multi-pass writing approach. The solid black line shows sample translation when the laser is 'ON'state, and the dotted line represents when the laser is 'OFF'while the sample returns to its start position very fast. The average power of the laser was fixed at 4 mW.

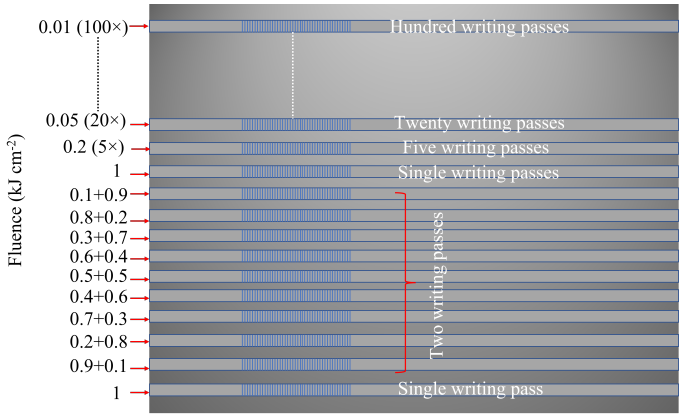

FIGURE 3.30: Schematic of fabricated chip written in various combinations of writing passes at a total fluence of 1 kJ cm^{-2}. The translation speed of Aerotech stages controlled the fluence for each pass.

In this technique, the fluence splits into more than one pass. The fluence for each pass varies via controlling the stage speed. In multi-pass writing, we observe a significant

increase in achieved effective refractive index and grating strength compared to single-pass writing. Multi-pass writing also offers the potential benefit of reducing artefacts associated with hydrogen out-gassing. This approach improves the fabrication efficiency of grating-based devices, which is desirable for integrated optics.

To explore this new writing regime, waveguides were written at a fixed writing power of 2 mW over two passes, changing the combination of writing fluences in a pseudo-random order (i.e., 0.1+0.9, 0.8+0.2, 0.6+0.4 kJ cm^{-2}). Each waveguide contained a 4-mm long uniform grating at a targetted Bragg wavelength of 1560 nm. A waveguide written with a fluence of 1 kJ cm^{-2} in a single pass was inserted at the start and end of writing to rule out spatial dependencies and the effect of hydrogen out-gassing; this also allows a comparison between multi-pass and single-pass writing. Additionally, nine more waveguides were fabricated where the fluence of 1 kJ cm^{-2} was divided between 1 and 100 passes (see Fig. 3.30). Figure 3.31 shows the plot of n_{eff} and Δn_{ac} written as the fluence of the first pass is varied. Here the total fluence of 1 kJ cm^{-2} was used in two passes. With the increasing fluence of the first pass, no substantial change in waveguide and grating properties was observed. However, both n_{eff} and Δn_{ac} follow a peak at a fluence of 0.4 kJ cm^{-2} and reduce at higher fluences of first pass.

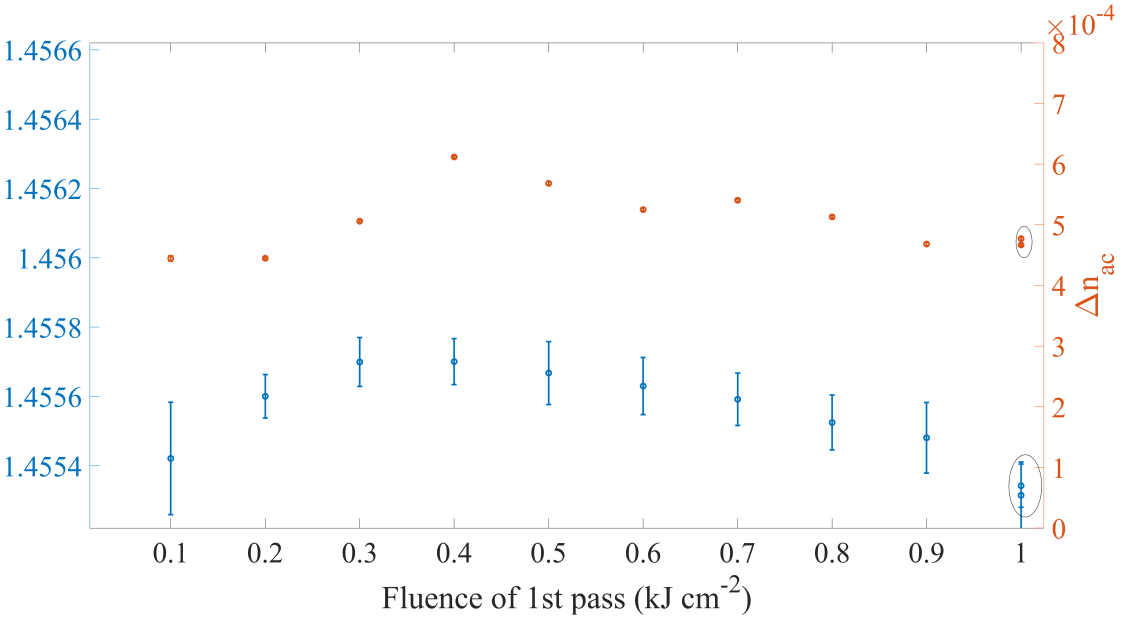

FIGURE 3.31: Variation in n_{eff} of waveguides written at total fluence of 1 kJ cm^{-2} using two passes. Data points in the circle are written at a fluence of 1 kJ cm^{-2} in a single-pass.

The photosensitivity does not change substantially over two writing passes. However, a significant variation in photosensitivity and grating strength was perceived when the writing passes varied from 1 to 100. Figure 3.32 illustrates the reflection spectra of the gratings written in a single pass and over-written in 20 and 40 passes. The figure shows a broadening and a large red shift in the central wavelength of overwritten gratings compared to those written in a single pass. The total time to write the waveguide and gratings in 40 passes was $\sim$ 25 minutes. Figure 3.33 shows the variation in n_{eff} and Δn_{ac} written at a net fluence of 1 kJ cm^{-2} with a different number of passes. Increasing the number of writing passes from 1 to 100, we observe a 1.4×10^{-3} increase in the effective refractive index of the waveguide compared to those written in a single-pass. Similarly, we perceive a significant increase in the strength of the grating by increasing the number

of passes to 40. The achieved Δn_{ac} of gratings overwritten 40 times is 1.6 times higher than those written in a single pass. A further increase in writing passes (beyond 40) reduces grating strength. This abrupt reduction in grating strength is due to the fast translation speed of Aerotech stages.

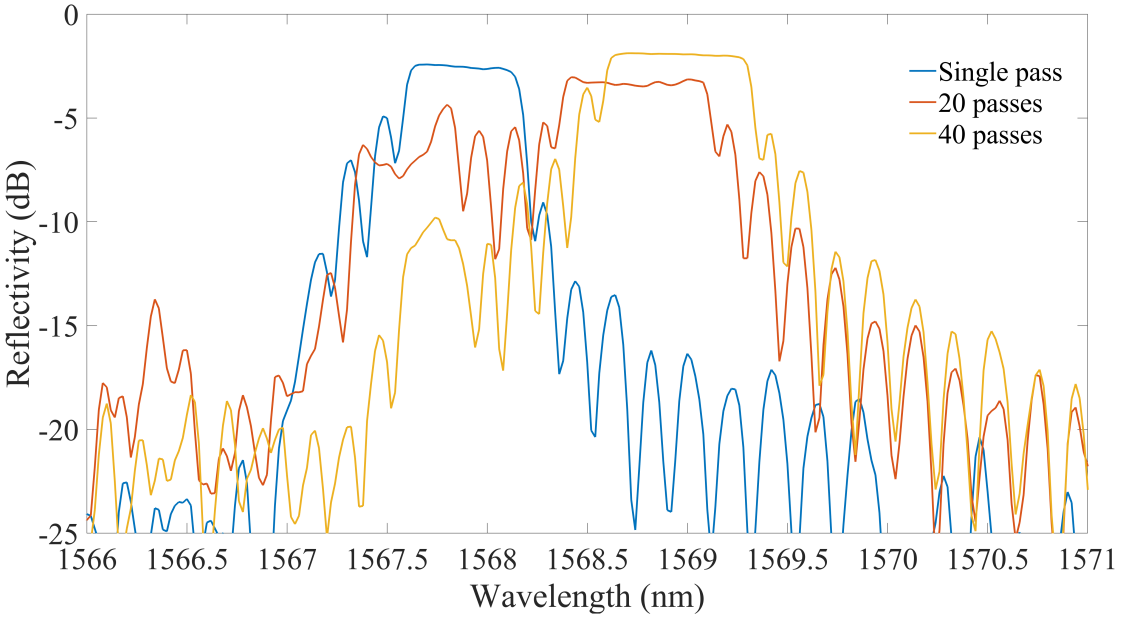

FIGURE 3.32: Grating reflection spectra; In 20, and 40 writing passes gratings are broadened and red shifted.

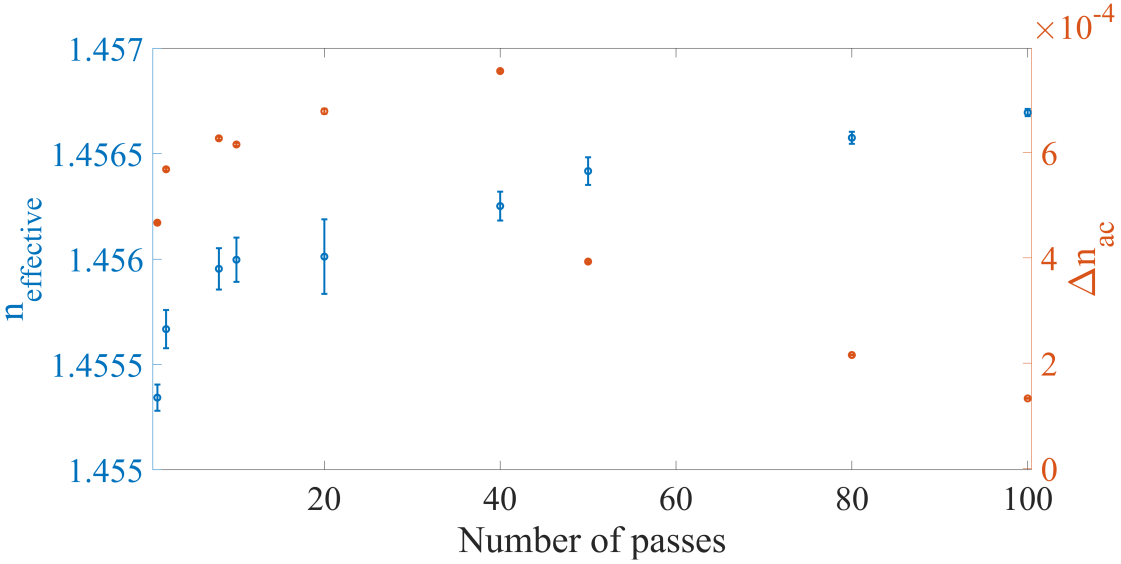

FIGURE 3.33: Variation in n_{eff} of waveguides written at total fluence of 1 kJ cm^{-2} using multi pass ranging from 1 to 100.

In the overwriting approach, writing speed is a crucial parameter in the UV writing system, which plays a vital role in evaluating the gratings strength of devices. To increase the number of writing passes, we must reduce the peak fluence to achieve the overall fluence 'same' for each waveguide. Hence, Aerotech stages run faster for each writing pass. However, there is a range of writing speeds (6 to 60 mm/min) where

the integrator provides a peak operating voltage of 3.6 kV. Increasing the stage speeds (above 60 mm/min), the peak voltage to EOM starts reducing where the scanning speed of interference fringes cannot match the sample translation speed. This results in blurring out the refractive index contrast of the gratings and hence the reduced Δn_{ac} in Fig. 3.33. However, future work will investigate the effect of multi-pass writing at the stage speed above 60 mm/min with a correct voltage offset.

Here, we have investigated a new writing regime where UV laser fluence builds up in multiple passes. Using the overwriting approach, we observed a significant improvement in photosensitivity (increment of 1.4×10^{-3} in effective refractive index) and gratings strength (1.6 times higher) compared to single-pass writing. The improved photosensitivity and gratings strength in the multi-pass writing approach can be attributed to the pre-sensitisation of the hydrogen-loaded sample during the first few writing passes [11]. The results also suggest that overwriting gratings in multiple passes lead to higher grating strength as it minimises the phase errors that may arise due to instabilities associated with the interferometer, stage system, and laser power. It may be possible that writing in a single pass with a higher fluence could result in an increased temperature in the focal volume, which could potentially cause hydrogen to outgas. In contrast, using a single pass with a low fluence locks the hydrogen within the core layer. However, further work is required to investigate the mechanisms of outgassing and hydrogen locking, and we aim to do so in future.

3.7 UV-induced hydrogen locking

In 213 nm UV writing experiments, we observed no significant variation in the waveguide and grating properties of hydrogen-loaded chips over 5-6 hours of fabrication. However, in previous studies that used a 244 nm CW laser, the fabrication time was limited to 2 hours, as exceeding this limit resulted in a significant reduction in photosensitivity due to hydrogen outgassing. To explore the time of hydrogen-out gassing, a simple experiment was conducted. We took a chip from the hydrogen cell and wrote a waveguide and 1 mm long uniform grating. We left the fabricated chip at room temperature for 24 hours. 24 hours later, we wrote another waveguide next to the first with the same laser fluence and writing power. The spacing between the two waveguides was 250 µm. It is worth noting that we were operating at a small UV writing spot with a diameter of 8.2 µm. We did not observe a significant difference in blue fluorescence during the fabrication of the second waveguide next to the first, indicating hydrogen-enhanced photosensitivity still left. Figure 3.34 shows the characterised reflection spectra of 1 mm long uniform grating written after 15 minutes and 24 hours of hydrogen outgassing. The detail of writing parameters and characterised results are given in Table 3.34. Both waveguides showed the same n_{eff} of 1.4482, suggesting the photosensitivity in the localised region was not degraded even after 24 hours of hydrogen out-gassing. The consistent photosensitivity is likely due to the locking of hydrogen within the surrounding core layer due to UV scatter during the fabrication of the first waveguide. Similarly, the (Δn_{ac}) of both 1 mm long uniform gratings is observed 1.1×10^{-3} and 1.3×10^{-3} respectively. The difference in grating strength is likely due to the re-alignment of the laser before each fabrication. The experimental parameters and results of both fabricated waveguides are given in Table 3.3. UV-induced hydrogen locking in planar silica and Ge-doped fibre has previously been seen using a 193 nm excimer laser exposure. [11].

The above experiment shows that 213 nm UV exposure locks the hydrogen-enhanced photosensitivity in the localised region. Using a large UV beam, hydrogen can be locked over a large planar sample area, which will be a matter of interest in future. Additionally, we aim to investigate the spatial and temporal dependency of hydrogen locking in a planar sample.

Waveguide	Hydrogen out-gassing time	Average laser power	Laser fluence	n_{eff}	Δn_{ac}
1	15 minutes	4 mW	1 kJ cm^{-2}	1.44823	1.1×10^{-3}
2	24 hours	4 mW	1 kJ cm^{-2}	1.44821	1.3×10^{-3}

TABLE 3.3: Detail of UV parameters and characterised results of the waveguide and gratings written after 15 minutes and 24 hours of hydrogen out-gassing.

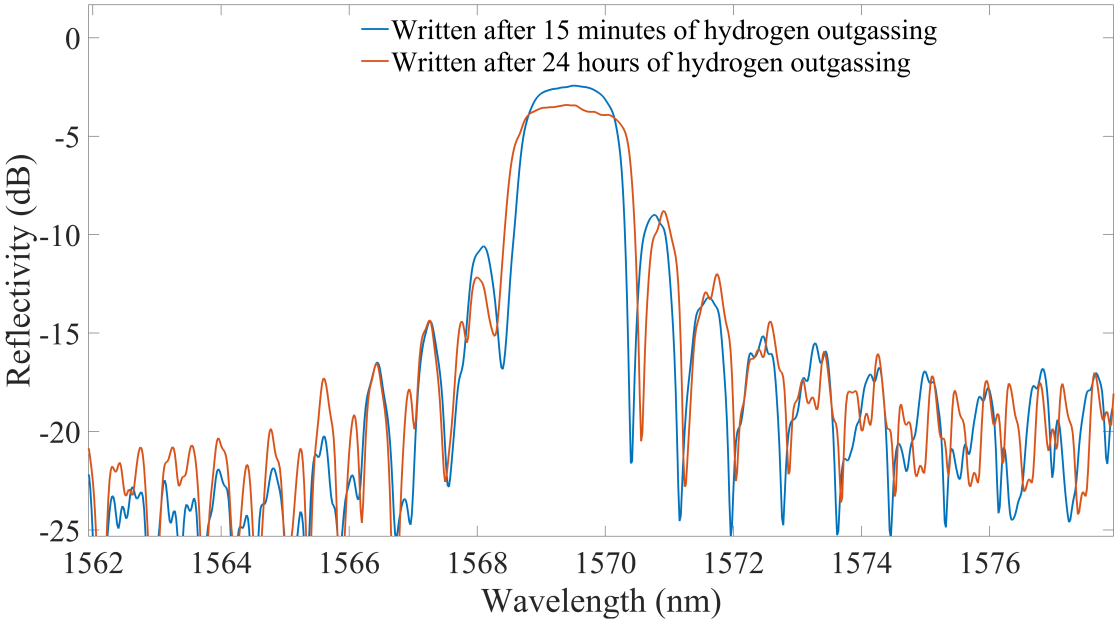

FIGURE 3.34: (a) Gratings reflection spectra with no outgassing (blue) and approximately 24 hours of outgassing (orange).

3.8 Conclusions

This chapter discusses the system calibration of the 213 nm system for defining integrated channel waveguides containing Bragg gratings. The waveguides and gratings are formed in planar silica with and without hydrogen loading. The 213 nm laser writing system operates with similar parameters and resulting device performance compared with conventional 244 nm direct writing systems. However, the system needs a 3.5 kV peak voltage to EOM to obtain the strength of the maximum grating, which is 0.7 kV lower than the required voltage for the grating writing using a CW 244 nm laser. All the gratings parameters were controlled through software without altering the UV interferometer. This chapter also presents and discusses the use of these Bragg gratings to characterise the 213 nm photosensitivity response in this doped silica platform.

Additionally, this chapter contains knowledge about the fluence dependence of the gratings strength, the effective refractive index of the waveguide, the detuning bandwidth of grating fabrication, and the waveguide propagation losses. We developed an intuitive model to understand the relationship between the photosensitivity of the material and the grating's response. We observed that gratings strength starts to deplete with increasing fluence before the photosensitivity saturation. This work did not highlight any nonlinear effects in the duty cycle curve, which have been suggested in the past [7], although a greater range of applied UV power will be required to verify the effects, which will be discussed in Chapter 4.

This chapter also deals with fabricating direct UV-written waveguides and gratings in non-hydrogen-loaded silica samples with 213 nm light. The challenges of avoiding the damage threshold of silica from the pulsed laser system and the stability of the interferometer are addressed. Again, the origin of laser-induced damage will be discussed in chapter 4. The experiments demonstrated the successful fabrication of waveguides and high-quality gratings despite the $\sim$ 17 hours of writing time. However, hydrogen loading provides 1.7 times higher Δn_{ac} than non-hydrogen loaded gratings. We developed an imaging system to investigate the interference pattern's phase variations. However, the measurement method was not robust enough to precisely measure phase errors in the writing systems. In summary, fabricating waveguides in non-hydrogen-loaded samples is not ideal, but it is relatively suitable for grating inscription since waveguides require much higher fluences than gratings.

We identified a new approach to define gratings where UV radiative fluence builds up in multiple passes. Results suggested that the photosensitivity and grating strength can be substantially improved using the multi-pass writing technique. Additionally, these experiments showed consistent photosensitivity of devices suggesting the hydrogen out-gassing effect is not substantial. This writing technique is crucial for the inscription of larger and more complex devices, by providing a robust photosensitive platform via pre-exposure. Additionally, it minimises the artefacts associated with the out-gassing of hydrogen and the stability of the interferometer. Results of overwriting experiments suggest the writing system is stable for grating inscriptions for at least 25 minutes, if not longer.

In a separate experiment, the effect of out-gassing was also probed by writing two waveguides in a single chip with a fabrication time difference of 24 hours. Results showed the possibility of hydrogen locking inside the planar layer during initial 213 nm exposure. Conclusively, the writing time of 213 nm radiated hydrogen-load samples can be prolonged to 24 hours without significant variation in photosensitivity compared to CW 244 nm laser, where writing time is limited to $\sim$ 2 hours. Again, this is important to get consistent fabrication results in hydrogen-loaded samples. Both multi-pass writing and pre-exposure techniques will be used in Chapter 5 for making large-area grating couplers.

A part of this work is published in 'Electronics Letters', [12] and conference proceedings in [13]–[15]. The work presented in [8], [16], [17] is not included in this thesis.

3.9 References

[1] C. Sima, J. C. Gates, H. L. Rogers, P. L. Mennea, C. Holmes, M. N. Zervas, and P. G. R. Smith, "Ultra-wide detuning planar Bragg grating fabrication technique

based on direct UV grating writing with electro-optic phase modulation," *Optics express*, vol. 21, no. 13, pp. 15 747–15 754, 2013.

[2] C. Sima, "Integrated planar Bragg grating devices for advanced optical communication systems," Ph.D. dissertation, University of Southampton, 2013.

[3] P. C. Gow, R. H. S. Bannerman, P. L. Mennea, C. Holmes, J. C. Gates, and P. G. R. Smith, "Direct UV written integrated planar waveguides using a 213 nm laser," *Optics express*, vol. 27, no. 20, pp. 29 133–29 138, 2019.

[4] T. Erdogan, "Fiber grating spectra," *Journal of lightwave Technology*, vol. 15, no. 8, pp. 1277–1294, 1997.

[5] A. S. Othonos and K. Kalli, *Fiber Bragg gratings fundamentals and applications in telecommunications and sensing*. Artech house, 1999.

[6] H. L. Rogers, S. Ambran, C. Holmes, P. G. R. Smith, and J. C. Gates, "In situ loss measurement of direct UV-written waveguides using integrated Bragg gratings," *Opt. Lett.*, vol. 35, no. 17, pp. 2849–2851, 2010.

[7] M. Gagné and R. Kashyap, "New nanosecond Q-switched Nd:VO_4 laser fifth harmonic for fast hydrogen-free fiber Bragg gratings fabrication," *Optics Communications*, vol. 283, no. 24, pp. 5028–5032, 2010.

[8] P. C. Gow, Q. S. Ahmed, P. L. Mennea, R. H. S. Bannerman, A. Jantzen, C. Holmes, J. C. Gates, C. B. Gawith, and P. G. R. Smith, "213 nm laser written waveguides in Ge-doped planar silica without hydrogen loading," *Optics Express*, vol. 28, no. 21, pp. 32 165–32 172, 2020.

[9] C. Holmes, "Direct UV written planar devices for sensing and telecommunication applications," Ph.D. dissertation, University of Southampton, 2009.

[10] J. Sparrow, "Development and applications of UV written waveguides," Ph.D. dissertation, University of Southampton, 2005.

[11] M. Åslund, J. Canning, and G. Yoffe, "Locking in photosensitivity within optical fiber and planar waveguides by ultraviolet preexposure," *Optics Letters*, vol. 24, no. 24, pp. 1826–1828, 1999.

[12] Q. S. Ahmed, P. C. Gow, C. Holmes, P. L. Mennea, J. W. Field, R. H. S. Bannerman, D. H. Smith, C. B. Gawith, P. G. R. Smith, and J. C. Gates, "Direct UV written waveguides and Bragg gratings in doped planar silica using a 213 nm laser," *Electronics Letters*, vol. 57, no. 8, pp. 331–333, 2021.

[13] Q. S. Ahmed, P. C. Gow, P. Mennea, R. Bannerman, D. H. Smith, C. Holmes, J. C. Gates, and P. G. R. Smith, "Direct 213 nm UV written Bragg gratings and waveguides in planar silica without hydrogen loading," in *Integrated Photonics Research, Silicon and Nanophotonics*, Optical Society of America, 2020, IW2A–4.

[14] Q. S. Ahmed, J. W. Field, P. C. Gow, C. Holmes, R. H. S. Bannerman, P. L. Mennea, C. B. E. Gawith, P. G. R. Smith, and J. C. Gates, "Investigation into multi-pass exposure of 213 nm pulsed uv writing for improved writing response," in *Integrated Photonics Research, Silicon and Nanophotonics*, Optica Publishing Group, 2022, JTu2A–33.

[15] Q. S. Ahmed, J. W. Field, P. C. Gow, C. Holmes, R. H. S. Bannerman, P. L. Mennea, C. B. E. Gawith, P. G. R. Smith, and J. C. Gates, "Improved photosensitive response of doped silica to a 213 nm pulsed laser using a multi-pass writing approach," CLEO/Europe-EQEC, 2023.

[16] P. C. Gow, C. Holmes, Q. S. Ahmed, and P. G. R. Smith, "Microwave consolidation of photosensitive planar glass layers," in *Integrated Photonics Research, Silicon and Nanophotonics*, Optica Publishing Group, 2020, IW2A–3.

[17] P. C. Gow, Q. S. Ahmed, J. C. Gates, P. G. R. Smith, and C. Holmes, "Microwave consolidation of UV photosensitive doped silica for integrated photonics," *Optical Materials Express*, vol. 11, no. 6, pp. 1835–1841, 2021.

Chapter 4

Investigation into the writing dynamics of planar Bragg gratings using a pulsed 213 nm radiation

4.1 Introduction

Chapter 3 comprehensively discussed the characterisation of waveguides and gratings written using a 213 nm laser. However, this work did not observe any sign of non-linearity associated to 213 nm laser. The non-linear photosensitivity response to 213 nm light was previously reported by Gagné and Kashyap in hydrogen-free B/Ge doped fibre [1]. In their work, two-photon absorption was suggested to be a dominant mechanism for the photosensitivity of B/Ge doped fibre.

Inspired by the work in [1], we fabricated devices in planar silica with different laser writing powers to observe the effects on the resulting channel waveguides and gratings. However, the fabrication of gratings in planar silica inherently differs from fibre due to the geometry, glass composition, and stresses between the layers and the silicon substrate. The typical structure we use for planar optics consists of a flame hydrolysis deposited silica core layer, doped with germanium and boron, on a silicon wafer with a 15 μm thermal oxide. A thick overclad layer doped with phosphorus and boron is usually deposited on top of the core layer. The planar core layer does not contain any pre-defined waveguide structures; therefore, these must be defined during the UV writing process. Using high-energy pulsed sources to define waveguides and gratings can lead to significant levels of ablation and subsurface damage to samples [2]. Therefore, it is essential to establish the optimal regimes to use these laser sources without causing damage. In chapter 3, SSDUW with constant writing power found a linear photosensitivity response to a fluence followed by saturation [2], similar to that observed for conventional 244 nm CW writing. In this work, we use a broad range of average beam powers and fluences to explore the characteristics of SSDUW, investigating the saturation of the photosensitivity response and grating properties to find the optimal writing regimes for 213 nm laser light in a planar silica platform. This study is critical for the UV writing of

waveguides and Bragg gratings in planar silica and fabrication of gratings in pre-defined waveguides and local phase trimming [3].

This chapter discusses the non-trivial response of gratings and waveguide properties. We extensively investigate n_{eff} , modulated refractive index of the gratings, birefringence and the laser-damage at a broad range of writing powers and fluences. Rod Cecil and James Gates fabricated the FHD layers discussed in this chapter. For estimating the grating's strength, modelling was performed with the help of Rex Bannermann and James Field. Waveguide and gratings fabrication, characterisation and data analysis were solely my work.

4.2 Experimental scheme

In this work, three-layer silica-on-silicon was used as the photosensitive platform. Flame Hydrolysis Deposition (FHD) was employed to deposit a 4.5 µm thick core layer of germanium and boron-doped silica onto a silicon wafer with a 15 µm thermal oxide acting as an underclad. The peak germanium and boron concentrations are estimated from time-of-flight mass spectroscopy to be $\sim 1\%$ and $\sim 10\%$, respectively. This core layer was capped with an index-matched 16.2 µm thick boron and phosphorous-doped upper-clad layer, also produced by FHD. The wafer identifier number of the used deposition recipe was PX 57 (see Appendix 1 for complete deposition details). Figure 4.1(a) shows a longitudinal cross-section of the typical structure of the FHD-deposited silica on silicon, including the alignment of the UV writing beams. It shows the dual-beam interferometry (as discussed in Chapter 3) using the 213 nm laser to simultaneously fabricate waveguide and Bragg gratings in the photosensitive B/Ge doped core layer. Figure 4.1(b) shows the transverse cross-sectional view of the waveguide. It shows the laser beam is focused with a $1/e^2$ spot diameter of 7.6 µm, inducing a change in effective refractive index forming the channel waveguide. Figure 4.1(c) shows the mode field diameters of UV-induced waveguides in both the x and y-direction, measured using a waveguide characterisation setup developed by Rex Bannerman [4]. Waveguides and gratings were simultaneously fabricated as shown in Fig. 4.2. The used samples were hydrogen loaded. For this experiment, the repetition rate of the laser was fixed at 10 kHz to generate a maximum average power of 14 mW (at the surface of the chip). The chip contained nine waveguides over which the writing power of the laser was increased from 0.5 mW to 14 mW (at the surface of chip). We have used a broad range of peak laser intensities ranging from 0.02 to 0.75 GW cm^{-2}. Increasing the laser power while maintaining constant fluence increases the translation speed of the stage system; the sample is exposed to higher pulse energies but a smaller number of pulses. Each waveguide contained ten 1-mm long uniform gratings; the Bragg wavelengths of these gratings were targeted from 1520 nm to 1587.5 nm with a wavelength interval of 7.5 nm (as shown in Fig. 4.3(a). The writing fluence for these gratings was pseudo-randomly ordered from 0.18 kJ cm^{-2} to 1.82 kJ cm^{-2} to limit the error from any spatial dependencies over the chip's length. The fluence was controlled by the translation speed of the air-bearing stage system (Aerotech). To maximise the grating reflectively, a peak voltage of 3.6 kV was applied to the EOM with an 80% duty cycle.

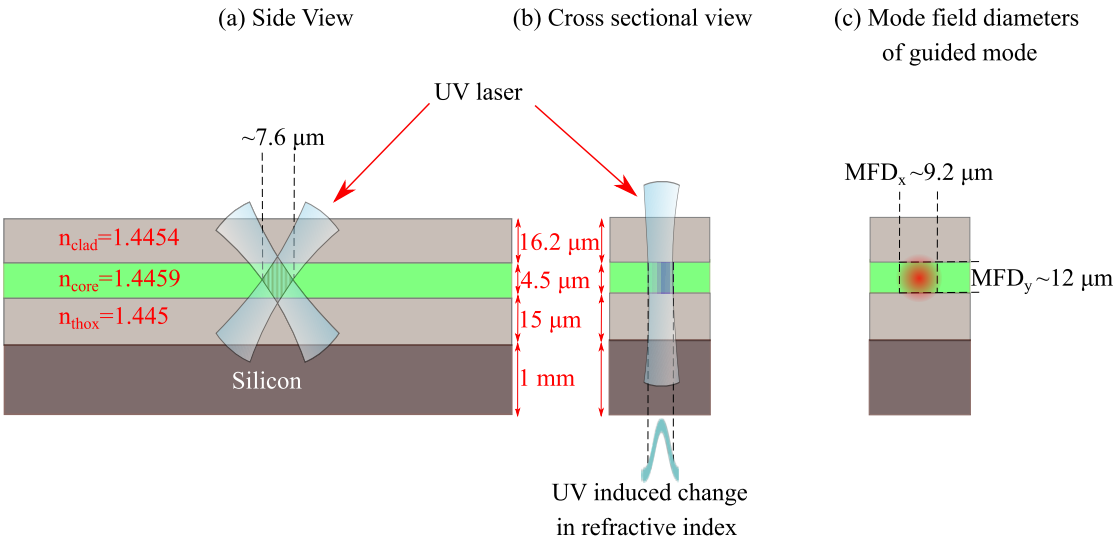

FIGURE 4.1: (a) Schematic of small spot direct UV (SSDUW) writing in a three-layer silica-on-silicon platform. (b) Schematic of a cross-sectional view of the FHD sample shows a UV laser beam inducing a change in the refractive index of the photosensitive core layer. (c) The mode field diameters (MFD) of UV-written waveguides are shown in the x and y-direction. All values are for 1550 nm operation.

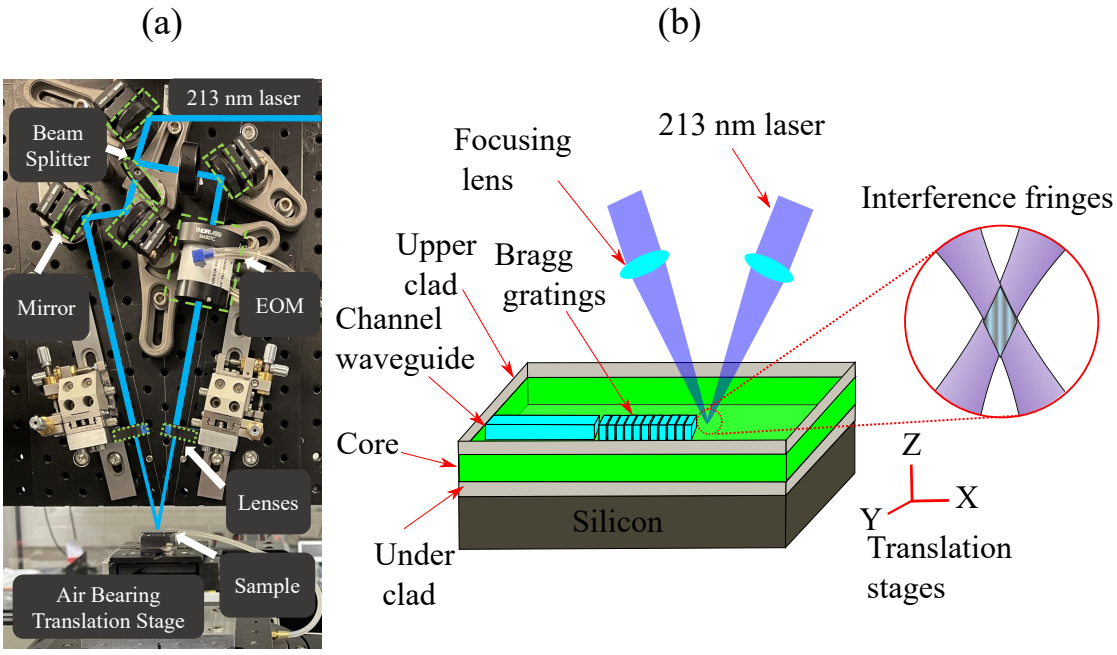

FIGURE 4.2: (a) An annotated photograph of 213 nm SSDUW setup. (b) Schematic of UV writing setup; enabling inscription of waveguides and Bragg gratings simultaneously in doped silica.

4.3 Characterisation results

For the grating characterisation, an Er-doped fibre amplified spontaneous emission (ASE) source was used with a polariser and polarisation maintaining fibre as described in [5]. A 3 dB fused fibre coupler was used to collect the reflected light, and the grating

spectra were measured on an optical spectrum analyser. We characterise the grating properties only in TE polarisation. Figure 4.3(b) shows a photograph of the UV fabricated chip; the white light illumination source shows the colourful diffraction of the Bragg gratings. The waveguides written with higher laser power showed signs of laser-induced damage.

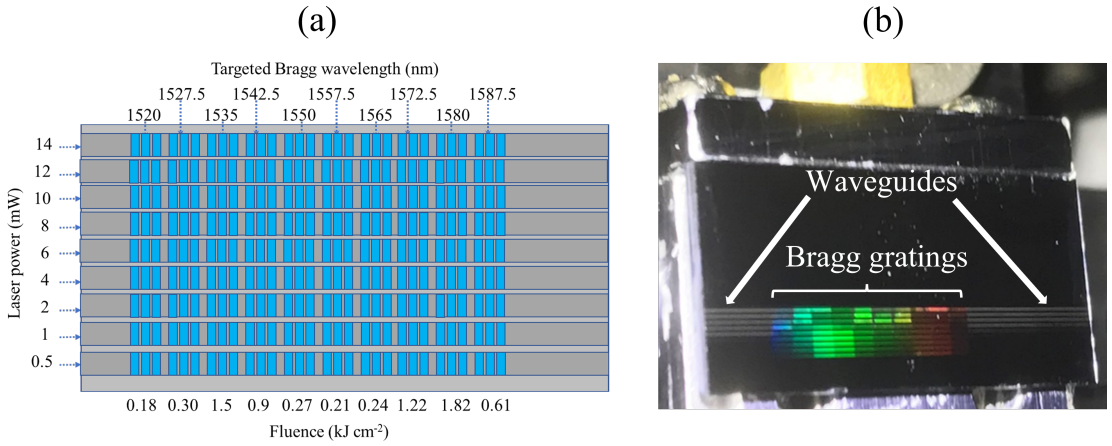

FIGURE 4.3: (a) Schematic of the planar silica chip used to investigate the effect of laser power and writing speed (fluence) on grating properties. (b) Photograph of UV written chip mounted on characterisation apparatus. Each waveguide contained ten 1-mm long uniform gratings written at different fluences ranging from 0.18 cm^{-2} to 1.82 kJ cm^{-2} in random order. A white light source highlights the colourful diffraction of the Bragg gratings. The waveguides written with high power (6 to 14 mW) show signs of laser-induced damage.

4.3.1 Grating response

Figure 4.4 displays the reflection spectra of gratings inscribed at different fluences with a writing beam power of 1 mW. The reflectivity of these gratings was normalised by referencing to the 3.3% reflection of the ASE source from the pigtail facet. At higher fluences of 1.5 kJ cm^{-2} and 0.9 kJ cm^{-2} respectively, the third and fourth gratings in the waveguide begin to saturate, which is evidenced by the 'flat top' in the grating spectra. This saturation offers an alternative route for estimating power in the waveguide. However, it is difficult to estimate Δn_{ac} accurately as gratings strength is influenced by fluence, and detuning. However, accurately estimating the Δn_{ac} is difficult due to grating detuning and absence of 100% reflector at the start of the waveguide. Later in this chapter, we will demonstrate a robust method for measuring the grating strength.

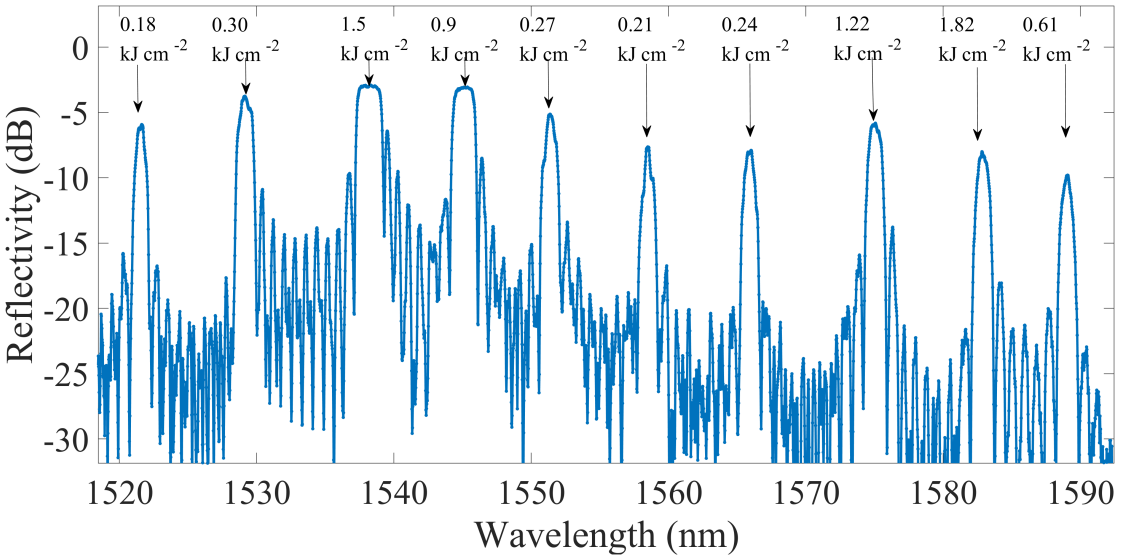

FIGURE 4.4: Reflection spectra from a single waveguide written at 1 mW laser power, containing ten 1-mm long uniform gratings with central Bragg wavelength from 1520 nm to 1587.5 nm. The gratings were written at different fluences ranging from 0.18 kJ cm^{-2} to 1.82 kJ cm^{-2}.

Figure 4.5 (a) shows reflection spectra of gratings written at the fluence of 0.3, 0.9 and 1.5 kJ cm^{-2}, varying writing power from 0.5 to 14 mW. At the fluence of 0.3 kJ cm^{-2}, a red shift in the central wavelength and a gradual broadening in the peak is evident with increasing power. Increasing the writing power from 0.5 to 4 mW, we observe a positive change in effective refractive index with increased grating strength. However, ramping up the power to 6 mW and above, leads to a transition of photo-induced effects where the central peak becomes anomalously broad. At the fluence of 0.9 and 1.5 kJ cm^{-2} a similar trend in the reflectivity is observed up to 4 mW power of writing power. However, above 4 mW, the amplitude of the peak reflectivity starts decreasing and nearly disappears at 14 mW of writing power. There are clear signs of laser-induced damage on the waveguides and gratings written at higher writing power (above 4 mW). The non-trivial response from the gratings written at higher power (above 4 mW) can be associated to laser-induced damage which leads to additional losses and anomalous broadening in the central peak of reflection spectra. Therefore, it is difficult to trust the measurements of these damaged gratings and corresponding spectra are represented by a grey colour in Figure 4.5 (b).

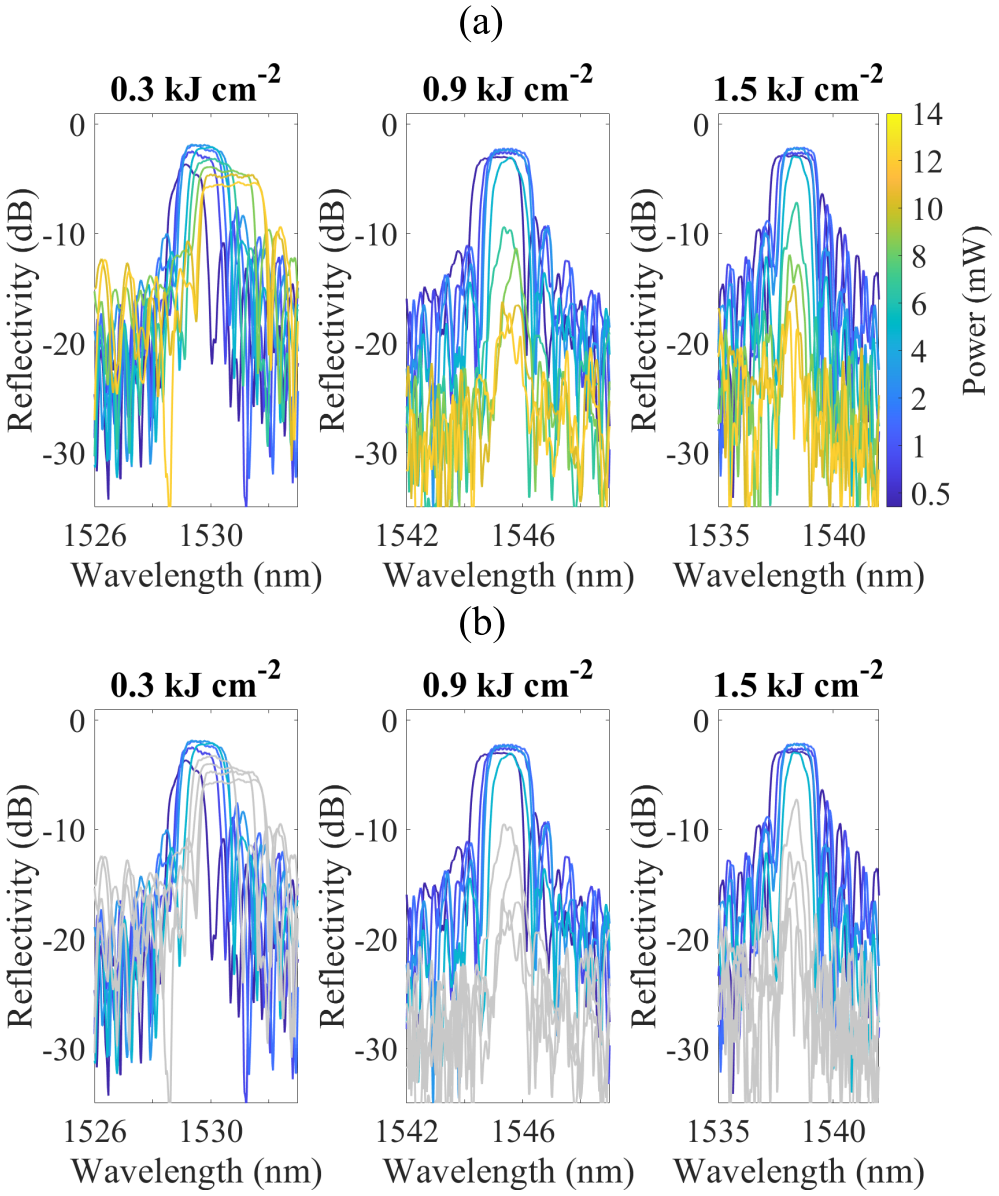

FIGURE 4.5: (a) Reflection spectra of the gratings written with a targeted Bragg wavelength of 1527.5, 1542.5 and 1537 nm corresponding to the laser fluence of 0.3, 0.9 and 1.5 kJ cm^{-2} respectively, at laser powers ranging from 0.5 mW to 14 mW. (b) Representation of the same data as shown in (a). However, the grey colour represents the damaged gratings written above 4 mW of writing power.

4.3.2 Photosensitivity response

The effective refractive index (n_{eff}) is calculated from the central Bragg wavelength using the Bragg condition for the inscribed grating period. Furthermore, Sellmeier equations for FHD doped silica were used to compensate for the dispersion effect [6].

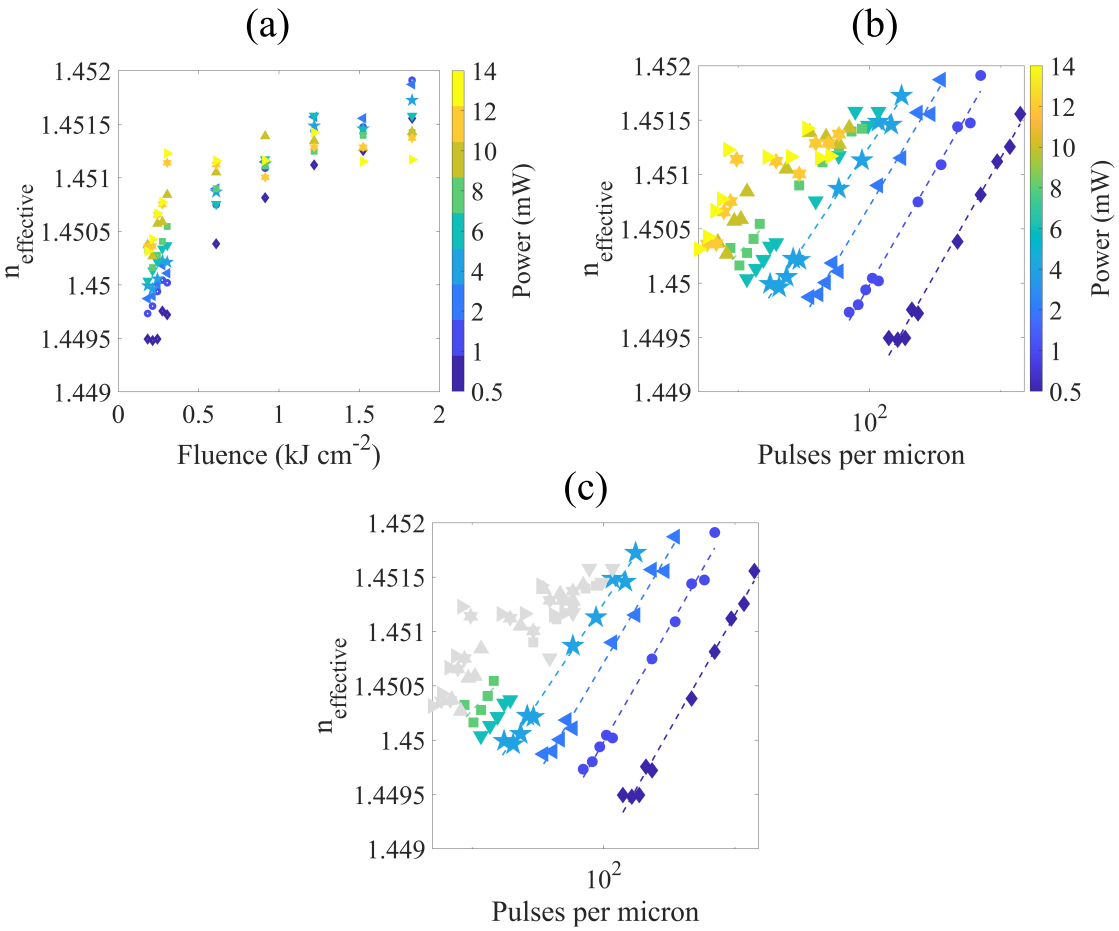

FIGURE 4.6: (a) The plot of change in effective refractive index (n_{eff}) as a function of the average power of the laser. (b) Plot of (n_{eff}) against pulses per micron in a linear-log scale for a better representation of photosensitivity response at different writing powers. (c) The data shown in (b) is plotted again. However, the data points represented by the grey colour are doubtful and correspond to anomalous reflection spectra shown in Fig. 4.5

Figure 4.6(a) shows n_{eff} for each grating as a function of laser fluence at different writing powers. At lower writing powers of 0.5, 1, 2 and 4 mW, the photosensitivity response shows a similar trend (as observed in [2]), where a positive increase in the refractive index is observed, followed by saturation at higher fluences. With continuous exposure, colour centres start to saturate and lead to a saturation of the photosensitivity response. At saturation, a further increase in UV exposure does not induce an increment in the effective refractive index. With increased writing power to 6 mW and above, the laser-induced damage begins to evolve, leading to more complex mechanisms to determine the change in the effective refractive index.

To better represent the photosensitivity dependence on writing power and fluence, we plot n_{eff} against the number of laser pulses per micron on a linear log scale in 4.6 (b). The number of laser pulses is directly proportional to the fluence, with a multiplying factor dependent on writing power. As discussed previously, it is difficult to trust the measurements of damaged gratings due to artefacts in the central peak of reflection spectra. Therefore, the calculated n_{eff} of these gratings is represented by a grey colour in Figure 4.6 (c). At lower powers ranging from 0.5 to 4 mW, n_{eff} increases logarithmically

and follows a linear trend line on a linear-log scale and the gradients of these curves are comparable within error. The photosensitivity response in this regime (0.5 to 4 mW average power) is identical and can be explained typically based on photo-chemical changes in colour centres due to laser exposure. At higher laser powers (above 4 mW), we can only trust the gratings measurements for the lower fluences where we do not see the damage. However, the shapes of the photosensitivity response suggest more than one physical process determines the net change in the refractive index. As we increase the writing power, it might be possible that an adverse process erases the positive change in the refractive index leading to an early saturation of photosensitivity. For instance, Canning et al. [7], [8] indicated the stress relief effect (expansion of glass matrix) correlated to a negative change in the refractive index with a 193 nm UV exposure to the planar germanosilicate waveguides. However, the negative change in refractive index is not evident in our case and it might be possible that the negative index always remains lower than the positive but results in an early saturation of photosensitivity curves.

This experiment does not give a quantitative dependence of gratings strength on the fluence and the writing power of 213 nm laser. This is due to the grating detuning and the absence of a 100% uniform reflector in the waveguide to estimate the coupling loss. However, we observe a subtle non-linearity where gratings and waveguide properties depend on writing power. The damage effect at higher writing power raises several research questions. Is the top planar surface damaged, and are the gratings formed by surface relief? What is the primary origin of damage? All these questions will be addressed in the following sections.

4.3.3 Damage characterisation

4.3.3.1 Investigation of surface relief gratings

The reflection spectra of damaged gratings (shown in Fig. 4.5) were either anomalously broad or highly lossy. We initially thought that the top surface (overclad) was damaged due to high-power UV exposure and surface relief gratings resulting in lossy spectra. We put index-matched oil on the surface to overcome the possibility of surface corrugation and observed the reflection spectra. The resultant plots shown in Figure 4.7 show no variation in the reflection spectra on covering the sample's top surface with index-matched oil. In Figure 4.8, a photograph of white light diffraction from the fabricated chip was taken before (a) and after (b) covering the sample's top surface with index-matched oil. Both images depict damaged waveguides that appear slightly different due to differences in colour saturation and reveal the angular variation of the camera during photography. However, we did not observe a noticeable variation in the colour diffraction pattern under white light illumination, indicating the damage is not on the top surface.

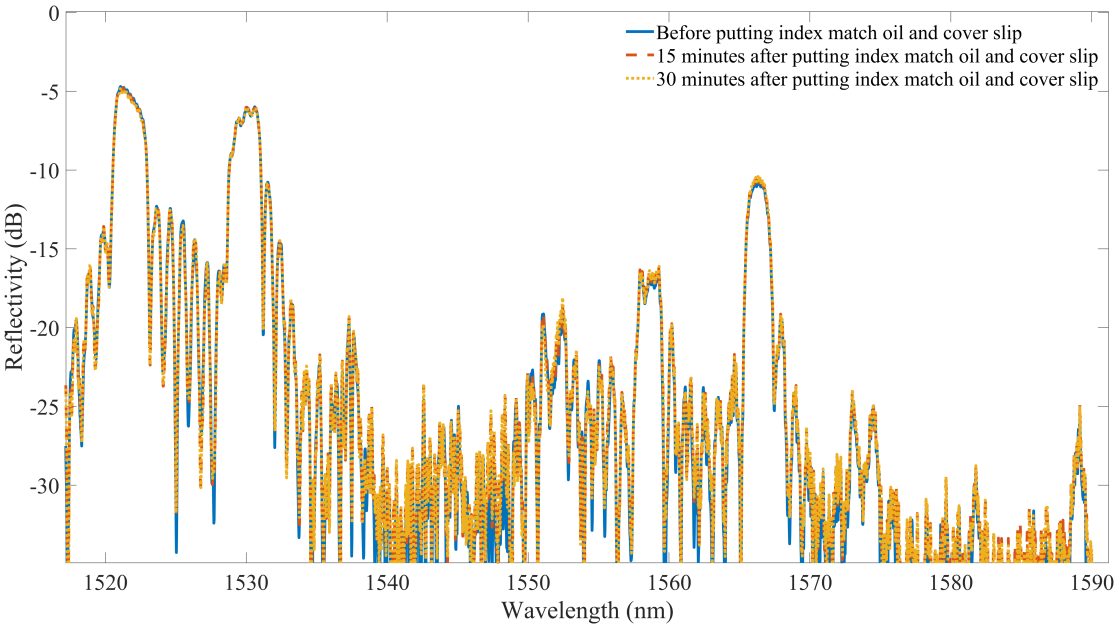

FIGURE 4.7: Reflection spectra of gratings written at the writing power of 14 mW; all the gratings were damaged. The characterisation was performed to probe the surface relief gratings by taking reflection spectra before and after covering the top surface of the chip with an index-matched oil. The data does not show any significant variation in the characteristic of the grating profile.

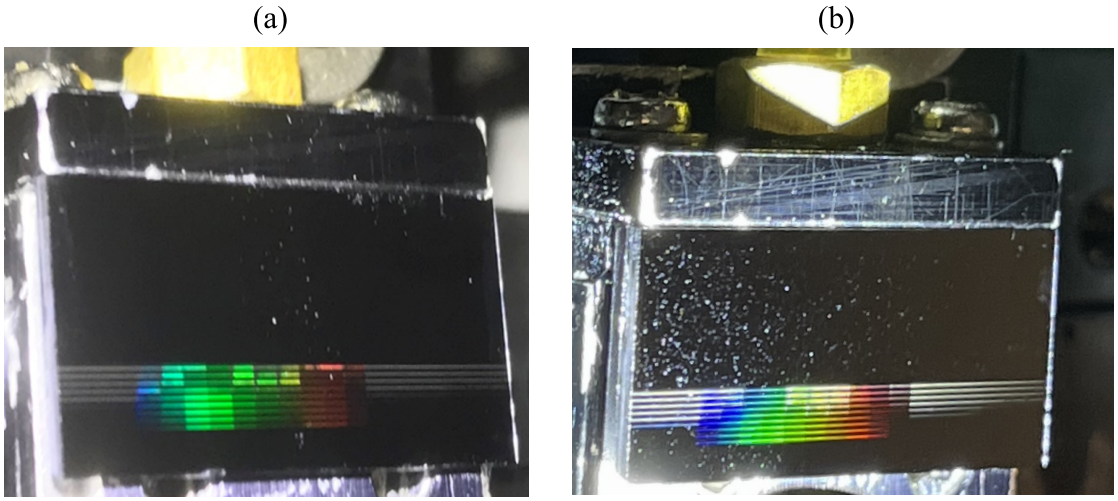

FIGURE 4.8: Photograph of UV written chip mounted on characterisation apparatus in (a). While (b) shows the same chip; however, the top surface is covered with an index-match oil. A white light source highlights the diffraction of the Bragg gratings and does not show any obvious difference between (a) and (b).

4.3.3.2 Microscopy

Light microscopy was performed to investigate the origin of laser-induced damage. Figure 4.9(a) clearly demonstrates a transition from non-damaged to a damaged waveguide with increasing writing power; higher peak intensities lead to damage formation. However, it is challenging to indicate the damage threshold as the damage mechanism is

highly sensitive to the overlap of UV in gratings and waveguide fabrication. To assist microscopy analysis, the chip was diced, and the end facet was polished at an angle of 10° with respect to the parallel plane of the surface (shown in Figure 4.9 (b)) to increase the apparent depth resolution of different layers of silica and silicon. Figure 4.9 (c) shows an optical micrograph of the chip, which contains a waveguide and gratings written at 14 mW, taken from the angle polished end facet.

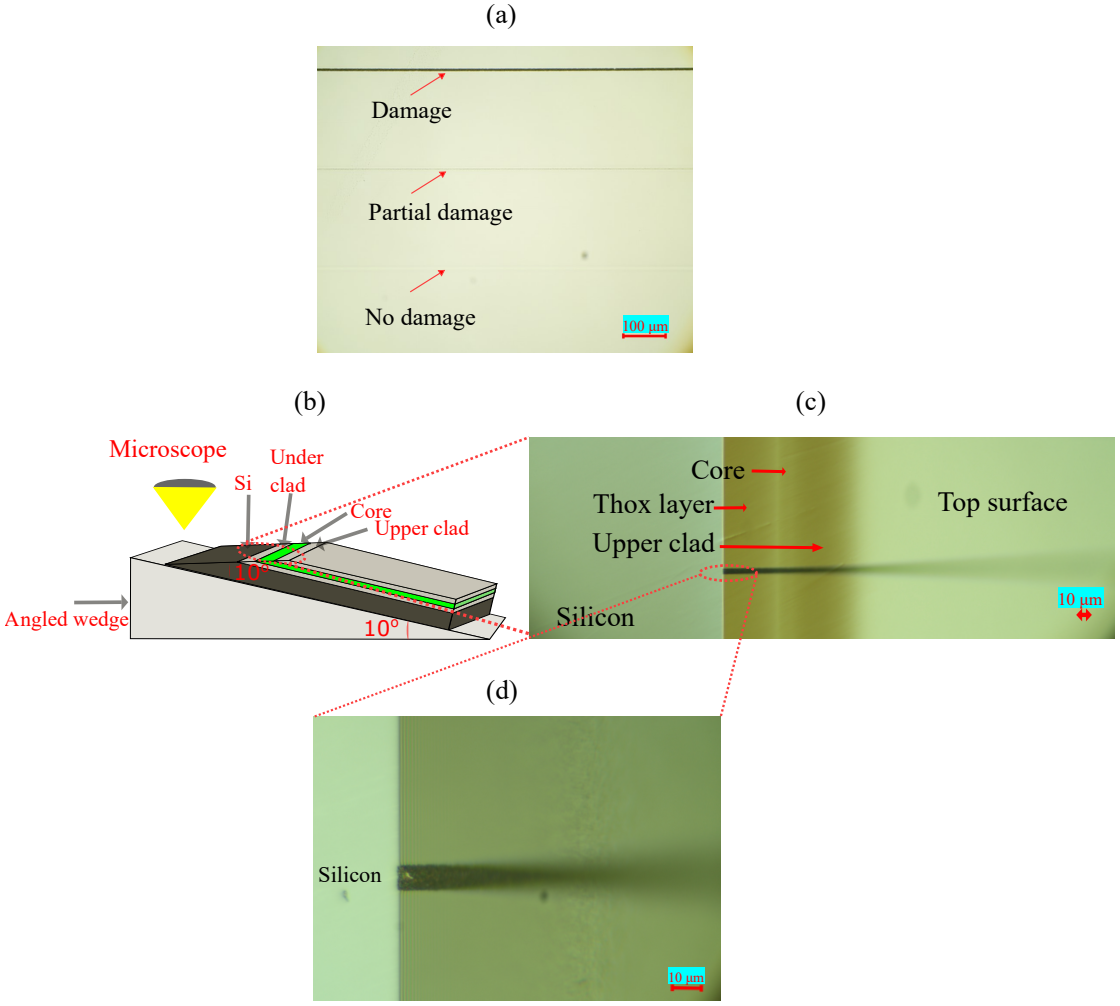

FIGURE 4.9: (a) Demonstration of evolving damage on a UV written waveguide with increasing writing power. (b) Schematic of angle polished end facet of a UV written sample to reveal different layers of silica, and silica-silicon interface under light microscopy. The angled polish effectively increases the resolution of the layers in the depth direction, compared to normal incidence end-facet microscopy. (c) The optical micrograph shows an angled polished end facet of the waveguide written at the writing beam power of 14 mW. (d) A high-magnification image of a waveguide written at 14 mW of laser power shows ablation on the silica-silicon interface.

Figure 4.9 (d) shows a high-magnification image of the same waveguide at the silicon interface. The damage is visible through the layers of glass and is clearly located on the silica-silicon interface. We have not seen any evidence of apparent damage occurring in the silica itself. Pulsed laser-induced damage at wavelengths of 1064, 532 and 355 nm to silicon under a dielectric layer has been previously observed [9] when the photon energy is higher than the bandgap of the silicon and lower than the bandgap of the dielectric. In

these studies, the silicon ablates in a localised region and introduces mechanical stresses between the layers. We suggest that damage at higher peak power densities is due to the ablation of the silicon layer at the silica-silicon interface.

Dr Paul Gow conducted zescope coherent scanning interferometry of damaged waveguides. Similar to optical microscopy, zescope investigations also confirm the origin of damage on the silicon interface.

4.3.4 Raman spectroscopy

Microscopic analysis revealed that high-power UV exposure caused damage to the silicon. Initially, we considered the possibility of structural changes in the silicon from a crystalline to an amorphous phase. To investigate the structural modification of silicon, Dr James Gates conducted Raman spectroscopy on an angle-polished chip, taking several scans from flat glass, polished glass, and silicon. Figure 4.11 shows the resulting intensity plot against the wave number. The data indicates a peak intensity at 521 cm^{-1} [10], corresponding to the crystalline phase of silicon. In the case of an amorphous phase, we would expect a phase shift at 480 cm^{-1} [10]. However, this data only shows the crystalline phase, ruling out the possibility of significant structural deformation.

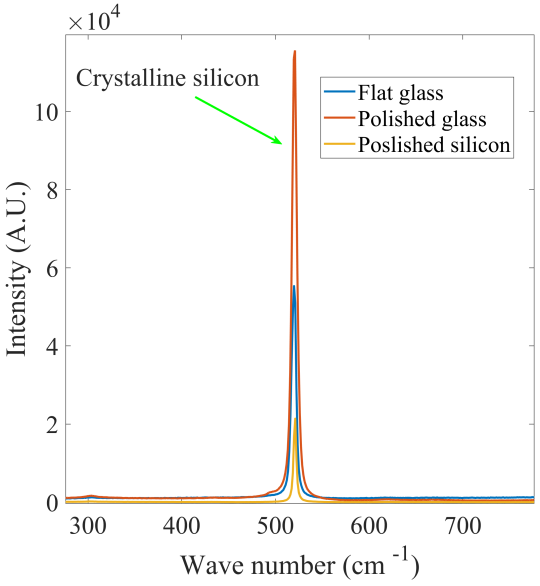

FIGURE 4.10: Raman spectroscopic data of damaged waveguide taken from the flat glass surface, polished glass, and the polished silicon interface.

We have investigated the photosensitivity and gratings response at different writing powers and fluences. The writing powers ranging from 0.5 to 4 mW appear suitable for planar Bragg grating writing, where the photosensitivity of doped silica is attributed to photo-induced colour changes. The use of high power (above 4 mW) leads to localised damage to the silica-silicon interface. Trusting the measurements of damaged gratings is difficult due to the non-typical profile of reflected mode and perceived losses. Additionally, we controlled the writing power by changing the attenuation value from the software control of the 213 nm laser, which may lead to power instability and non-trivial artefacts in writing dynamics. This experiment does not give a quantitative analysis of

grating strength. However, it gives useful information about suitable writing regimes using a pulsed 213 nm laser light without inducing damage. An in-depth analysis of grating strength, effects associated with hydrogen outgassing and photosensitivity will be addressed in the later sections of this chapter.

4.4 Modified experimental scheme

In this experiment, the writing scheme (discussed in section 4.2) was modified to estimate grating's strength at different writing powers and fluences. To probe the effect of laser power and fluence on grating properties, a chip of 20×10 mm was selected and UV written with a series of integrated waveguides and gratings. Each waveguide was 8.1-mm long and contained one 4 mm long uniform grating at a targeted Bragg wavelength of 1540 nm followed by a 1.5 mm long grating at a Bragg wavelength of 1560 nm.

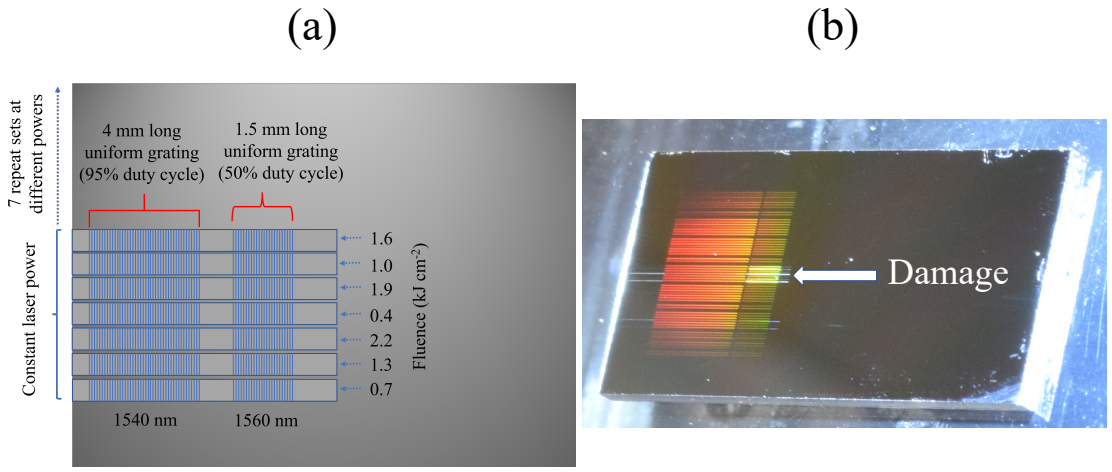

FIGURE 4.11: (a) Schematic of the planar silica chip used to investigate the effect of laser power and writing speed (fluence) on grating properties. (b) Photograph of UV written chip mounted on characterisation apparatus. A white light source highlights the diffraction of the Bragg gratings. The waveguides written with higher laser power (7.3 and 11.6 mW) show signs of laser-induced damage.

In each waveguide, the 1540 nm grating estimated the insertion loss during characterisation and was fabricated with a 95% EOM duty cycle to make the grating highly saturated. The second grating was shorter (1.5 mm) and fabricated with a lower duty cycle (50%) to make strong but not highly saturated gratings as they provide a poor regime for interrogating the grating properties. A set of seven waveguides was fabricated at fluences ranging from 0.4 to 2.2 kJ cm^{-2} in a pseudo-random order for a fixed writing power. The translation speed of the air-bearing stage system controlled the fluence. The chip contained seven similar sets of waveguides fabricated at writing powers ranging from 0.6 to 11.6 mW corresponding to peak laser intensities of 0.02 to 0.58 GW cm^{-2}, as shown in Figure 4.11(a). The writing power of the beam was controlled using ND filters. Increasing the laser power while maintaining constant fluence increases the translation speed of the stage system; the sample is exposed to higher pulse energies but a smaller number of pulses. The grating characterisation was performed in TE and TM using a polarised Er-doped fibre amplifier ASE source [5]. A 3 dB fused fibre coupler was used to collect the reflected light, and the grating spectra were measured on an optical spectrum

analyser. Figure 4.11(b) shows a photograph of the UV fabricated chip; the white light illumination shows the colourful diffraction of the Bragg gratings. The waveguides written with higher laser power of 7.3 and 11.6 mW showed signs of laser-induced damage. The origin of this damage formation is already discussed in section 4.3.3.

Additionally, the chip contained eight other test waveguides to monitor the alignment and effects of hydrogen out-gassing. We observed no obvious variation in the properties of the device due to out-gassing or alignment. The dependence of grating characteristics (bandwidth, reflection, etc.) on laser writing power and fluence are non-trivial, so we explore them independently. Firstly, we investigate the effect of varying fluence at constant power; later we discuss the effect of varying writing power at a constant fluence.

4.5 Grating characterisation

The grating characterisation was performed by coupling input light from a PM optical fibre V-groove assembly to the UV-written channel waveguide. Refractive index-matching oil was used at the interface to prevent facet reflections. Each waveguide was 8.1-mm long and contained one 4 mm long uniform grating at a targeted Bragg wavelength of 1540 nm, followed by a 1.5 mm long grating at a Bragg wavelength of 1560 nm. In each waveguide, the 4 mm long grating served to estimate the coupling loss during characterisation. These were 'flat-toped' 100% reflectors, providing a reference for the power at that position in the waveguide. Figure 4.12 displays the reflection spectra of the gratings from one of the alignment waveguides written at a fluence of 1 kJ cm^{-2} and a writing power of 3.6 mW.

The reflectivity of these gratings was normalised by reference to the 3.3% reflection of the ASE source from the pigtail facet. The Bragg gratings written at lower fluences were not saturated. We used a spectral model for a rigorous analysis of the grating's strength to extract a value of the power within the waveguide. The grating model used is similar to that proposed by Wang et al. [11], a variant of Rouard's method [12]. This approach treats the grating as a thin film stack, with each half period represented by a layer of higher or lower refractive index. The reflections between layers and the phase shifts from layers are easily calculated and used to construct a series of transfer matrices whose product is the transfer matrix of the grating. For a step refractive profile index grating, this provides a complete model for any grating regardless of its apodisation profile or phase. As stated by Wang [2], the sinusoidal refractive index profile of FBGs can be approximated by scaling Δn by $\pi/2$. This approximation is correct for the fundamental response of a weak (Δn<0.01) grating. A similar approach by Miguel et al. [13] further divides each period into more layers producing a more exact model at the cost of linearly increasing computation time.

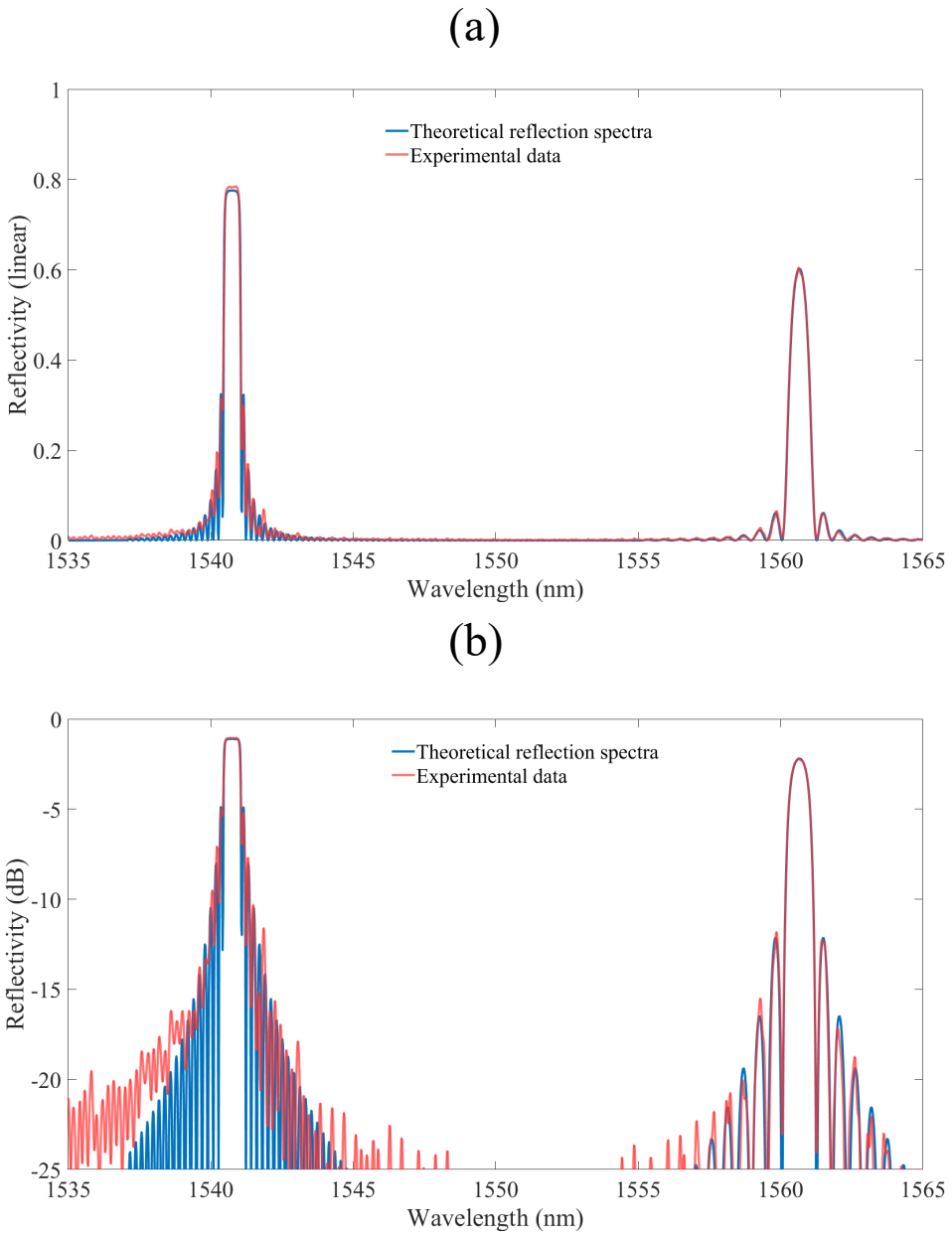

FIGURE 4.12: Experimentally measured spectra of 4 mm and 1.5 mm long uniform gratings, fabricated at 3.6 mW writing power and the fluence of 1 kJ cm^{-2}, are plotted in linear scale in (a) and dB in (b). These plots show experimental data in red, and the theoretical reflection spectra of an ideal uniform Bragg reflectors are plotted in blue.

Our model uses a python optimiser to fit the experimental reflection spectra and returns the fit parameters, including effective refractive index, modulated refractive index and the coupling loss. The same model is used to calculate the theoretical reflection spectrum in Figure 4.12. Using the reflection from the polished fibre pigtail and this model, we can estimate the reflectivity and determine the optical power coupled into the waveguide. To validate the approach, we have previously compared the derived power with the measured transmission (insertion) loss and this has shown good agreement. The derived coupling loss was between 0.4 dB and 1 dB, with a typical loss of 0.6 dB to a standard optical fiber. This is mainly due to poor end facet preparation as we would expect only $\sim$ 0.1 dB loss due to mode mismatch. This technique works well in this scenario, where

the gratings do not induce additional loss via scattering, as may be seen with other integrated platforms.

This model does not consider the propagation loss in the waveguide. The typical propagation loss of 0.2 dB/cm has been observed (see section 3.3.3) in similar devices using a grating-based technique [14], and a physical cut-back method [3]. Propagation losses depend on the fluence, the spot size of the UV laser [14], and the thickness of the FHD deposited core layer. Increasing the writing fluence causes a greater index difference between the written core and surrounding material, leading to higher waveguide NA, better mode field confinement and lower propagation losses. However, a higher average power may also lead to increased propagation loss due to damage-induced scattering. This has been discussed previously in [14]. However, we believe these to have minimal effect in these experiments.

4.5.1 Alignment and out-gassing investigation

Additionally, the chip contained eight other test waveguides to monitor the alignment and effects of hydrogen out-gassing. Figure 4.13(a) shows n_{eff} and Δn_{ac} of the four waveguides written at the fluence of 1 kJ cm^{-2} and 3.6 mW of writing power. To investigate alignment, these waveguides were inscribed at different positions, over 7 mm of the distance across the chip. Both n_{eff} and Δn_{ac} slightly increase as the UV beam moves from the first to last alignment waveguide. Typically waveguide and grating properties slightly vary with the miss alignment of two spots due to surface flatness when a 7.8-micron beam moves across a 20 mm $\times$10 mm chip. However, the resultant variation in n_{eff} and grating strength shown in Fig. 4.13(a) is insignificant. Similarly, four waveguides were written to examine the effect of hydrogen out-gassing. These waveguides were inscribed next to alignment waveguides for over 300 minutes. With continuous hydrogen out-gassing, we would expect a reduction in photosensitivity response and the grating strength. However, the data shown in Fig. 4.13(b) does not indicate changes related to hydrogen-enhanced photosensitivity, probably due to hydrogen locking, as discussed in section 3.7. Table 4.1 shows the mean n_{eff} and Δn_{ac} measured from the waveguides written to examine UV alignment and hydrogen out-gassing.

Mean values	Alignment waveguides	Photosensitivity waveguides
n_{eff}	$1.44871 \pm 5 \times 10^{-5}$	$1.44872 \pm 7 \times 10^{-5}$
Δn_{ac}	$4.8 \times 10^{-4} \pm 2 \times 10^{-5}$	$5.1 \times 10^{-4} \pm 2^{-5}$

TABLE 4.1: Estimated mean n_{eff} and Δn_{ac} of waveguides and gratings written to probe effects associated with the alignment of UV spots and hydrogen out-gassing during fabrication. The error bars in these plots correspond to the standard error.

4.5.2 Response of photosensitivity and the grating strength

Figure 4.14 shows a plot of variation in n_{eff} and Δn_{ac} for each 1.5 mm long grating as a function of writing fluence at different laser powers. At all writing powers, the n_{eff} response shows a similar trend (as seen in [2]) where a positive increase in the effective refractive index is observed. The n_{eff} response is associated with the red shift in central

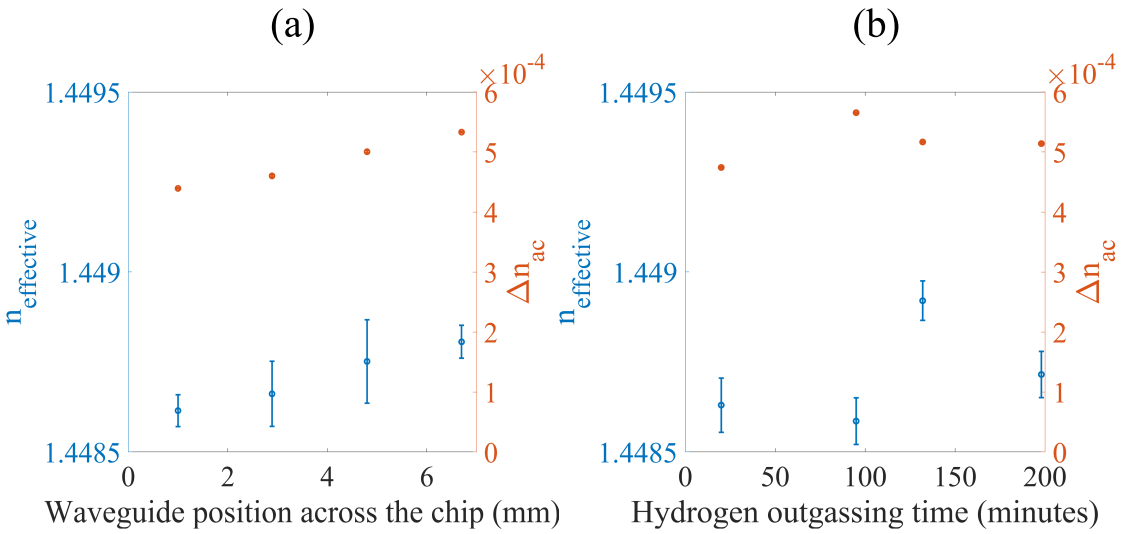

FIGURE 4.13: Plots of n_{eff} and Δn_{ac} of the reference waveguides written to probe the spatial and temporal effects associated with UV writing characteristics. The effects on photosensitivity and grating's strength due to the overlap of dual-beam spot are plotted in (a) and the response of hydrogen out-gassing is shown in (b). These waveguides were written at a fluence of 1 kJ cm^{-2} and 3.6 mW of writing power. The error bars given in these plots correspond to the standard deviation of modelled fit plotted over the experimental data using a Python optimiser.

wavelength can be explained typically on the basis of photo-chemical changes in colour centres due to laser exposure. However, it is interesting to observe the different trends in grating modulation Δn_{ac} as a function of writing powers and fluence. At the low powers of 0.5 and 1.7 mW, we observe an increase in Δn_{ac} followed by saturation with increasing fluence from 0.4 to 2.2 kJ cm^{-2}. On increasing the writing power from 2.6 to 7.3 mW, the Δn_{ac} increases to a peak value of 5.1×10^{-4} around a fluence of 1 kJ cm^{-2} and begins to reduce with a further increase in fluence. In this power range, the response of Δn_{ac} can be well understood by looking at the change in n_{eff} where grating modulation increases with the increase in n_{eff} and depletes as photosensitivity begins to saturate. At the highest power of 11.6 mW, we observe an entirely different response in grating strength. However, as we observe damage in these waveguides, it is difficult to trust the reflectivity measurements due to the perceived increase in loss. However, we do not observe any negative change in refractive index as a function of laser fluence; contrary to our observations, Pissadakis et al. [15] have reported the transition of gratings from type I to type In in B/Ge doped hydrogen-free fibres in a similar fluence range of 1 to 3 kJ cm^{-2}. Although in this work, a picosecond laser was used. Furthermore, it is difficult to compare our grating properties to FBG due to different compositions of doped silica, hydrogen-loaded samples, and fabrication methods.

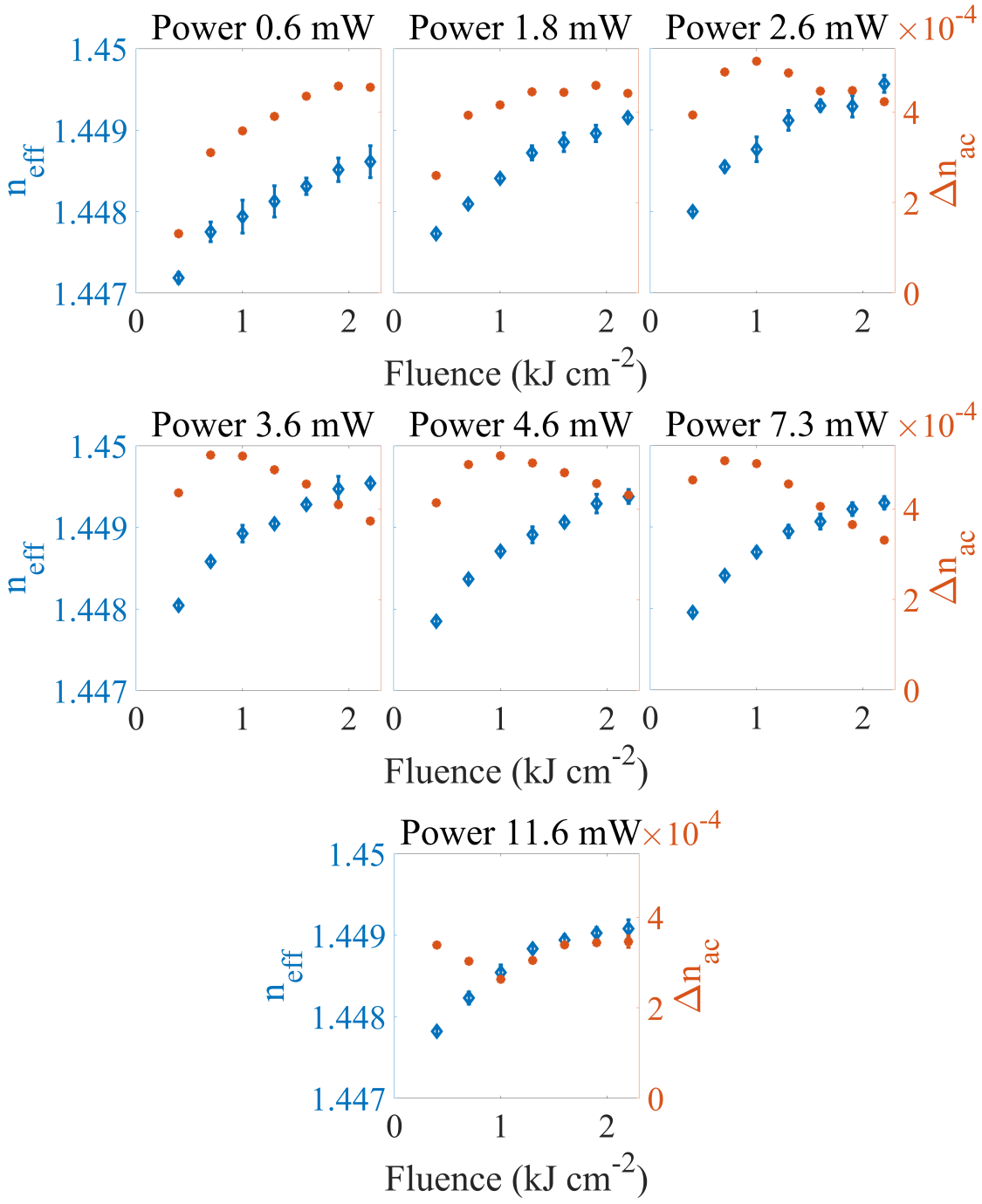

FIGURE 4.14: Plot of n_{eff} and Δn_{ac} as a function of fluence at writing beam powers ranging from 0.6 to 11.6 mW.

In order to demonstrate a clear dependence of n_{eff} on writing power and fluence, we plot n_{eff} as a function of fluence on a linear-log scale in Figure 4.15 (a). A similar plot of n_{eff} as a function of laser pulses per micron is shown in Figure 4.15 (b). At all writing powers, we observe that n_{eff} increases logarithmically and follows a linear trend line on a linear-log scale. At lower writing powers ranging from 0.5 to 4.64 mW, the gradient of linear trend lines agrees within error. However, the differing offset (increased n_{eff}) within a fluence range of 0.4 to 2.2 kJ cm^{-2} shows that an increased writing power advances the saturation in photosensitivity for the same fluence. Increasing the writing power to

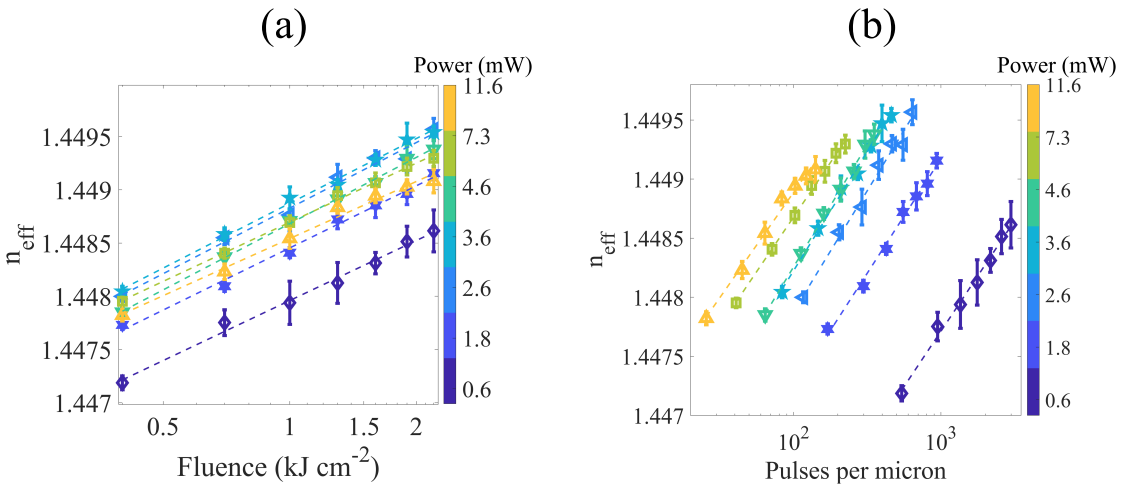

FIGURE 4.15: Plot of n_{eff} as a function of fluence in (a) and laser pulses per micron in (b) in a linear-log scale.

7.3 and 11.6 mW leads to a reduced gradient of the trends, as shown in Figure 4.15, suggesting the saturation of photosensitivity response is more abrupt. We would expect to have the same value of n_{eff} at zero fluence suggesting a non-linear trend between fluence zero and 0.4 kJ cm^{-2}. However, it is challenging to evaluate the photosensitivity response of a planar sample at very low fluences due to the absence of a pre-defined waveguide.

4.5.3 Birefringence

We also observed variation in the birefringence ($n_{eff}^{TM} - n_{eff}^{TE}$) depending upon writing power and fluences shown in Figure 4.16.

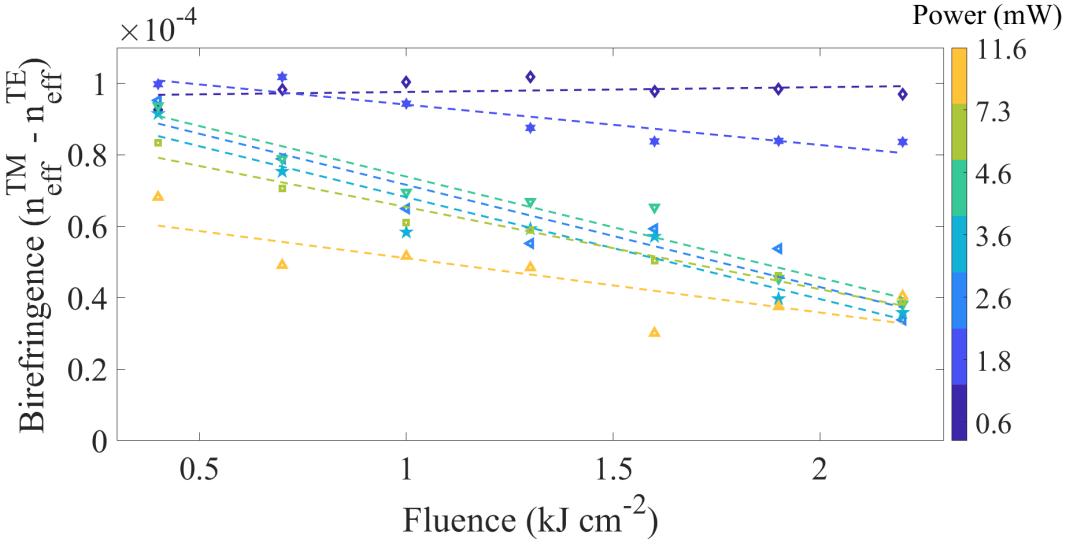

FIGURE 4.16: Birefringence measurement as a function of increasing fluence at writing powers ranging from 0.5 to 11.6 mW.

The inherent birefringence appears to be 1×10^{-4} due to the stress and geometry of our planar silica-on-silicon structure.

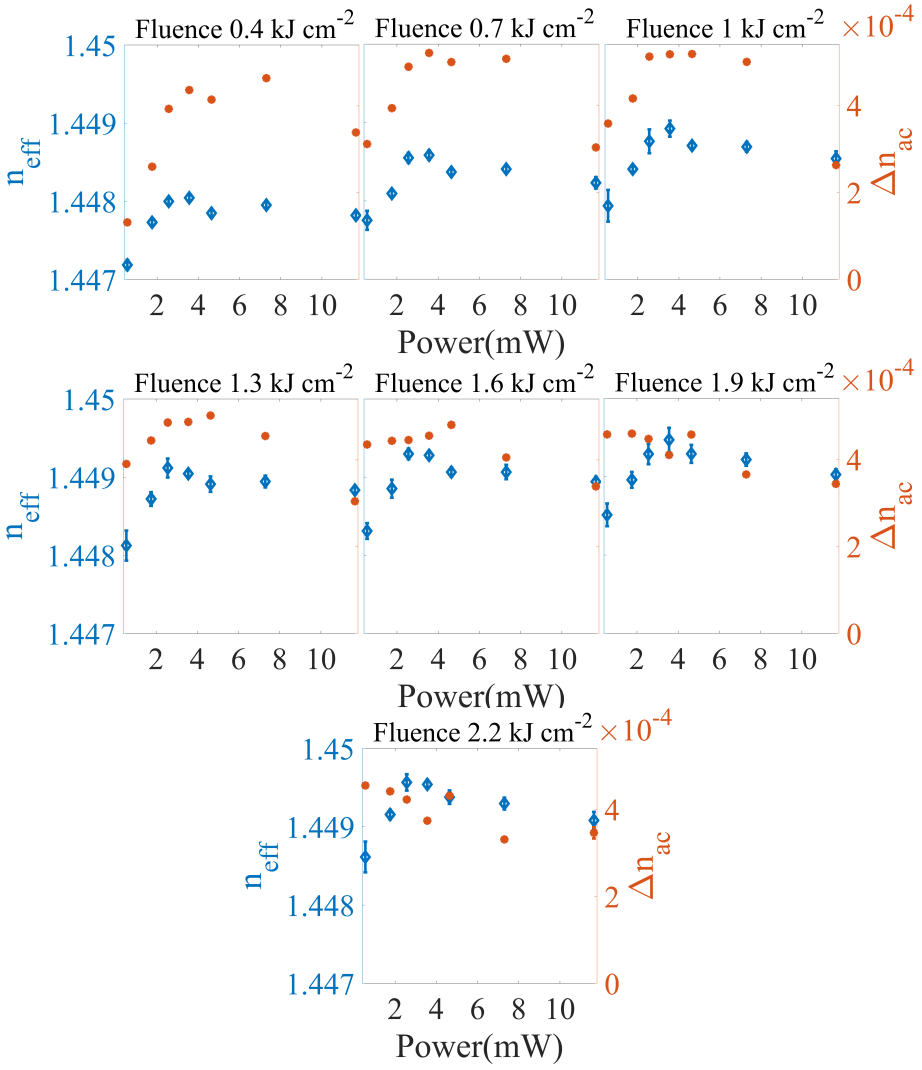

FIGURE 4.17: Plot of n_{eff} and Δn_{ac} as a function of writing power. Compared to Fig. 4.14, we again plotted the same data in an alternative way to visualise the effect of writing power on waveguide and grating properties. At all fluences, we observe the positive change in n_{eff} with increasing writing power upto 3.6 mW. Above 3.6 mW slight reduction in n_{eff} can be seen. We observe damage at writing powers of 7.3 and 11.6 mW, it is difficult to trust the reflectivity measurements and Δn_{ac} due to losses in the waveguides. The maximum value of Δn_{ac} is achieved at a fluence of 1 kJ cm^{-2} at writing power ranging from 2.6 to 4.6 mW suggesting the ideal writing regime for defining strong and high-quality gratings.

Increasing writing fluence at the lowest writing power of 0.5 mW does not contribute to significant variation. With an increasing writing power, birefringence follows a negative correlation with the fluence as was seen previously with 244 nm laser processing [16]. UV writing increases the refractive index of the core layer, which can reduce the birefringence due to modal power confinement. Additionally, local stresses near the waveguide can also dominate stress-induced polarisation effects.

Figures 4.15 and 4.16 clearly demonstrate that the writing power in 213 nm laser inscription is a crucial parameter to decide the response of photosensitivity (see Figure 4.17). Devices made with the lowest writing power of 0.5 mW show the lowest n_{eff} for all fluences; correspondingly, these waveguides written at 0.5 mW are the most birefringent.

UV writing experiments using a CW 244 nm laser are conventionally expected to exhibit a photosensitivity response proportional to fluence, and independent of the writing power. However, the variation in photosensitivity and birefringence with increasing writing power (using a pulsed 213 nm laser) may be associated with the pulsed nature of the laser and thermal effects. Additionally, it is also possible that higher pulse energies no longer follow the same photosensitivity model as for lower pulse energies and more than one physical process, such as heating and damage, is involved in determining the net change in refractive index [17]. A mixing of the photo-induced chemical changes and densification-related processes could potentially describe the different photosensitivity behaviours in this experiment. The photo-induced chemical mechanism gives a positive refractive index change, saturating when all species have been reacted, whereas densification can lead to more complex refractive index behaviour. At higher powers, the Kramers-Kronig effect may be dominated by heating or damage-related processes.

4.6 Conclusions

For the first time, we have extensively investigated the regimes (power and fluence relationship) of SSDUW using 213 nm light. This chapter discusses the non-typical effects of writing power and fluence on the induced effective change in the refractive index and gratings strength. Compared to [1], [18], we have used higher peak intensities (up to 0.58 GW cm^{-2}) to define waveguides and Bragg gratings in doped silica. Contrary to [1], we have not seen any significant evidence of similar non-linear photosensitivity response in B/Ge silica. However, we do observe a subtle non-linearity where gratings and waveguide properties depend on writing power. However, it is challenging to draw comparisons due to the different compositions of glass, the geometry of planar sample and effect of doping and hydrogen loading. We observe that writing powers of 2.5 to 4.6 mW are ideal for SSDUW, where we suppose the change in the refractive index upon laser exposure is dominated by photochemical changes. In this writing regime, grating strength is maximum at a fluence of 1 kJ cm^{-2} and the photosensitivity response appears to be optimum, an essential feature to fabricate complex devices. The maximum value of Δn_{ac} observed in this study is $5.1\times\ 10^{-4}$. However, the grating strength is intentionally reduced for these experiments and we can achieve Δn_{ac} up to $1.25\times\ 10^{-3}$ which is higher compared to 244 nm writing experiments [19]. Above powers of 4.6 mW, the data suggests additional refractive index change caused by damage-induced stress and leads to photosensitivity saturation at lower fluences and reduced grating strength. Light microscopy also showed that the use of high writing power leads to localized damage of the silica-silicon interface. This work enables direct UV writing with 213 nm laser light, as a route to local phase trimming of dielectric materials.

A part of this work is published in 'Optical materials express', [20] and conference proceeding in [21].

4.7 References

[1] M. Gagné and R. Kashyap, "New nanosecond Q-switched Nd:VO_4 laser fifth harmonic for fast hydrogen-free fiber Bragg gratings fabrication," *Optics Communications*, vol. 283, no. 24, pp. 5028–5032, 2010.

[2] Q. S. Ahmed, P. C. Gow, C. Holmes, P. L. Mennea, J. W. Field, R. H. S. Bannerman, D. H. Smith, C. B. Gawith, P. G. R. Smith, and J. C. Gates, "Direct UV written waveguides and Bragg gratings in doped planar silica using a 213 nm laser," *Electronics Letters*, vol. 57, no. 8, pp. 331–333, 2021.

[3] H. L. Rogers, S. Ambran, C. Holmes, P. G. R. Smith, and J. C. Gates, "In situ loss measurement of direct UV-written waveguides using integrated Bragg gratings," *Opt. Lett.*, vol. 35, no. 17, pp. 2849–2851, 2010.

[4] R. H. S. Bannerman, "Microfabrication of waveguide-based devices for quantum optics," Ph.D. dissertation, University of Southampton, 2019.

[5] P. C. Gow, Q. S. Ahmed, J. C. Gates, P. G. R. Smith, and C. Holmes, "Microwave consolidation of UV photosensitive doped silica for integrated photonics," *Optical Materials Express*, vol. 11, no. 6, pp. 1835–1841, 2021.

[6] H. L. Rogers, "Direct UV-written Bragg gratings for waveguide characterisation and advanced applications," Ph.D. dissertation, University of Southampton, 2013.

[7] J. Canning, D. Moss, M. Aslund, and M. Bazylenko, "A study of negative index grating growth in germanosilicate planar waveguides," *Optical and quantum electronics*, vol. 31, pp. 469–480, 1999.

[8] J. Canning, D. Moss, M. Aslund, and M. Bazylenko, "Negative index gratings in germanosilicate planar waveguides," *Electronics Letters*, vol. 34, no. 4, pp. 366–367, 1998.

[9] G. Heinrich, M. Bähr, K. Stolberg, T. Wütherich, M. Leonhardt, and A. Lawerenz, "Investigation of ablation mechanisms for selective laser ablation of silicon nitride layers," *Energy Procedia*, vol. 8, pp. 592–597, 2011.

[10] T.-h. Kim, H. Adeli, A. Stoica, and B.-H. Kang, "Control and automation, and energy system engineering," 2011.

[11] Z. H. Wang, G.-D. Peng, and P. L. Chu, "Improved Rouard's method for fiber and waveguide gratings," *Optics communications*, vol. 177, no. 1-6, pp. 245–250, 2000.

[12] A. S. Othonos and K. Kalli, *Fiber Bragg gratings fundamentals and applications in telecommunications and sensing*. Artech house, 1999.

[13] M. A. Muriel and A. Carballar, "Internal field distributions in fiber Bragg gratings," *IEEE Photonics technology letters*, vol. 9, no. 7, pp. 955–957, 1997.

[14] P. C. Gow, R. H. S. Bannerman, P. L. Mennea, C. Holmes, J. C. Gates, and P. G. R. Smith, "Direct UV written integrated planar waveguides using a 213 nm laser," *Optics express*, vol. 27, no. 20, pp. 29 133–29 138, 2019.

[15] S. Pissadakis and M. Konstantaki, "Type IIA gratings recorded in B-Ge codoped optical fibre using 213 nm Nd: Yag radiation," in *2005 31st European Conference on Optical Communication, ECOC 2005*, IET, vol. 3, 2005, pp. 563–564.

[16] P. Holmberg, F. Laurell, and M. Fokine, "Influence of pre-annealing on the thermal regeneration of fiber Bragg gratings in standard optical fibers," *Optics Express*, vol. 23, no. 21, pp. 27 520–27 535, 2015.

[17] K. P. Chen, P. R. Herman, R. Taylor, and C. Hnatovsky, "Vacuum-ultraviolet laser-induced refractive-index change and birefringence in standard optical fibers," *Journal of lightwave technology*, vol. 21, no. 9, p. 1969, 2003.

[18] S. Pissadakis and M. Konstantaki, "Grating inscription in optical fibres using 213 nm picosecond radiation: A new route in silicate glass photosensitivity," in *Proceedings of 2005 7th International Conference Transparent Optical Networks, 2005.*, IEEE, vol. 1, 2005, pp. 337–342.

[19] C. Sima, J. C. Gates, H. L. Rogers, P. L. Mennea, C. Holmes, M. N. Zervas, and P. G. R. Smith, "Ultra-wide detuning planar Bragg grating fabrication technique based on direct UV grating writing with electro-optic phase modulation," *Optics express*, vol. 21, no. 13, pp. 15 747–15 754, 2013.

[20] Q. S. Ahmed, J. W. Field, C. Holmes, S. Z. Oo, P. L. Mennea, R. H. S. Bannerman, R. Cecil, G. Churchill, C. B. E. Gawith, P. G. R. Smith, *et al.*, "Investigation into the writing dynamics of planar bragg gratings using pulsed 213 nm radiation," *Optical Materials Express*, vol. 13, no. 2, pp. 495–503, 2023.

[21] Q. S. Ahmed, J. W. Field, P. C. Gow, S. Z. Oo, C. Holmes, R. H. S. Bannerman, P. L. Mennea, C. B. E. Gawith, P. G. R. Smith, and J. C. Gates, "Photosensitivity response of pulsed 213 nm light in planar Bragg grating writing," in *Bragg Gratings, Photosensitivity and Poling in Glass Waveguides and Materials*, Optica Publishing Group, 2022, BM3A–6.

Chapter 5

Holographically fabricated out-of-plane 45° blazed grating couplers for integrated free space beam delivery

chapteroop) Chapters 3 and 4 provided an essential understanding of 213 nm UV writing dynamics and give critical information on UV writing parameters. In previous chapters, I have discussed in-plane gratings with a grating plane normal to the direction of wave propagation. Here, we will explore another class of gratings oriented at a blaze angle to the light propagation axis. This chapter will discuss blazed gratings' theory and experimental demonstration for out-of-plane beam coupling.

This work was conducted in collaboration with a modelling group (Dr Peter Horak and Dong-Woo Ko) at ORC in Southampton. Experimental work was first closely supervised by Dr Paul Gow, and later jointly performed with Dr James Field a postdoctoral fellow, on a UKRI project (QT Assemble). This chapter will discuss the fabrication of out-of-plane grating couplers holographically written in a silica-on-silicon platform using a 213 nm laser. For this purpose, an entirely new interferometric board was designed for inscribing grating planes in planar silica at a 45° blaze angle. The fabrication approach was non-trivial and faced several engineering challenges; this chapter will discuss the work to overcome these challenges. Later we will demonstrate a 1D out-of-plane grating coupler (45° blazed gratings in a channel waveguide) holographically fabricated in planar silica. Finally, a 2D (large-area) grating coupler prototype will be presented.

I have worked on designing and building interferometric boards for out-of-plane 45° blazed grating inscriptions. Dong-Woo and James Field performed all the numerical and analytical simulations. The fabrication, characterisation and analysis for the 1D grating coupler are solely my work. Finally, a 2D grating coupler was fabricated and analysed jointly with James Field.

5.1 Diffraction grating

A diffraction grating is an optical component consisting of a surface with a periodic structure of closely spaced parallel lines or grooves, diffracting light into its spectral components. When light is incident upon the grating, it is diffracted into multiple orders (or angles) depending on the spacing of the lines or grooves and the wavelength of the light. This phenomenon is used in various applications, such as spectroscopy, where the diffracted light can separate the different wavelengths of light and create a spectrum. The properties of a diffraction grating depend on factors such as the spacing between the lines, the angle of incidence of the light, and the angle of diffraction. The efficiency of specific diffraction orders can be enhanced by introducing a sawtooth-like profile to the design of the reflection grating. Such a particular reflection design of a grating is called blazed grating and is shown in Fig. 5.1.

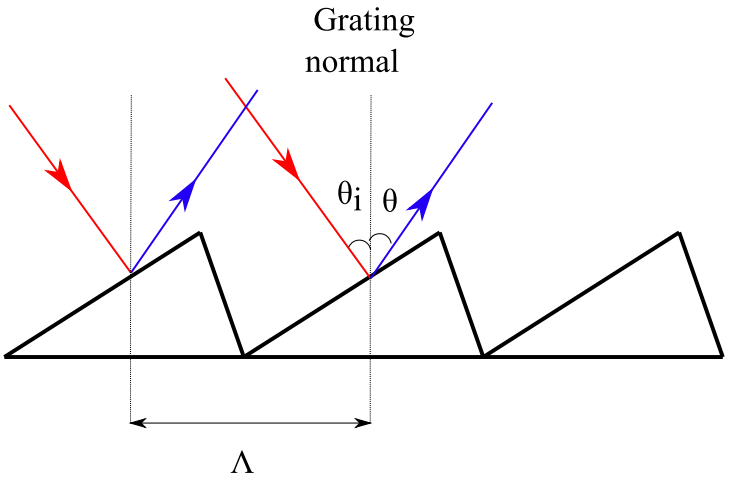

FIGURE 5.1: Schematic of the blazed gratings with a period Λ, where incoming electromagnetic rays incident at an angle of θ_i and diffract at the angle θ .

In Fig.5.1, an electromagnetic wave of wavelength λ incident on a grating structure with the period Λ at an angle θ_i, the N_{th} diffracted beam, with the angle θ is governed by equation 5.1,

$$\Lambda(sin\theta + sin\theta_i) = N\lambda \tag{5.1}$$

When light enters a blazed grating, it is diffracted into different angles depending on its wavelength. The diffraction efficiency of a blazed grating is highest for a specific wavelength and decreases for other wavelengths. The grating period decides the diffraction angle of input light, but the blaze angle provides directionality and enhanced efficiency. We refer the reader to follow further details [1]. UV laser-written blazed Bragg gratings in silica were used to tap light out of the fibre core [2]. It was later shown that the fibre output could be focused by changing the grating period [3]. Blazed gratings in fibre [4] and on an integrated planar platform [5] are recognised as a route to provide polarisation filtering, highlighting their potential to be used in polarisers, and spectrometers [6].

5.2 Chirped grating

Chirped gratings are periodic structures consisting of a sequence of grooves into a material like glass, with a pitch that varies spatially along the length of the grating (see Fig. 5.2). In a chirped grating, the spatial variation of the pitch affects the phase of the reflected and transmitted light waves. This phase shift depends on the position within the grating and the wavelength of the light. Thus, by controlling the chirp, one can manipulate the spectral response of the grating. The chirped grating within a waveguide was first reported by Byron et al. [7], who used a dual beam UV interferometer to inscribe uniform fringe patterns in a tapered photosensitive fibre. Similarly, the uniform period exposure was used in [8], and chirp was introduced by bending the fibre with respect to interference fringes. The approach results in a fringe separation that continuously varies along the exposed fibre length. Chirped gratings find applications in various fields, including telecommunications, spectroscopy and pulse shortening. For example, in telecommunications, these gratings compensate for the dispersion of optical signals in fibre-optic networks. The diffracted beam can be shaped and focused using chirped-blazed gratings by changing the grating period over a fixed grating length. Such types of gratings are called chirp-blazed gratings [6]. In 2020, Dr James Field used the chirp-blazed gratings approach for miniaturised blazed grating-based spectrometers [6]. In the later section of Chapter 5, the chirped blazed gratings will be utilized for out-of-plane light focusing.

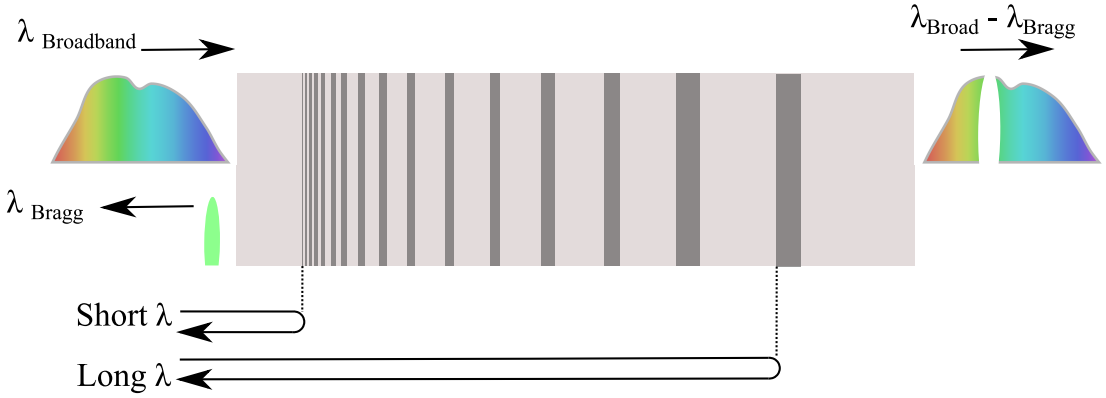

FIGURE 5.2: A schematic diagram of a chirped grating with an aperiodic pitch is shown, where $\lambda_{\text{Broadband}}$ serves as the input source and λ_{Bragg} is the reflected mode. Owing to the aperiodic pitch, longer wavelengths penetrate deeper into the grating before reflecting.

5.3 Design of 45° blazed gratings using dual beam UV exposure

Here we consider a 45° blazed grating design, which will be holographically fabricated in planar silica using 213 nm light. The following derivation will give us information about the required period of the 45° blazed grating to couple 780 nm light out-of-plane as a free space beam. We infer the required incident angles from the grating period for UV beams to interfere and generate 45° blazed gratings. The 45° blaze angle was selected for the grating due to the highly polarised nature and directionality of the diffracted beam [9].

Fig. 5.3 shows the schematic of blazed gratings within a channel waveguide. In the diagram incident wave vector is denoted by K_i, K_r shows the reflected wave vector and K_G is the grating vector.

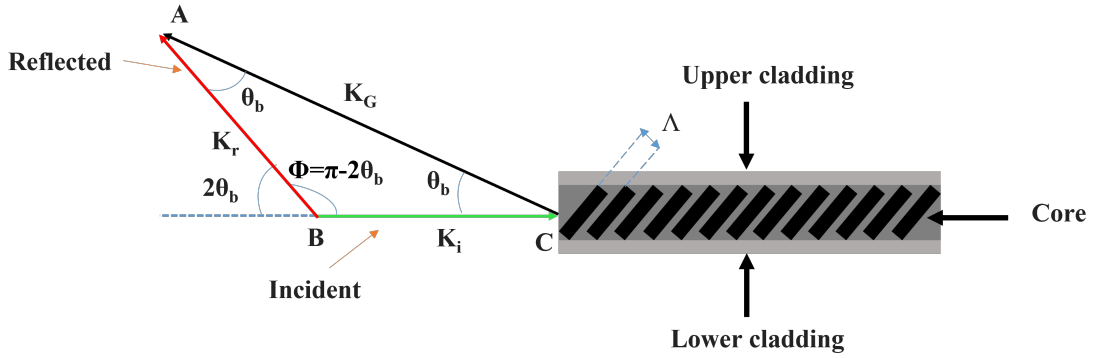

FIGURE 5.3: Schematic of blazed gratings within a channel waveguide, where K_i, K_r denote the equal wave vectors of the incident and reflected light respectively and K_G stands for the grating vector.

Consider $|K_i| = |K_r| = |K|$ (energy conservation) and $\phi = \pi - 2\theta_b$. By applying cosine law on the ABC triangle defined in Fig. 5.3 we derive,

$$|K|^2 + |K|^2 - 2|K||K|\cos(\pi - 2\theta_b) = |K_G|^2 \tag{5.2}$$

Cos is -ve in the second quadrant (assuming $0<\theta_b<90$)

$$|K|^2 + |K|^2 + 2|K||K|\cos(2\theta_b) = |K_G|^2 \tag{5.3}$$

Rearranging the equation 5.3,

$$(1 + \cos(2\theta_b)) = \frac{|K_G|^2}{2|K|^2} \tag{5.4}$$

Dividing both sides of equation 5.3 by 2 we get,

$$\frac{(1 + \cos(2\theta_b))}{2} = \frac{|K_G|^2}{4|K|^2} \tag{5.5}$$

Taking square root on both sides of equation 5.4,

$$\sqrt{\frac{(1 + \cos(2\theta_b))}{2}} = \sqrt{\frac{|K_G|^2}{4|K|^2}} \tag{5.6}$$

Using $\cos\frac{\theta}{2} = \sqrt{\frac{1+\cos\theta}{2}}$,

$$K = \frac{K_G}{2\cos\theta_b}. \tag{5.7}$$

In equation 5.7, K is the incident or reflected wave vector, θ_b is the angle of grating tilt and K_G is the grating vector. Substituting $K = 2\pi n_{\text{eff}}/\lambda$ and $K_G = 2\pi/\Lambda$ in equation

5.7 we obtain,

$$\Lambda = \frac{\lambda}{2n_{\text{eff}} \cos\theta_b}, \tag{5.8}$$

where Λ is the grating period. Substituting the values of the reflected wavelength (λ= 780 nm), $\theta_b = 45°$ and $n_{\text{eff}} = 1.47$ in equation 5.8, we can calculate the grating period Λ =375 nm. The period of interference fringes by dual-beam interferometry is defined by equation 5.9.

$$\Lambda = \frac{\lambda_{\text{UV}}}{2\sin\frac{\theta}{2}}. \tag{5.9}$$

Where Λ is the fringe period of the interference pattern, $\lambda_{\text{UV}} = 213$ nm, and $\frac{\theta}{2}$ is the half angle of the two beams of the interferometer. This gives us a half angle $\frac{\theta}{2}$ of 16.3 °.

5.4 Bandwidth and sensitivity of 45° blazed gratings

This section will discuss the bandwidth and sensitivity of UV-written blazed gratings. The grating strength, period and blaze angle are crucial parameters to determine the coupling efficiency of a blazed grating. Dong-Woo performed analytical and numeric simulations to investigate the bandwidth sensitivity of UV-written blazed gratings [9].

5.4.1 Grating strength

The grating strength is a key parameter for the determination of coupling efficiency. We must enhance the grating strength or modulated refractive index (Δn_{ac}) to increase the coupling efficiency. UV-written gratings provide lower index contrast and coupling efficiency compared to etched gratings. Figure 5.4 shows an analytic plot of coupling efficiency for a blazed grating against the modulated refractive index. The coupling efficiencies non-linearly increase with the increasing Δn_{ac} and saturate at Δn_{ac} of 5×10^{-3}. Since 1.25×10^{-3} was the highest Δn_{ac} experimentally observed using 213 nm processing (see Chapters 3 and 4), we regard it as a suitable value for modelling blazed gratings. In Fig. 5.4, red dotted lines show the experimentally achieved Δn_{ac} and corresponding coupling efficiency, which is $\sim$ 25 %. The coupling efficiencies for a 10 mm long blazed grating can be increased up to 60 %.

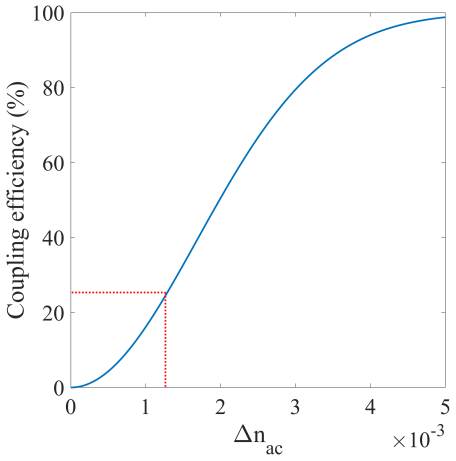

FIGURE 5.4: An analytic plot of coupling efficiency against the grating strength (Δn_{ac}) for a 3 mm long blazed grating.

5.4.2 Input wavelength

It is impossible to accurately examine the bandwidth of the grating period without changing the grating design, as the number of grating planes in a fixed grating length varies depending upon the grating period. However, the bandwidth for the grating period can be investigated indirectly by changing the wavelength of the input mode without affecting the grating design. Since the input wavelength is in the same order of magnitude as the grating period, it is a good substitute for the bandwidth sensitivity of the grating period. Figure 5.5 plots coupling efficiencies vs input wavelength for a 3 mm long 45° blazed grating at Δn_{ac} of 1.25×10^{-3}. The shape of the plot appears to be Gaussian, with a bandwidth of 87.3 nm. In contrast, the bandwidth of normal Bragg gratings was found to be less than 1 nm (see Chapter 3). This indicates that devices made using the blazed grating approach are highly broadband.

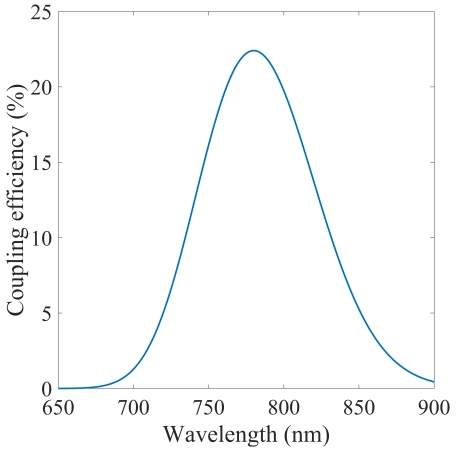

FIGURE 5.5: A plot of an analytic solution for the coupling efficiency against the input wavelength for a 3 mm long blazed grating.

5.4.3 Blaze angle

Figure 5.6 shows a plot of coupling efficiency against the blaze angle for a fixed grating period. The blaze angle appears to be a critical aspect for determining the efficiency of the blazed grating. Unlike the input wavelength, the bandwidth for a blaze angle is very low for the blaze angle with an FWHM of 3.21°. By looking at the plot, it seems evident that coupling efficiency completely vanishes at ±5° deviation from a 45° blaze angle. In the later section, we will discuss the angle of the UV interferometer beams will define the blaze angle.

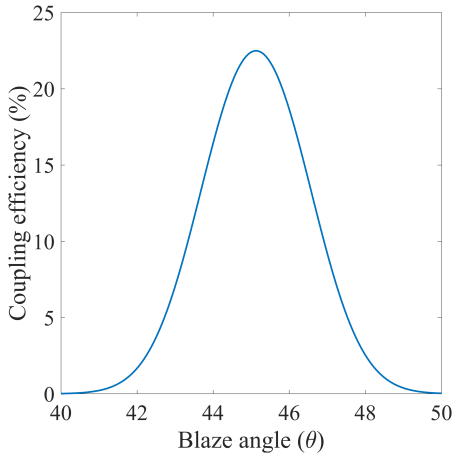

FIGURE 5.6: A plot of an analytic solution for the coupling efficiency against the blaze angle for a 3 mm long blazed grating.

5.5 Prism coupling mechanism

Fabricating gratings in planar silica with a blaze angle of 45 ° with respect to surface normal is challenging using dual beam interferometry. The challenge comes from the large angles of the incident UV beams, resulting in significant Fresnel losses and making it impossible to couple the incident light into silica at the desired angles for 45° blaze angle. In order to overcome this limitation, we proposed a prism coupling mechanism [10]–[12] to allow coupling and reduce the power imbalance in the two beams. Consider the simple case in which two beams interfere to generate a fringe pattern at an angle of 45° with respect to chip normal as shown in Fig. 5.7. One arm of the interferometer is at an angle of 28.7° and is considered beam A the other arm is at a larger angle of 61.3° and is called beam B. Loss of power in terms of reflection from one medium to other can be calculated using Fresnel coefficients [13] shown in equations 5.10 and 5.11,

$$R_s = \left| \frac{n_1 \cos\theta_i - n_2 \sqrt{1 - (\frac{n_1 \times \sin\theta_i}{n_2})^2}}{n_1 \cos\theta_i + n_2 \sqrt{1 - (\frac{n_1 \times \sin\theta_i}{n_2})^2}} \right|^2, \tag{5.10}$$

$$R_p = \left| \frac{n_1 \sqrt{1 - (\frac{n_1 \times \sin\theta_i}{n_2})^2} - n_2 \cos\theta_i}{n_1 \sqrt{1 - (\frac{n_1 \times \sin\theta_i}{n_2})^2} + n_2 \cos\theta_i} \right|^2, \tag{5.11}$$

Where θ_i is the angle of incidence with respect to normal, n_1 is the refractive index of air which is very close to 1, and n_2 is the refractive index of FHD silica ($\sim$ 1.535 for 213 nm). Figure 5.7 demonstrates the concept in which beam A and B are incident at an angle of 16.3° with respect to the 45° prism.

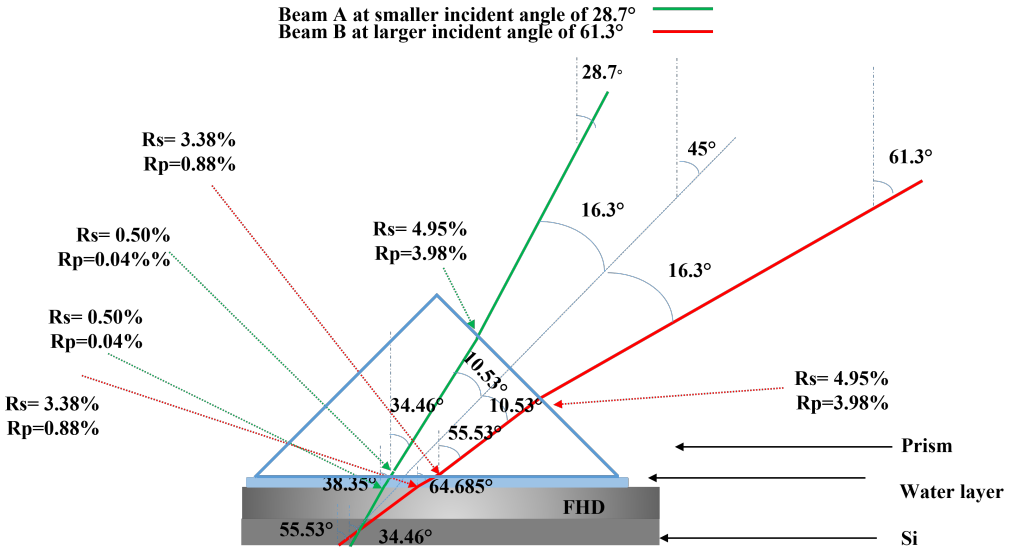

FIGURE 5.7: Diagram of the Fresnel reflections at the surface of the prism, water and FHD silica when a 213 nm laser is incident to generate the out-of-plane grating coupler.

In this case, the Fresnel losses are minimised due to the smaller angle of incidence. After passing through the prism, both beams are focused on the FHD sample. Between the prism surface and the FHD silica chip, an index-matched fluid (i.e. de-ionised water) can be introduced. By utilising the above methodology, both beams suffer minimum reflection loss and power imbalance, offering the potential for high contrast refractive index gratings. Both beams interfere with $\sim$ 9% of the power reduction inside the core layer. Fresnel reflection coefficients at each interface (i.e. glass prism, water (n $\approx$1.40 at 213 nm) and FHD silica) in the scenario shown in Fig. 5.7 are computed and summarised in Table 5.1.

Fresnel Reflection Coefficient	Air-Prism	Prism-water	Water-FHD silica	Total loss
Rs (s-polarisation)	0.0495 for both beams A and B	0.0338 for beam A and 0.005 for beam B	0.005 for beam A and 0.0338 for beam B	0.088 for both beams A and B
Rp (p-polarisation)	0.0398 for both beams A and B	0.0088 for beam A and 0.0004 for beam B	0.0004 for beam A and 0.0088 for beam B	0.049 for both beams A and B

TABLE 5.1: Calculated Fresnel reflection coefficients for each interface of the scenario shown in Fig.5.2.

5.6 Initial tests for the fabrication of channel waveguide and out-of-plane 45° blazed gratings

A new interferometer arrangement was designed for initial tests to generate 45° blazed gratings by dual-beam UV writing. A setup schematic is shown in Fig. 5.8. In this writing system, a planoconvex lens with a focal length of 50 cm was used to focus the laser. After passing through the focusing lens, the beam splits into two arms by a 50:50 beam splitter. One arm of the interferometer is passed through the EOM, and both arms are focused at the spot size of ∼15 μm. We designed the interferometer to have the same focal length in both arms of the interferometer. The path length is a less concerning parameter due to ∼1 metre coherence length of 213 nm laser; for 244 nm CW laser, the coherence length is limited to 1 cm. A prism was mounted on a rail, and a ∼100 μm layer of de-ionised water was introduced for an index match between the sample and the prism's bottom surface. During the UV fabrication, the prism was fixed and the sample was translated using the Aerotech air-bearing stages.

Layer	Silicon	THOX	PX194	Upper-clad
Thickness μm	1000	15	3.31	17.7
Refractive index (780 nm)	3.71	1.4537	1.4608	1.4555

TABLE 5.2: Details of deposited layers.

The recipe, PX194 (see Appendix 1 for complete deposition details), was used to get a single-mode operation at 780 nm wavelength. The resulting parameters are summarised in Table 5.2. Individual chips measuring 10 × 20 mm were diced from this wafer and hydrogen-loaded before the UV writing.

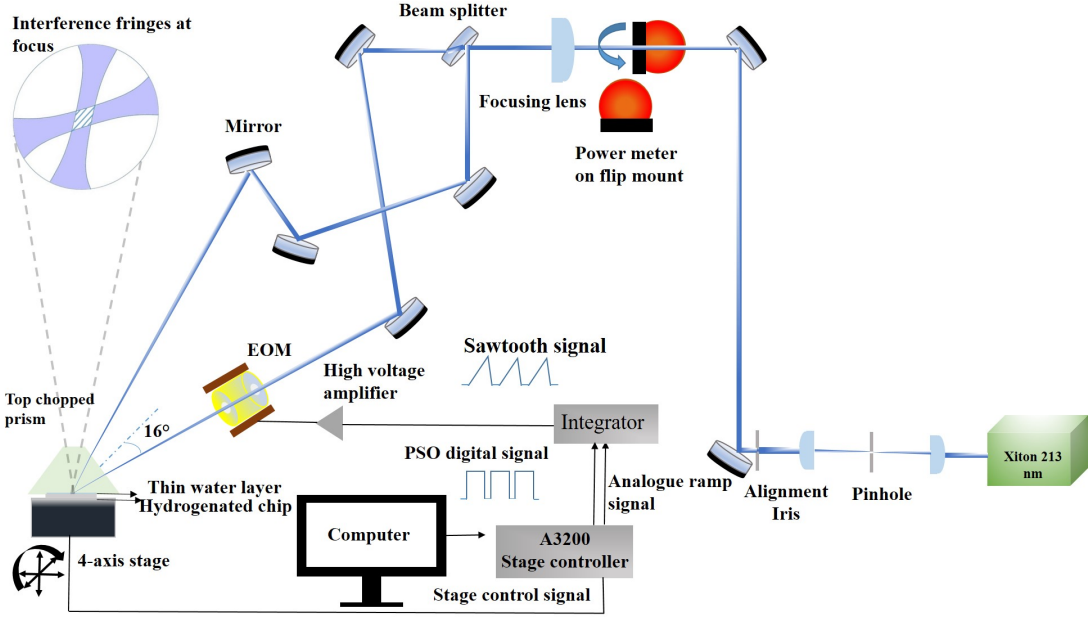

FIGURE 5.8: Schematic of the 213 nm UV writing system for the fabrication of tilted gratings using prism coupling mechanism.

We fabricated a channel waveguide and uniform gratings at a fluence of 1 kJ cm^{-2}. At the end of fabrication, there was no water left on the surface of the chip, and we were concerned that fabrication had not been successful. However, characterisation did show some 780 nm laser coupling to free space from the input mode. Figure 5.9 shows a photograph of a fabricated chip aligned with a fibre v-groove assembly to launch 780 nm inside the waveguide.

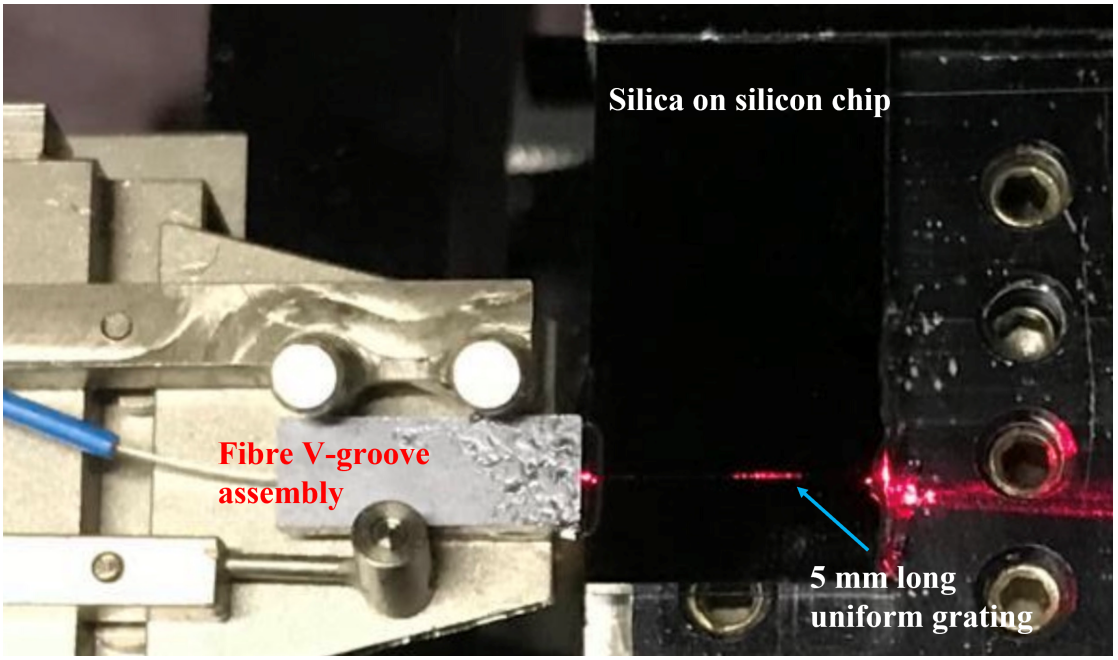

FIGURE 5.9: Photograph of fabricated chip shows a 5 mm uniform blazed grating. 780 nm light was launched into the chip through fibre V-groove assembly.

5.7 Fabrication challenges

The 45° blazed grating writing system was non-trivial and faced several engineering challenges during fabrication. These challenges came up due to the complex design of the interferometer, prism system, and water. This section discusses a detailed investigation and efforts to address all these engineering challenges.

- Bubble formation: The fabrication results were very inconsistent, and we observed bubble formation in the water layer between the prism and chip several times.
- Vacuum chuck: The vacuum chuck to hold the planar chip was not ideal for the current fabrication system, and we faced the issue of water running off during sample translation back and forth.
- Prism aberration: On the alignment camera, we experienced an aberration in the UV spots through the prism.
- Interferometer board arrangement: The current design of the interferometer board uses five 45° reflecting mirrors. The reflecting mirrors were poorly optimised for the required angles, and we experienced tremendous power loss at the surface of the chip. Additionally, it was challenging to focus both arms of the interferometer within the same focal length.

5.7.1 Bubble formation

A series of experiments were conducted to investigate the origin of the bubble formation (shown in Fig. 5.10), and identified causes were the use of high average power, the presence of seed bubbles and localised defects or dirt on the surface. We will discuss these in detail.

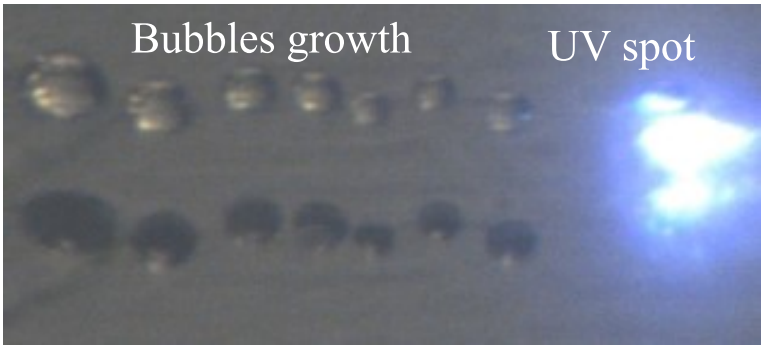

FIGURE 5.10: Photograph of bubble formation inside the water layer between the prism and silica chip upon high-intensity UV exposure.

5.7.1.1 High average power

We found that bubbles formed mainly due to localised heating caused by high UV power densities during the experiments.

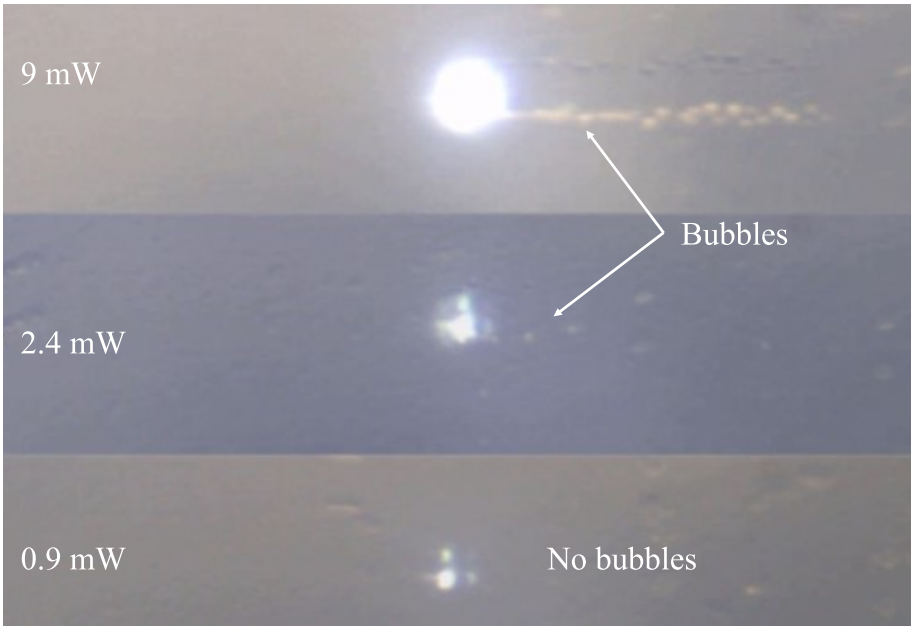

FIGURE 5.11: Photograph of bubble generation by the UV laser writing spot. Reducing the laser power (while keeping the radiative fluence constant) eliminates the formation of bubbles during the writing.

However, the bubble size and density vary depending on the total energy deposited in a focal volume. Figure 5.11 shows three photographs of the focused UV spot scanning

along the FHD sample through a prism and a 100-micron thick water layer. The writing power of the 213 nm laser was gradually reduced from 9 mW to 0.9 mW to probe the formation of the bubbles. The maximum density of bubbles was observed with 9 mW of power, while 2.4 mW introduced few bubbles, and no bubbles were observed when using 0.9 mW of power.

5.7.1.2 Presence of seed bubble

In addition to the laser power, seed bubbles at the site initiate nucleation upon laser exposure. This may be due to the trapped gases inside the water, which start to evaporate upon high-intensity laser exposure and create more bubbles in the water layer. Figure 5.12 shows UV spots scanning over the FHD sample in the left direction. A seed bubble already exists in the water layer without UV exposure. As the UV spots pass through the seed bubble, more bubbles are created along the laser scanning. To investigate further, UV laser exposure was probed in tap, ultra-pure, and outgassed ultra-pure water. Our observation indicates that tap water generates significantly more bubbles than ultra-pure (de-ionized) water under UV exposure, implying that impurities in tap water absorb more laser power, resulting in water boiling. The formation of bubbles was further reduced by out-gassing the ultra-pure water using a rotary pump for 15 minutes.

5.7.1.3 Dirt or defects on the surface

It was observed that an unclean surface of either a prism or FHD sample causes more bubbles due to dust particles or other defects on the surface absorbing more UV light, thereby reducing the threshold power to nucleate bubbles in the water layer. To overcome this issue, cleaning the prism and FHD samples with solvents (acetone and methanol) followed by washing with ultra-pure water was found to be effective.

Through detailed investigations, we observed that the formation of bubbles in the water layer was jointly contributed by laser power, surface contamination of the sample, and trapped gases. We discovered that bubble formation could be minimised by using outgassed ultra-pure water, carefully cleaning the sample with acetone and water, and using low average power.

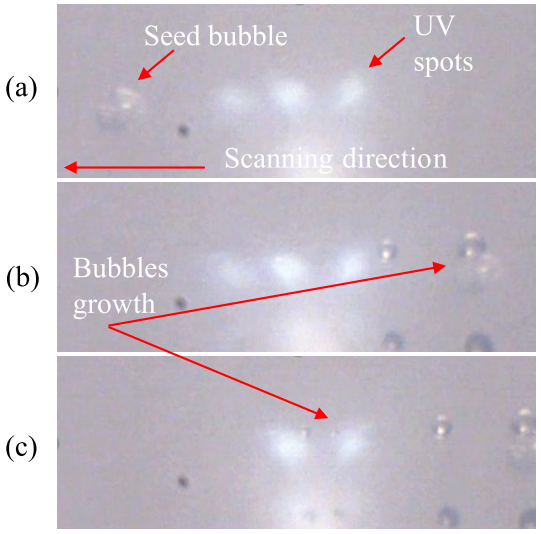

FIGURE 5.12: A Photographic view of bubble nucleation inside the water layer upon UV exposure. (a) Photograph of a seed bubble which exists inside the water layer before the UV spots hit the site. (b and c) Nucleation of bubbles upon UV interaction with the seed bubble.

5.7.2 Vacuum chuck

Initially, we used a dropper to put water on the planar sample mounted on a vacuum chuck. During the initial fabrication tests, we found that the design of the vacuum chuck (see Fig. 5.13) was not ideal for this complex fabrication system. With UV writing potentially taking several hours, continuous evaporation left no water between the prism and the chip. In order to address this issue, Glenn Churchill and Dr James Field designed a new vacuum mount via machining to hold sufficient water for several hours. Figure 5.14(a) shows the newly designed vacuum mount, while the photograph of this mount with UV interferometer is shown in Figure 5.14(b). The novelty of this vacuum mount was that it had o-rings to provide a water-tight seal, so we could flood the planar sample while still using the vacuum to hold the sample.

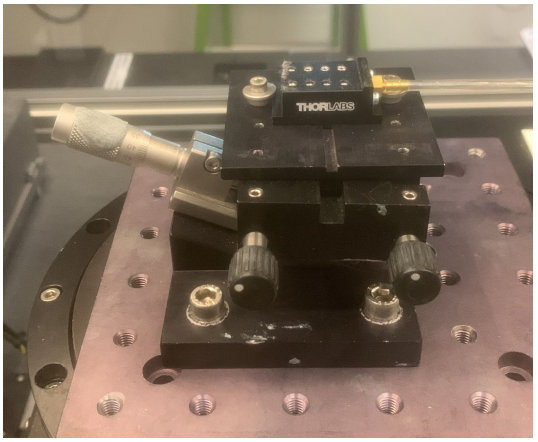

FIGURE 5.13: Photograph of a vacuum chuck to hold a planar sample for UV fabrication.

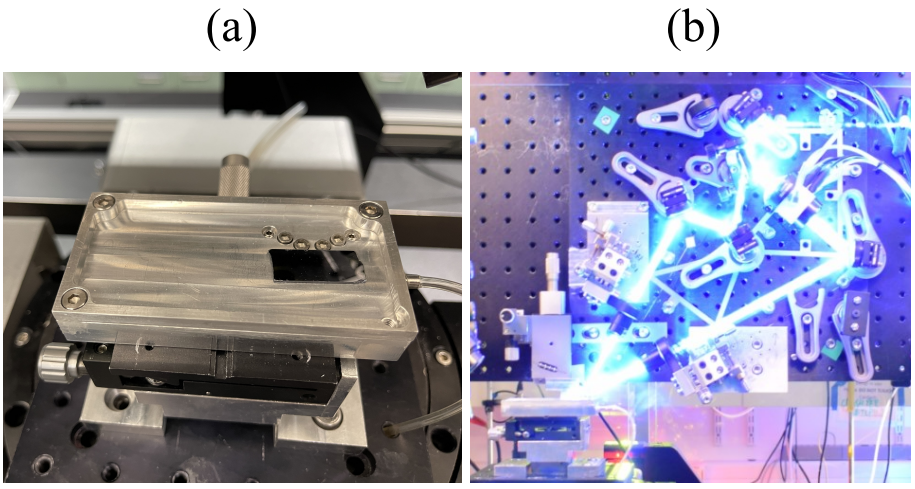

FIGURE 5.14: Photograph of newly designed vacuum mount to hold the FHD deposited chips with sufficient water around.

5.7.3 Prism aberration

The propagation of UV through the prism caused aberration (shown in Fig. 5.15 (a)); we were concerned that this reduced the purity of the interference pattern, resulting in low grating visibility.

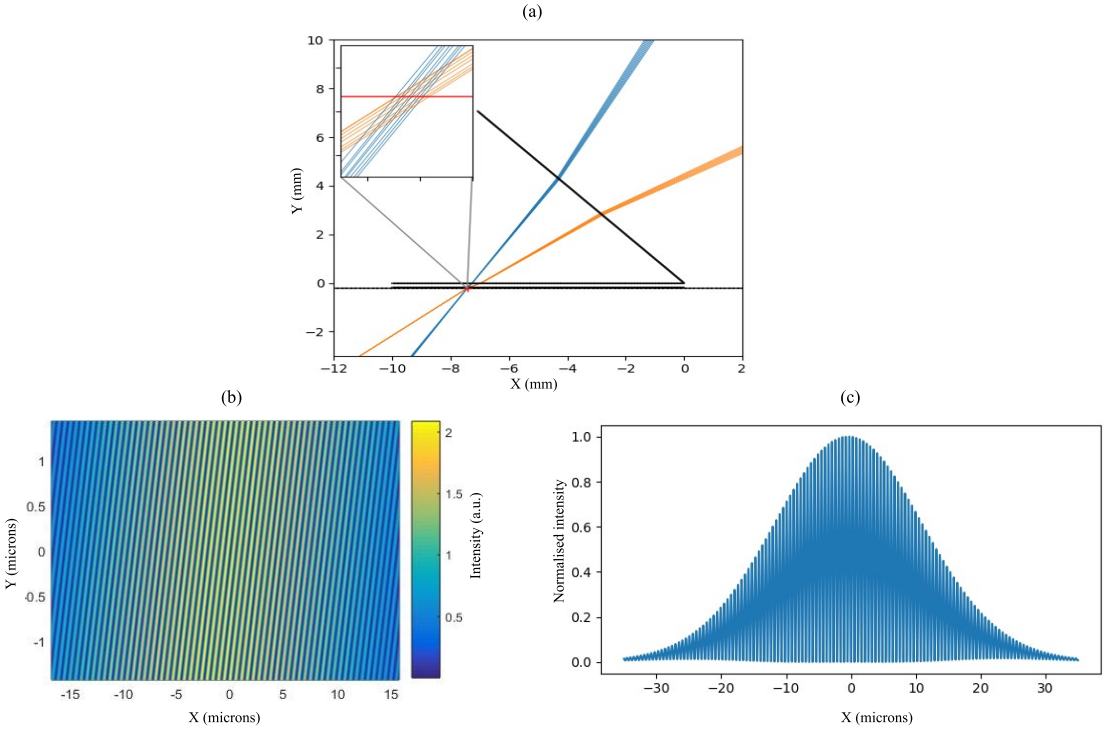

FIGURE 5.15: (a) Ray model of beams focusing through the prism to calculate focal positions. Beam propagation model of interference pattern caused by overlapping focused beams. (b) 1D slice of interference pattern through the focal plane. The scaling of the plot is not one-to-one; hence interference fringes are not 45°. (c) 2D intensity map near the focal plane. The fringe period is constant across the spot, and the spot profile is almost exactly Gaussian, showing negligible aberrations.

Dong-Woo and James Field performed ray modelling to observe interference patterns through the prism. The result showed that the interference pattern was clean (see Fig. 5.15 (b and c)) and remained strong even if the position of UV spots moved across the prism surface. In order to obtain aberration-free UV spots on the alignment camera, we used a UV-glued double-prism system (see Fig. 5.16) to remove the imaging aberration. These modifications greatly simplified the alignment process, allowing us to get consistent fabrication results and move to a larger fabrication areas.

FIGURE 5.16: UV-glued double prism system to overcome the imaging aberration of the UV spots. Prism 1 is used to sit over the sample, with a ∼ 100-micron thick water layer in the middle of sample surface and the prism. The UV beams pass through prism 1 and interfere within the core layer of silica sample. Prism 2 is specifically used to compensate the aberration of UV spots through the alignment camera.

5.7.4 Designing a new UV interferometer board

In previous experiments, the alignment of two spots was found challenging, leading to inconsistent results. Considering the efficiencies of blazed gratings, it is crucial to have a correct blaze angle and period; a slight deviation could lead to a decrease in the efficiency of the grating. In order to ensure consistent fabrication, an entirely new interferometric board was designed. Compared to the previous design, the position of the interferometer components was 3D printed in the new design. Additionally, the use of two focusing lenses made alignment much more effortless. We used a pair of CaF_2 lenses of 80 mm focal length to focus the laser spot at a $1/e^2$ diameter of 7.6 microns. Figure 5.17 shows

the schematic and a photograph of the 213 nm UV writing setup for defining 45° blazed gratings.

5.8 Fabrication of 1D out-of-plane grating coupler

We used the PX 194 wafer in previous experiments to fabricate out-of-plane, 45° blazed grating couplers.

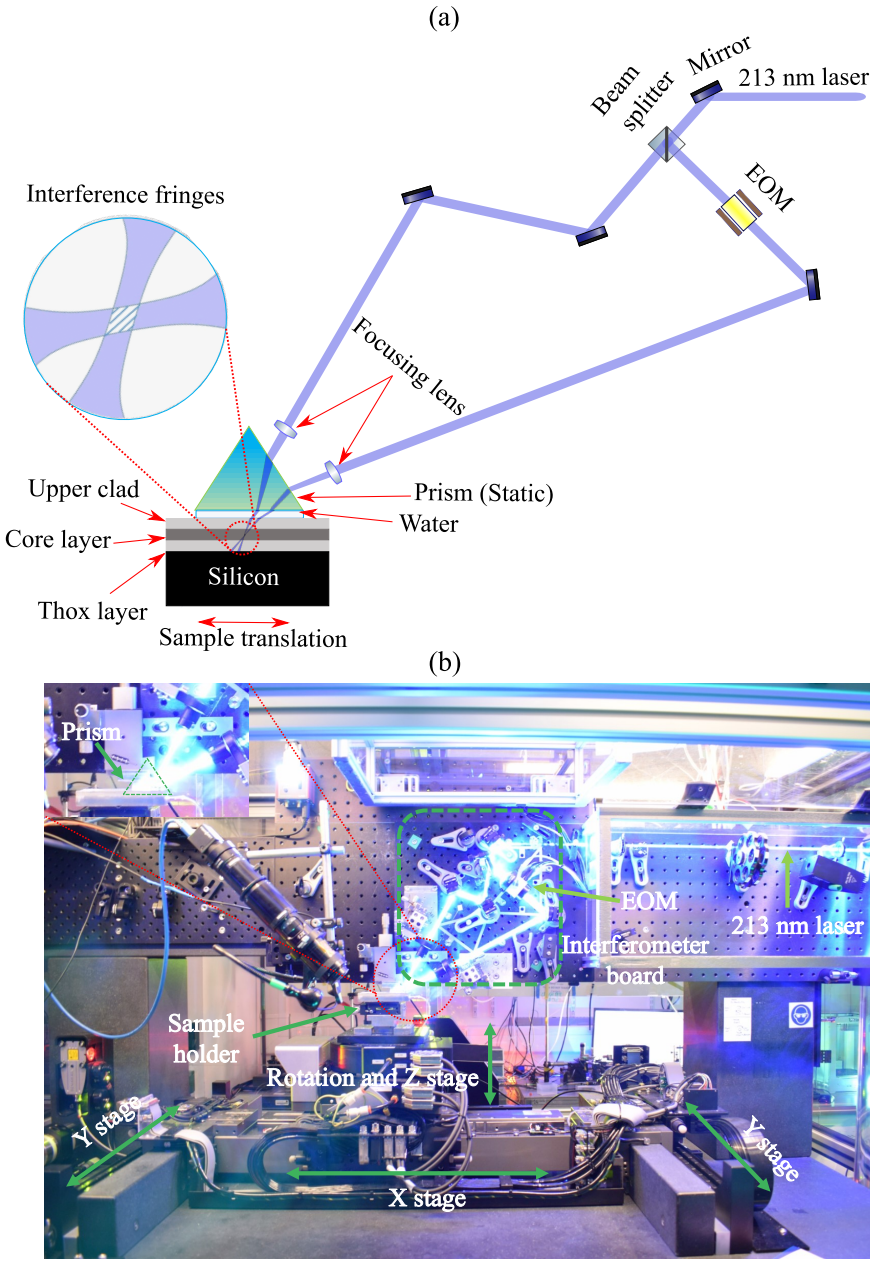

FIGURE 5.17: (a) Schematic of direct 213 nm writing system to inscribe out-of-plane 45° blazed gratings using a 213 nm light. (b) The photographic view of 45° blazed gratings writing setup.

While this wafer was explicitly designed with the core thickness of 3.3 µm for single-mode operation at 780 nm wavelength, the achieved grating strength was weak. Therefore, PX 57 wafer was selected; while this was not single-mode for 780 nm operation, we found it resulted in strong gratings, which should result in better out-of-plane gratings. This wafer had a 4.5 µm thick core layer of germanium and boron-doped silica onto a silicon wafer with a 15 µm thermal oxide acting as an underclad. This core layer was capped with an index-matched 16.2 µm thick boron and phosphorous-doped upper-clad layer, also produced by FHD. The main difference between the core recipes of these wafers was the number of passes used to vary the thickness during deposition. The complete details of deposition recipes for all the used wafers are provided in Appendix 1. We diced the wafer into 20×10 mm chips and loaded them into a hydrogen cell for five days.

We imaged through the double-prism system with the newly developed interferometer and observed aberration-free and circular UV spots. Additionally, the new vacuum mount was robust to store sufficient water for several hours of fabrication. We first aimed to fabricate channel waveguides, including 45° blazed gratings (1D out-of-plane grating coupler) at a period of ∼530 nm to couple 780 nm light out of the chip, normal to the surface. The gratings with a uniform and Gaussian apodisation were inscribed by controlling the phase modulation. Additionally, we used a linear approximation approach [6] to change the grating period for a fixed grating length. The grating period was varied by controlling the phase modulation to focus light 5 mm above the surface of the chip.

5.8.1 Characterisation

Figure 5.18(a) shows the characterisation setup for fabricated devices containing 45° blazed gratings. The characterisation equipment includes stages to mount the fabricated chip aligned with the V-groove assembly. A 50 mm plano-convex lens was placed within a cage assembly to project an image of the outcoupled beam with a magnification of 2 onto a camera. We characterised the fabricated devices by launching 780 nm light into the channel waveguides using a fibre V-groove assembly, a photo of scattered light is shown in Figure 5.18(b). Figure 5.19(a) demonstrates the out-of-plane coupling of 780 nm light from three uniform gratings inscribed at different periods. The free-space beam was characterised (see Figure 5.19(b)) by an Ophir Spiricon beam profiling camera (model L11059), normal to the top surface of the chip. The maximum coupling efficiency for a 3 mm long uniform grating was ∼4%.

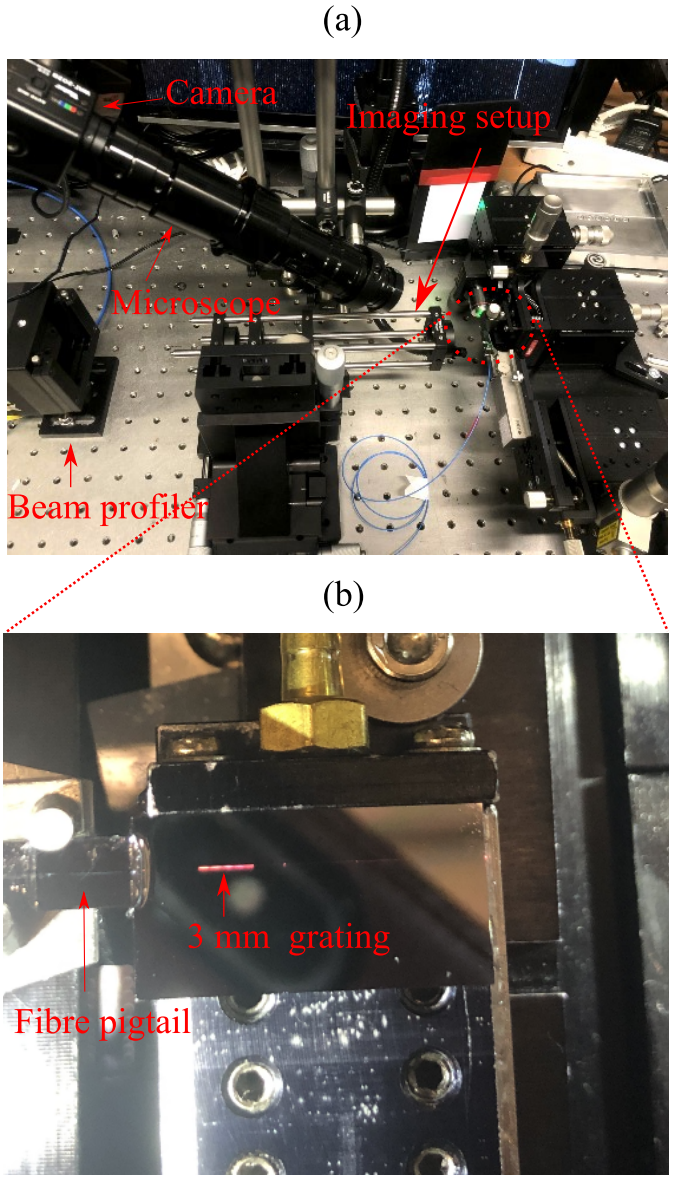

FIGURE 5.18: (a) Characterisation setup for out-of-plane gratings. Chips are side mounted and waveguides coupled into using a fibre v-groove. Light coupled out of the top surface of the chip was interrogated using a horizontally mounted imaging system. (b) Photographic view of a 1D grating coupler. The figure shows vertical outcoupling of 780 nm light from a 3 mm long uniform grating written at a 45° blaze angle.

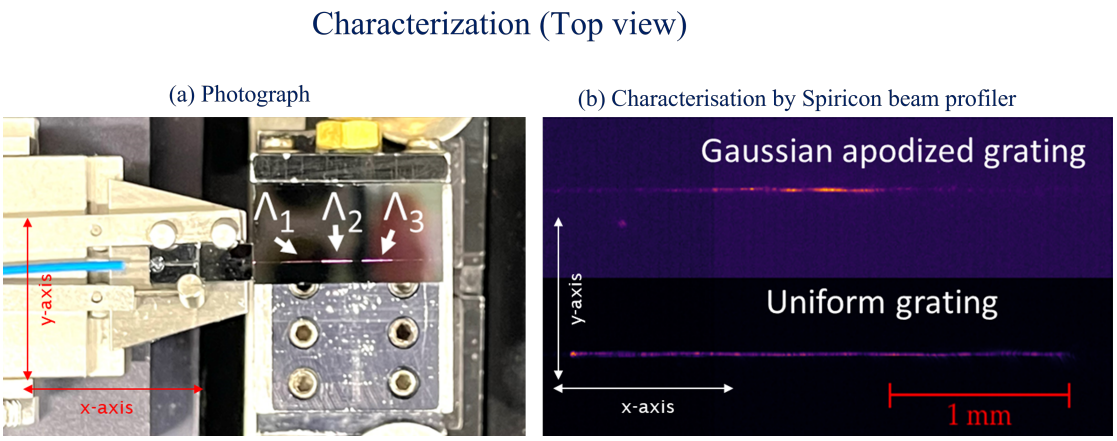

FIGURE 5.19: (a) Photograph of the fabricated chip demonstrates the out-coupling of 780 nm light from three 3-mm long uniform-apodised blazed gratings holographically written with different grating periods. (b) Closer image of the 780 nm light coupling-out of a single 3-mm long grating. The image was taken using a Spiricon beam profiler.

Figure 5.19(a) is a photograph of the fabricated chip demonstrating the out-coupling of 780 nm light from three 3-mm long uniform-apodised blazed gratings holographically written with different grating periods. Figure 5.19(b) shows characterised beams from a 3-mm long uniform and Gaussian apodised grating. The fabricated waveguides were multi-mode in both the x and y-direction. To characterise the chirped gratings, we first brought the surface of the chip into focus. We then moved the camera and lens together (see Fig. 5.20) in 100-micron increments until they were positioned 10 mm above the surface.

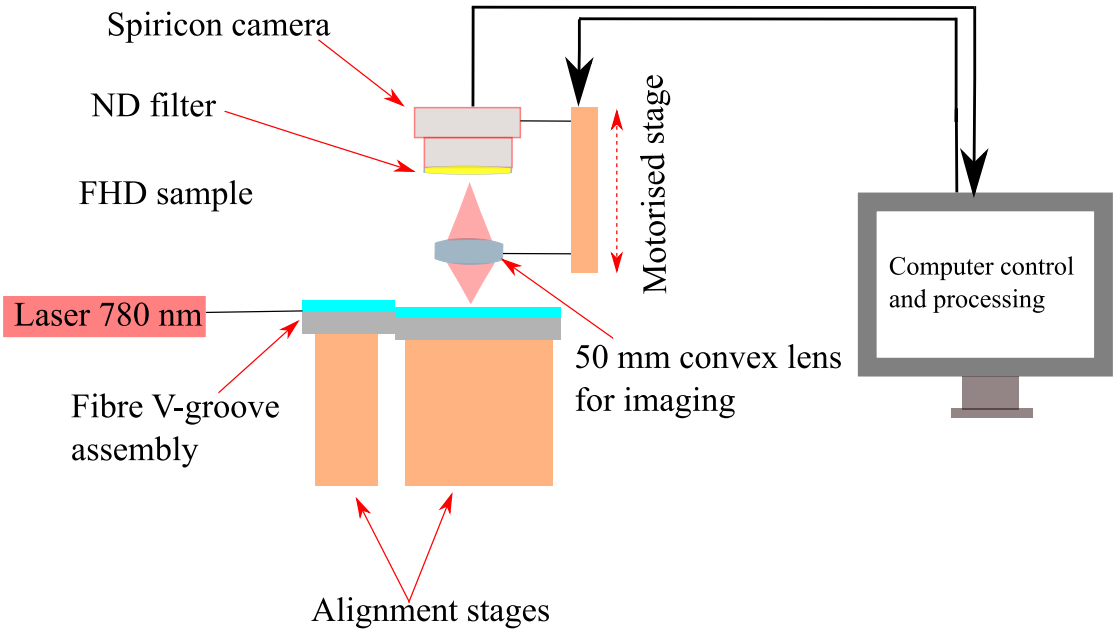

FIGURE 5.20: Schematic of the characterisation of focusing out-of-plane gratings.

Figure 5.21(a) shows a schematic diagram of the beam focusing above the surface of a blazed chirp grating. Figure 5.21(b) shows the characterised data in a digitally processed image of light focusing (in the x-direction) from 2-mm long chirped grating. The

characterised image shows the focusing beam's non-uniform nature, probably due to the chirp profile of the grating. Additionally, the modal beating effects introduce fringes as the used wafer was poorly optimised for 780 nm operation. The focused beam waist appears to be $\sim$ 5 microns with a focal length of $\sim$ 4.8 mm. Based on calculations, the focused spot diameter of a 2 mm wide beam should be 2.4 microns. However, the experimentally measured beam waist is two times higher than the calculated value due to the non-uniform profile of the gratings. Figure 5.21(c) shows the beam propagation from the same grating in the y-direction; the beam diffracted as expected from a 7-micron wide channel waveguide.

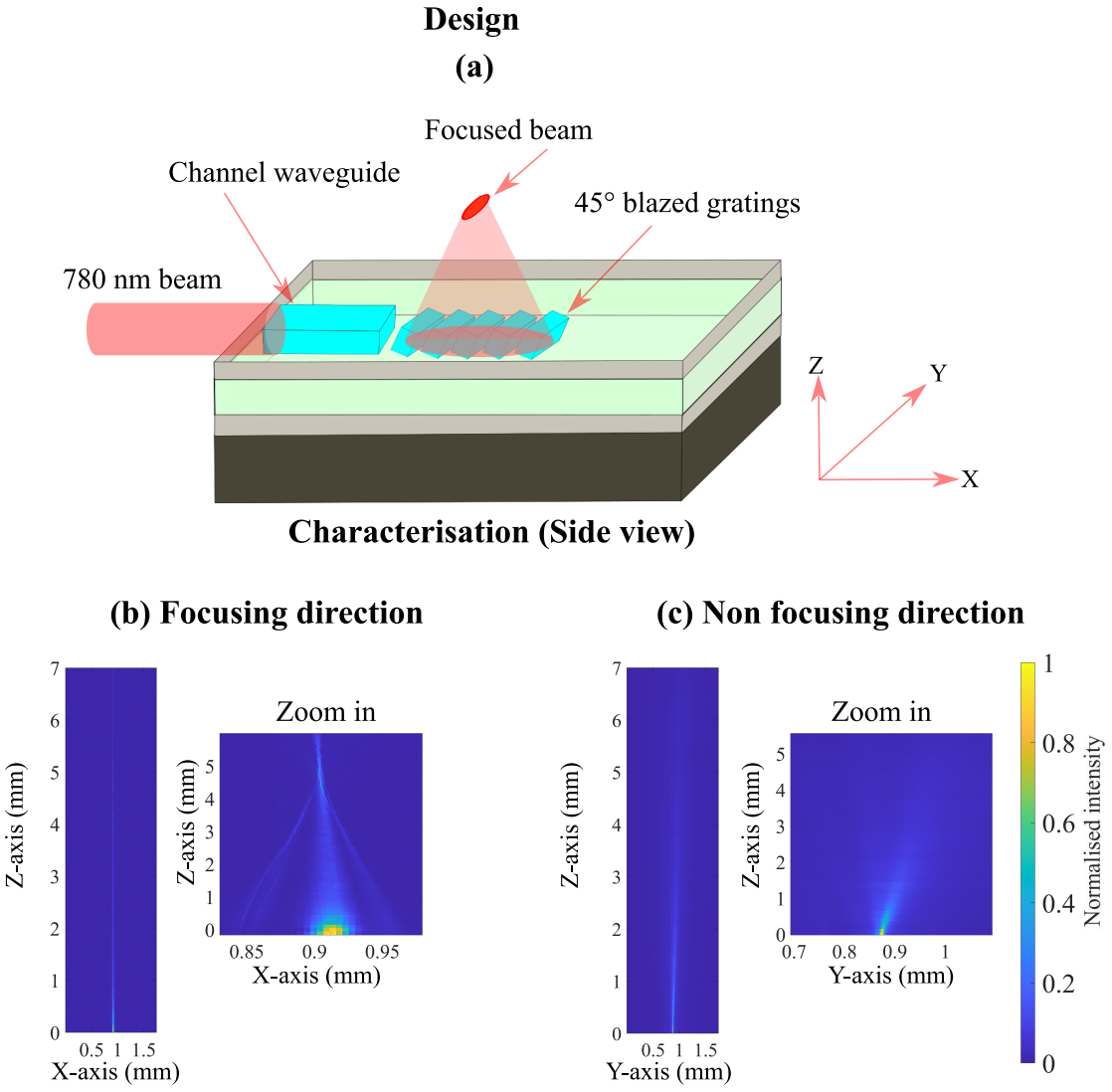

FIGURE 5.21: (a) A schematic of a 1D grating coupler shows an out-of-plane beam focusing from a chirped blazed grating. (b) Characterised image of light focusing out of the chip in the x-direction from a 2-mm chirped blazed grating. (c) Characterised image of the light diffracting from the same grating in the y-direction.

5.9 2D grating coupler

In this section, we will extend the design of an out-of-plane grating coupler to 2D. The design presented in Fig. 1.2 requires a beam expander to change the mode coupled from a 6 µm fibre core to a 10 mm wider beam. Possible solutions could be tapered mode expanders or diffractive grating couplers. Traditionally beam expanders/waveguide tapers adiabatically change the waveguide mode shape to achieve a constant deformation of the waveguide mode from an entrance to an exit mode. Typically these are used in silicon, high-index waveguide schemes to create grating couplers for optical fibre input. In order to expand the input mode from a 6 µm fibre core to a 10 mm wider beam, a large tapered waveguide would be needed, which is not ideal for a compact integrated platform. An alternative approach could be diffractive grating couplers. For example, Kim *et al.* [14] have demonstrated an integrated design for a SiN grating coupler to provide a free space beam coupling out of the plane. Their design consists of an extreme mode converter providing the interface with the photonic mode in the waveguide and the free space beam (see Fig. 1.3 taken from [14]). In the first step, a mode expander was fabricated to convert the channel waveguide mode to slab mode via evanescent coupling. In the second step, large grating lines with an apodisation profile were fabricated to couple the slab mode into a free-space collimated beam, as shown in the figure. The mode profiling showed a Gaussian beam with a beam waist of 160 µm in both x- and y-axis coupled out of the device into free space. The same research group has presented a modified scheme [15] where silicon metasurfaces were used on the top of the etched grating footprint to focus light at 475 nm spot size. For a detailed study on 2D grating couplers, we kindly refer the reader to Chapter 1.

5.9.1 Proposed scheme for a 2D grating coupler

Our approach will use in-plane grating couplers to provide an expanded beam.

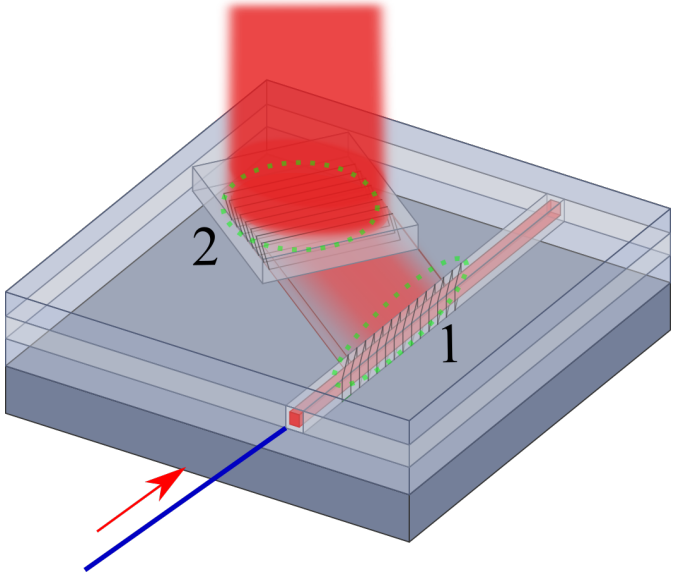

FIGURE 5.22: Proposed scheme using an in-plane blazed Bragg grating (1) to input light into a large-area out-of-plane (OOP) blazed grating (2). These two parts are fabricated separately.

The obvious geometry would be an in-plane 10 mm 45° blazed Bragg grating in a planar waveguide could generate a 10 mm wide beam to input into a 10 mm × 10 mm out-of-plane area grating. However, this scheme will not work, as gratings at 45° are inherently polarising; any light diffracted from the first grating would be in the wrong polarisation to interact with the orthogonal out-of-plane gratings.

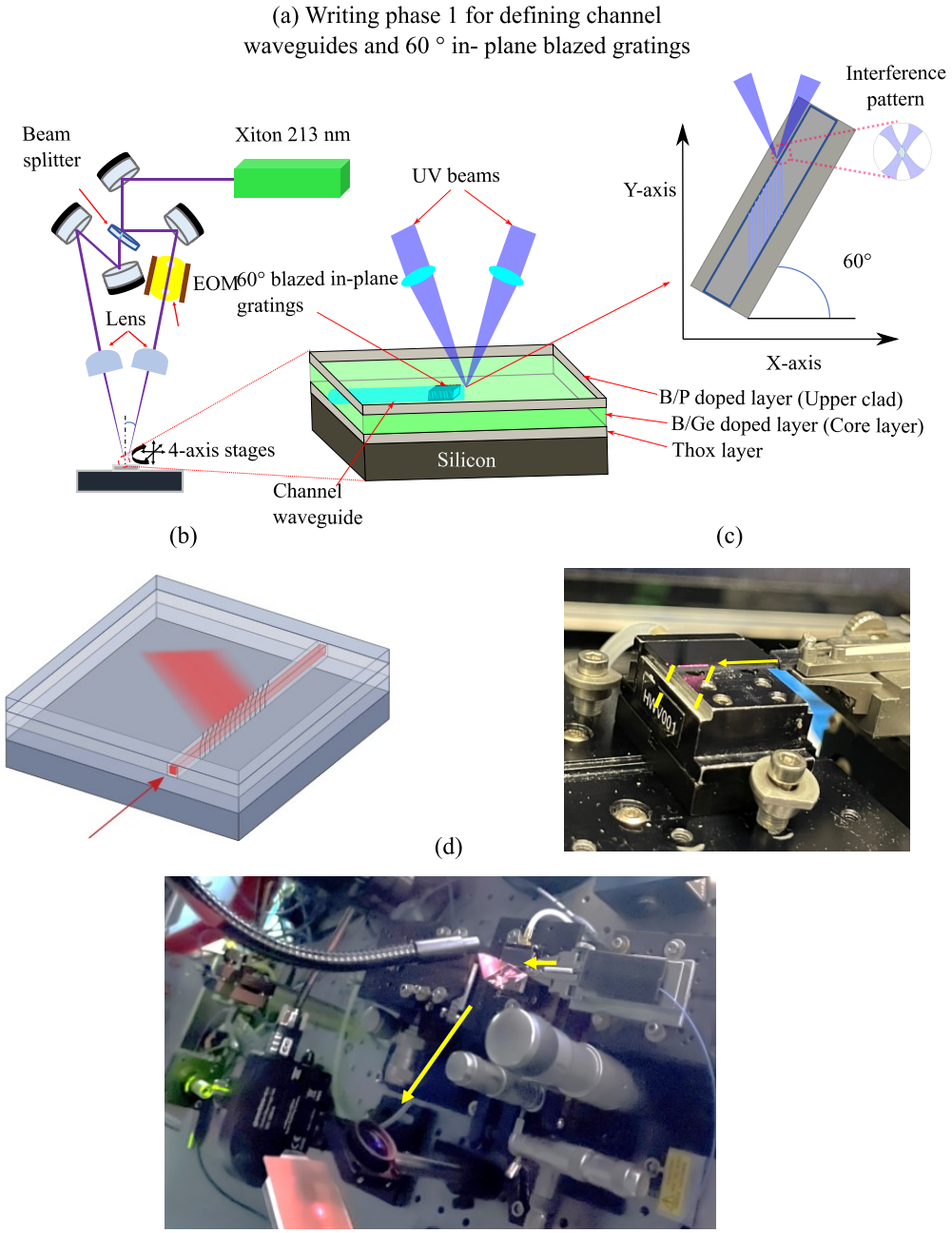

FIGURE 5.23: (a) The schematic of the first writing phase displays the same interferometric board discussed in chapters 3 and 4. However, the writing approach uses stage rotation to inscribe in-plane 60° blazed gratings in a channel waveguide. (b) The schematic of 60° blazed grating. With a 60° blaze angle, the period matches 780 nm wavelength and reflects the incoming mode at 120° within the core layer. (c) Photograph of the fabricated chip with 60° blazed grating. (d) Characterisation of blazed gratings to measure the reflected power and efficiency of the device using a prism and plano-convex lens.

Possible solutions exist for generating a large beam with in-plane diffraction gratings with blaze angles $< 45°$ and $> 45°$(i.e. 60° to 70°). The proposed design of a 2D grating coupler consisted of two fabrication phases. Phase 1 was to inscribe a channel waveguide with in-plane blazed gratings in a hydrogen-loaded FHD chip. Later, the fabricated sample was re-hydrogen-loaded, followed by the second phase to fabricate out-of-plane grating planes. Figure 5.22 shows the design of a 2D grating coupler developed in two writing phases.

5.9.2 Fabrication and characterisation of 60° blazed gratings

In the first phase, a channel waveguide is fabricated containing a 6 mm long in-plane 60° blazed gratings at a laser fluence of 1.5 kJ cm^{-2}. We used the same interferometric board previously employed for 1550 nm Bragg gratings. A 60° blaze angle was obtained by rotating the stages, as shown in Fig. 5.23(a). An additional waveguide was fabricated at the same fluence to measure the efficiency of the blazed grating. Further details of the fabrication technique are available in [6]. Figure 5.23(b) shows the schematic of the channel waveguide and 60° blazed gratings to provide a wider beam within the core layer. Figure 5.23(c and d) shows photographs of a fabricated chip on the characterisation setup. The chip is coupled to a fibre V-groove assembly to launch a 780 nm source in the waveguide. We carefully measured the transmission losses through the waveguide with and without gratings and compared it to the reflecting power of 60° blazed grating. The coupling efficiency after compensating the Fresnel losses through prism came out to be 18%.

5.9.3 Fabrication of a 2D out-of-plane grating coupler

Prior to the second writing phase, the chip was again hydrogen-loaded. The fabrication of mm scale grating planes using a 7.6-micron UV spot was not ideal. Therefore we replaced the 80 mm spherical plano-convex lenses with 100 mm cylindrical lenses in the out-of-plane interferometric board. The cylindrical lens focuses the beam to 8.2 µm in one axis, providing a 2.50 mm diameter on the wider axis.

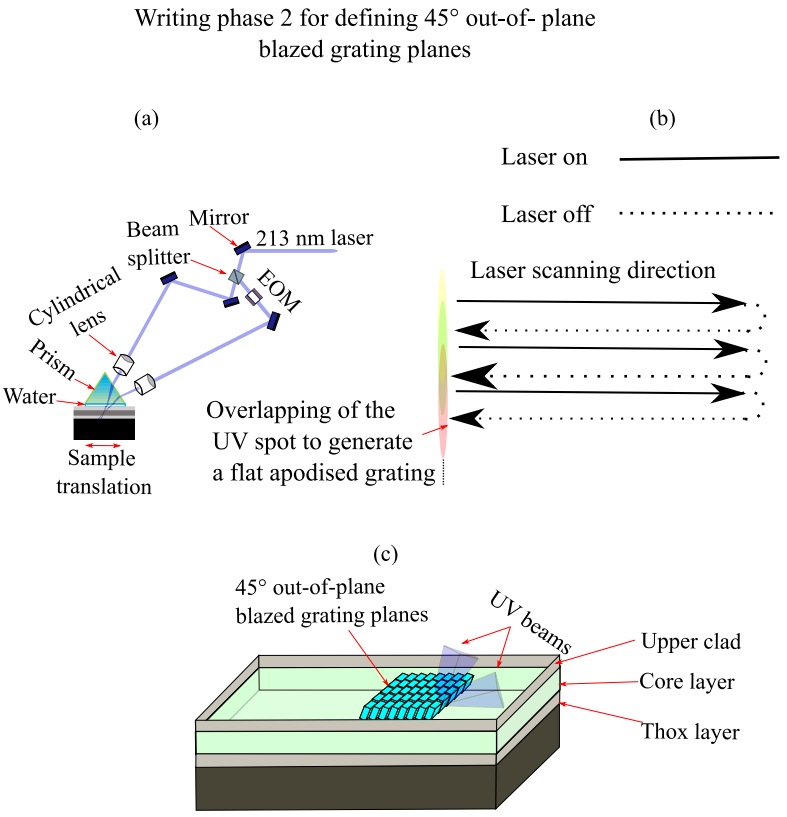

FIGURE 5.24: (a) The schematic of the second writing phase shows a 45° blazed grating writing interferometer with cylindrical lenses to inscribe out-of-plane 45° blazed grating planes. (b) Demonstration of writing scheme; the direction of laser scanning was across the horizontal axis. (c) Schematic demonstration of 45° area grating planes.

The schematic of the out-of-plane interferometric board is shown in Fig. 5.24(a). The out-of-plane grating planes were fabricated at a fluence of 1.47 kJ cm^{-2}. The writing direction was horizontal, where laser scans over to generate a waveguide and gratings. UV spot overlapping was performed vertically in an attempt to generate a flat apodised grating (see Fig. 5.24(b)). Figure 5.24(c) shows the schematic of 45° blazed grating planes over a large area. Figure 5.25 (a) shows the schematic of a 2D out-of-plane grating coupler. Figure 5.25(b) shows the photograph of the fabricated 2D grating coupler mounted on the characterisation setup. We used a fibre V-groove assembly to launch 780 nm light inside the waveguide containing 60° blazed gratings.

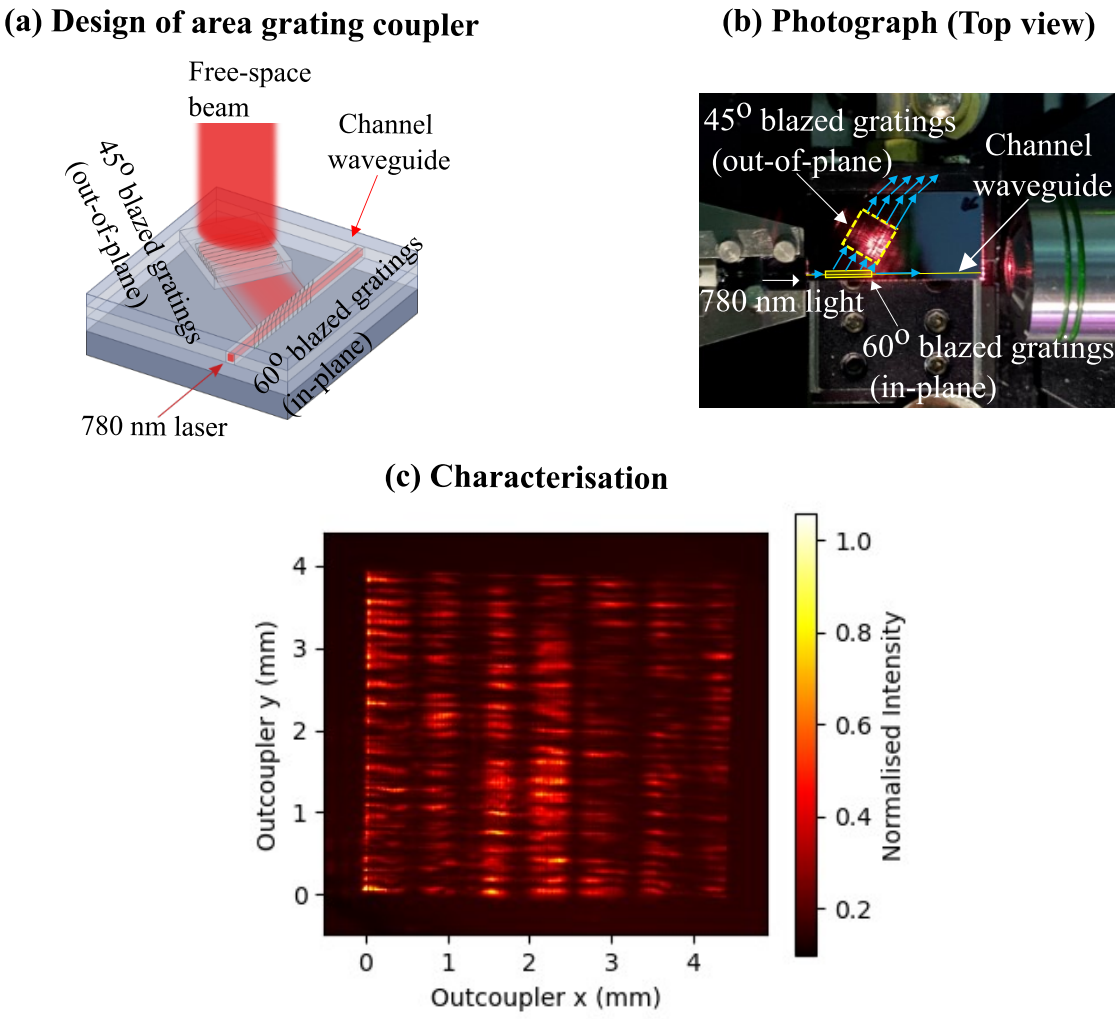

FIGURE 5.25: (a) The schematic shows a 2D grating coupler which follows the fabrication in two phases using 213 nm light. The design contains in-plane 60° blazed gratings in a channel waveguide, followed by out-of-plane grating planes to provide a large beam into free space. (b) The photograph of a silica-on-silicon chip characterisation. The figure shows the chip aligned with a fibre V-groove assembly to launch 780 nm light into a channel waveguide containing 60° blazed in-plane gratings. The in-plane gratings provide beam expansion inside the planar core layer. The wide beam finally reflects into free space by out-of-plane 45° blazed grating planes. (c) The figure shows the characterised image of the outcoupled beam into free space. The input light propagates in a positive y-direction and shows fringes due to modal beating.

The in-plane grating coupler expanded the input beam within the planar layer. The wider beam is reflected towards grating structures (4.4 mm × 3.9 mm) written at a 45° blaze angle and coupled into free space. Later, the characterisation was performed by the Spiricon beam profiler. Figure 5.25 (c) shows the characterised image of an outcoupled beam. The characterisation shows horizontal fringes in the image which we believe is due to a modal beating. The vertical fringes correspond to the overwriting of the cylindrical UV spot along a wider axis. We measured the coupling efficiency by taking the ratio of the measured laser power out of fibre to the power in free space. The coupling efficiency (fibre to free space) of this device was less than 1%, as it was the first

device and a lot of work is required to make large and efficient devices by improving the grating strength and ensuring the 45° blaze angle (see Chapter 6).

5.10 Conclusions and future work

This chapter presents a state-of-the-art holographic system to fabricate gratings couplers for integrated out-of-plane beam delivery. Using a prism coupling approach, we developed a new interferometer to inscribe out-of-plane 45 ° blazed gratings in a silica-on-silicon platform. The chapter encompassed detailed efforts to overcome the engineering challenges due to the complex design of the fabrication system. Based on analytical and numerical modelling, we made several improvements in the design of the holographic fabrication system to minimise errors in the blaze angle and grating period. A characterisation system was established to characterise the light coupling out-of-plane into free space. Using 45 ° blazed grating approach, we fabricated a 1D out-of-plane grating coupler with a uniform and Gaussian apodised profile. The maximum coupling efficiency of a 1D grating coupler was achieved up to ∼1.3%/mm. We also demonstrated a focusing grating coupler by introducing a chirp profile to the gratings. Chirp gratings were characterised by taking several height scans by beam gauge using a computer-controlled translation stage. Results showed the beam focusing at ∼4.8 mm above the surface.

After getting consistent fabrication results of 1D grating couplers, we proposed a 2D design for integrated out-of-plane beam delivery. The design consisted of two writing phases using two different interferometer boards. Before each fabrication, the planar sample was put into a hydrogen cell for five days. In the first phase, we used a 1550 nm interferometer board and fabricated a channel waveguide containing a 6 mm long in-plane 60 ° blazed gratings at a fluence of 1.5 kJ cm^{-2}. The in-plane 60 ° angle was set through the rotation of Aerotech stages. The in-plane blazed grating served as a beam expander to diffract a wider beam within the core layer. The coupling of in-plane blazed gratings showed efficiencies up to 18 %. In the second writing phase, we aimed for large-area fabrication; we replaced the spherical plano-convex lenses with a pair of cylindrical lenses in the setup shown in Fig. 5.24. The out-of-plane grating planes were fabricated at a fluence of 1.47 kJ cm^{-2}. The results successfully demonstrated a large-area(4.4 mm × 3.9 mm) grating coupler. The fibre-to-free space coupling efficiency was less than 1%. The coupling efficiency of the fabricated devices was lower than our expectations, inferred by numerical and analytic modelling as the modelling approach assumed the highest achieved modulated refractive index (Δn_{ac}) of to 1.25×10^{-3}. Achieving such a high index contrast for gratings is challenging as overlapping two spots was tricky with a complex interferometer arrangement using a prism and water. The blaze angle and grating period are crucial in determining coupling efficiency, and a slight angular deviation of beams significantly reduces the coupling efficiency.

Future work will be followed with several engineering improvements, such as mounting a 45 ° pinhole in the interferometer arrangement to ensure a correct blaze angle. New recipes for wafer deposition will be investigated with higher germanium concentration to get strong gratings. We expect to push the coupling efficiency to 20 % for a 2D area (10 mm × 10 mm) out-of-plane grating coupler. Once such a device has been made, the prototypes will be ready to provide a large free space beam for deployable quantum atom traps.

A part of this work is published in 'Optics Express'[9] and conference proceedings in [16]–[18]. Additionally, two journal papers are currently being drafted.

5.11 References

[1] T. Erdogan, "Fiber grating spectra," *Journal of lightwave Technology*, vol. 15, no. 8, pp. 1277–1294, 1997.

[2] G. Meltz, W. Morey, and W. Glenn, "In-fiber Bragg grating tap," in *Optical Fiber Communication Conference*, Optica Publishing Group, 1990, TUG1.

[3] G. Meltz, W. W. Morey, and A. L. Wilson, *Optical waveguide embedded light redirecting and focusing Bragg grating arrangement*, US Patent 5,061,032, Oct. 1991.

[4] K. Zhou, G. Simpson, X. Chen, L. Zhang, and I. Bennion, "High extinction ratio in-fiber polarizers based on 45 tilted fiber Bragg gratings," *Optics Letters*, vol. 30, no. 11, pp. 1285–1287, 2005.

[5] M. T. Posner, N. Podoliak, D. H. Smith, P. L. Mennea, P. Horak, C. B. E. Gawith, P. G. R. Smith, and J. C. Gates, "Integrated polarizer based on 45° tilted gratings," *Optics express*, vol. 27, no. 8, pp. 11 174–11 181, 2019.

[6] J. W. Field, S. A. Berry, R. H. Bannerman, D. H. Smith, C. B. Gawith, P. G. R. Smith, and J. C. Gates, "Highly-chirped Bragg gratings for integrated silica spectrometers," *Optics Express*, vol. 28, no. 14, pp. 21 247–21 259, 2020.

[7] K. Byron, K. Sugden, T. Bricheno, and I. Bennion, "Fabrication of chirped Bragg gratings in photosensitive fibre," *Electronics letters*, vol. 18, no. 29, pp. 1659–1660, 1993.

[8] K. Sugden, I. Bennion, A. Molony, and N. Copner, "Chirped gratings produced in photosensitive optical fibres by fibre deformation during exposure," *Electronics letters*, vol. 30, no. 5, pp. 440–442, 1994.

[9] D.-W. Ko, Q. S. Ahmed, J. Field, J. C. Gates, and P. Horak, "Out-of-plane beam shaping with UV-written tilted Bragg gratings for beam delivery on quantum chips," *Optics Express*, 2022.

[10] S. M. Schultz, T. K. Gaylord, E. N. Glytsis, and N. F. Hartman, *Diffractive grating coupler and method*, US Patent 6,285,813, Sep. 2001.

[11] S. M. Schultz, E. N. Glytsis, and T. K. Gaylord, "Design of a high-efficiency volume grating coupler for line focusing," *Applied optics*, vol. 37, no. 12, pp. 2278–2287, 1998.

[12] S. M. Schultz, E. N. Glytsis, and T. K. Gaylord, "Design, fabrication, and performance of preferential-order volume grating waveguide couplers," *Applied Optics*, vol. 39, no. 8, pp. 1223–1232, 2000.

[13] T. S. Francis and X. Yang, *Introduction to optical engineering*. Cambridge University Press, 1997.

[14] S. Kim, D. A. Westly, B. J. Roxworthy, Q. Li, A. Yulaev, K. Srinivasan, and V. A. Aksyuk, "Photonic waveguide to free-space Gaussian beam extreme mode converter," *Light: Science & Applications*, vol. 7, no. 1, pp. 1–13, 2018.

[15] A. Yulaev, W. Zhu, C. Zhang, D. A. Westly, H. J. Lezec, A. Agrawal, and V. Aksyuk, "Metasurface-integrated photonic platform for versatile free-space beam projection with polarization control," *ACS photonics*, vol. 6, no. 11, pp. 2902–2909, 2019.

[16] Q. S. Ahmed, J. W. Field, P. C. Gow, C. Holmes, D.-W. Ko, P. Horak, C. B. E. Gawith, P. G. R. Smith, and J. C. Gates, "Holographically fabricated blazed chirped gratings for out-of-plane integrated beam focusing," in *Bragg Gratings, Photosensitivity and Poling in Glass Waveguides and Materials*, Optica Publishing Group, 2022, BTu1A–7.

[17] Q. S. Ahmed, J. W. Field, P. C. Gow, C. Holmes, D.-W. Ko, P. Horak, C. B. E. Gawith, P. G. R. Smith, and J. C. Gates, "Holographically fabricated blazed gratings for out-of-plane coupling in integrated optics," in *CLEO: Science and Innovations*, Optica Publishing Group, 2022, STh4P–3.

[18] Q. S. Ahmed, J. W. Field, P. C. Gow, C. Holmes, R. H. S. Bannerman, P. L. Mennea, C. B. E. Gawith, P. G. R. Smith, and J. C. Gates, "Holographically fabricated 2d grating coupler for integrated large beam delivery," CLEO/Europe-EQEC, 2023.

Chapter 6

Conclusions and future work

The current project was part of ongoing research activities for the UK Quantum Technology program. The motivation of this project was to fabricate fibre-coupled out-of-plane grating couplers to provide a large free space beam (1 cm) for deployable quantum atom traps. This thesis has provided the initial investigation into blazed gratings fabricated by a pulsed 213 nm laser source. The devices made in this work have dimensions an order of magnitude higher than the previous work reported in Chapter 1. Though the efficiencies of the fabricated devices were low, we aim to enhance these efficiencies significantly to fulfil the requirements of atom trap systems specified in Chapter 1.

Our research group has been working for the last 20 years on fabricating Bragg gratings in fibre and planar silica for various applications using CW 244 nm frequency-doubled Ar-ion lasers. However, one limitation of the 244 nm laser source was the need for hydrogen loading, which limits the writing time to 2 hours; using this source to make large and complex integrated devices was impossible. When I joined the project, our group had already installed a new pulsed laser system operating at 213 nm wavelength. Compared to the 244 nm laser source, the 213 nm laser offers high-quality grating fabrication without hydrogen loading. I aimed to explore this new laser source for grating fabrication. At the start of this thesis, several research questions were raised about the potential of this laser source for large-area grating fabrication and how it operates.

How does a 213 nm laser compare with a 244 nm laser system for planar waveguide and grating fabrication?

Can we write planar Bragg gratings without hydrogen loading using a 213 nm laser? If yes, how do the devices and parameters compare to hydrogen-loaded fabricated devices?

Does a 213 nm source generate non-linearity in photosensitivity or grating response, as previously reported in [1]?

Considering the pulse nature of the 213 nm laser, what is the suitable regime (combination of laser power and fluence) to operate for waveguide and grating fabrication?

Do holographically fabricated blaze gratings diffract enough light to make large out-of-plane grating couplers?

Is the proposed geometry for large-area devices fabricable?

I will provide a summary to answer all these questions in the following sections.

6.1 System calibration and characterisation of 213 nm writing system

Chapter 3 presented extensive system calibration of the 213 nm system to inscribe integrated channel waveguides and Bragg gratings. The waveguides and gratings were fabricated in planar silica, with and without hydrogen loading. The 213 nm laser writing system has similar parameters and resulting device performance compared to conventional 244 nm direct writing systems. However, to obtain the maximum grating strength, the 213 nm laser requires a 3.5 kV peak voltage to EOM, 0.7 kV lower than the voltage needed for grating writing using a CW 244 nm laser.

In addition, this chapter included useful information on the fluence dependence of the grating strength, the effective refractive index of the waveguide, the detuning bandwidth of grating fabrication, and the waveguide propagation losses. Using an intuitive model, we explored that grating strength depletes with increasing fluence before photosensitivity saturation.

Chapter 3 also addressed the challenges of fabricating direct UV-written waveguides and gratings in non-hydrogen-loaded silica samples with 213 nm light, including avoiding the damage threshold of silica from the pulsed laser system and the stability of the interferometer. The experiments demonstrated the successful fabrication of waveguides and high-quality gratings despite the $\sim$ 17 hours of writing time. However, hydrogen loading provides 1.7 times higher Δn_{ac} than non-hydrogen loaded gratings. In general, fabricating waveguides in non-hydrogen-loaded samples is not ideal, but it is relatively suitable for grating inscription since waveguides require much higher fluences than gratings. Compared to the 244 nm laser [2], we observed a 1.3 times higher modulated refractive index (Δn_{ac}) in 213 nm planar Bragg gratings.

This chapter also identified a new fabrication approach, where UV radiative fluence builds up in multiple passes. Results suggested that the photosensitivity and grating strength can be substantially improved using the multi-pass writing technique. Additionally, these experiments showed consistent photosensitivity of devices, indicating the hydrogen out-gassing effect was not substantial for at least 10 hours. This writing technique was crucial for inscribing larger and more complex devices, providing a robust photosensitive platform via pre-exposure, and minimising the artefacts associated with hydrogen out-gassing and the stability of the interferometer.

6.2 Identifying appropriate writing regimes for 213 nm written planar Bragg gratings

Chapter 4 provided a detailed investigation into regimes (power and fluence relationship) of SSDUW using 213 nm light. This chapter discussed the non-typical effects of writing power and fluence on the induced effective change in the refractive index and gratings strength. Compared to [1], [3], we used higher peak intensities (up to 0.58 GW cm^{-2}) to define waveguides and Bragg gratings in doped silica. Contrary to [1], we

have not seen any significant evidence of similar non-linear photosensitivity response in B/Ge silica. However, we observed a subtle non-linearity where gratings and waveguide properties depend on writing power. However, it is challenging to draw comparisons due to the different compositions of glass, the geometry of the planar sample, the effect of doping and hydrogen loading and the lack of a pre-defined waveguide. We observed that 2.5 to 4.6 mW writing powers are ideal for SSDUW, where we suppose the change in the refractive index upon laser exposure was dominated by photochemical changes. In this writing regime, grating strength is maximum at a fluence of 1 kJ cm^{-2}, and the photosensitivity response appears to be optimum, an essential feature to fabricate complex devices. Above powers of 4.6 mW, the data suggests additional refractive index change caused by damage-induced stress, leading to photosensitivity saturation at lower fluences and reduced grating strength. Above 4.6 mW of writing power, the photosensitivity mechanism became complex due to damage and heating. Investigations were performed to explore the origin of laser-induced damage; both optical microscopy and Zescope showed that high writing power leads to localised damage of the silica-silicon interface. Raman spectroscopy was performed to probe the structural modification of damaged silicon. However, no peak corresponding to amorphous silicon was detected, which suggests that the laser-induced damage did not cause substantial deformation to the crystalline structure.

6.3 Fabricability of large area blazed grating couplers

Chapter 4 presented a state-of-the-art holographic system to fabricate gratings couplers for integrated out-of-plane beam delivery. Using a prism coupling approach, I developed a new interferometer to inscribe out-of-plane 45 ° blazed gratings in a silica-on-silicon platform. Based on analytical and numerical modelling, we made several improvements in the design of the holographic fabrication system to minimise errors in the blaze angle and grating period. Using a 45 ° blazed grating approach, we fabricated a 1D out-of-plane grating coupler with a uniform and Gaussian apodised profile. This chapter also presented light focusing using chirped blazed gratings.

After getting consistent fabrication results of 1D grating couplers, we proposed a 2D design for integrated large-area beam delivery. The design consisted of two writing phases using two different interferometer boards. The first writing phase inscribed a 6 mm long in-plane 60 ° blazed gratings to diffract a wider beam into the core layer, and the second phase fabricated out-of-plane 45°grating planes. The fabricated device showed a large-area(4.4 mm × 3.9 mm) free space beam; the beam dimensions are significantly larger than the etched gratings reported in Chapter 1. The fibre-to-free space coupling efficiency was less than 1%. We expect to push the coupling efficiency to 20 % for a 2D area (10 mm × 10 mm) out-of-plane grating coupler.

6.4 Future work

In this thesis, a prototype of a large-area grating coupler is demonstrated. We will modify the interferometer arrangements in future work by introducing a 45° pinhole where two beams interfere, as the correct blaze angle plays a crucial role to determine the coupling efficiencies of blazed gratings. The template of a newly designed interferometer

is shown in Fig. 6.1 The pinhole will be used to align interferometer beams to ensure the interference and inscription of gratings at 45° blaze angle. Secondly, we will investigate and use the multi-pass writing approach for improving the grating strength, hence the coupling efficiencies of blazed gratings.

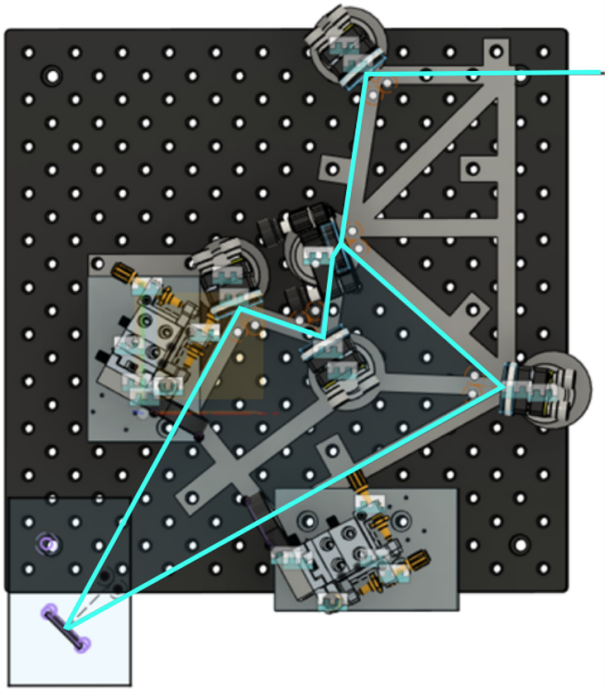

FIGURE 6.1: Newly designed template of the interferometer for fabrication of out-of-plane 45° blaze gratings.

The analytical and numeric modelling suggests that the blaze angle is crucial to determine the coupling efficiencies of the blazed gratings. Additionally, new recipes will be explored for wafer deposition to get higher index contrast gratings for 780 nm operation. The multiple-pass writing technique (discussed in Chapter 3) will be utilised to improve the grating strength for in-plane and out-of-plane gratings. The characterisation will include the measurements of coupling efficiencies and beam divergence. We aim to increase the coupling efficiency of our devices. However, the fundamental limitation is associated with the weak gratings contrast achieved by direct UV writing. Since $1.25\times\ 10^{-3}$ was the highest Δn_{ac} experimentally observed using 213 nm processing (see Chapters 3 and 4), we regarded it as a suitable value to determine the efficiencies of blazed gratings. The coupling efficiency of final device will be quadratic and depend upon both in-plane and out-of-plane blazed gratings. Based on analytic modelling discussed in Chapter 5, we can achieve $\sim$ 50 to 60 % coupling efficiency for a 10 mm beam width (fibre to planar). Similarly, for a 10 mm $\times$ 10 mm out-of-plane grating planes we expect to achieve $\sim$ 60 % coupling efficiency (fibre to free space). The total coupling efficiency of the device will be the percentage coupling power of in-plane blazed grating $\times$ percentage coupling power of out-of-plane blazed gratings $\sim$ 20 to 25 % for a 2D area (10 mm $\times$ 10 mm) out-of-plane grating coupler. If we could increase Δn_{ac}, the efficiencies of both (in-plane and out-of-plane) blazed gratings can be significantly enhanced. Once such a device has been made, the prototypes will be ready to provide a large free space beam for portable quantum atom traps (see Fig. 6.2).

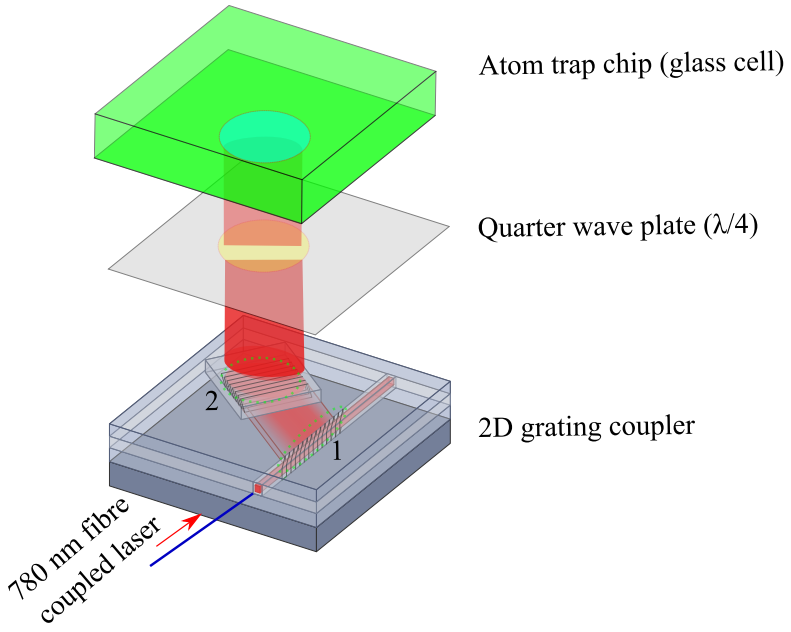

FIGURE 6.2: Expanded view of a proposed portable design for atom trap. It uses in-plane blazed Bragg grating (1) to input light into a large-area out-of-plane (OOP) 45° blazed grating (2). These two parts will be fabricated separately. The fabricated device will be bonded with a quarter wave plate and atom trap chip for integrated free space beam delivery.

6.5 COVID-19 impact

Experimental work disruptions repeatedly occurred throughout my PhD program due to COVID-19. I started my PhD program in the summer of 2019, and COVID-19 emerged worldwide the following winter. Due to the first COVID wave, the University was shut down immediately. The reopening and induction to get back into the building took three months (March to June 2020) to get me into building 53. After reopening, the labs I required access to, the UV laser writing lab and optical characterisation lab, were heavily used by the senior group members who required priority access to complete their work. In such cases, it was not always possible to access facilities when needed due to the restriction of single-person occupancy. The booking system partially helped, and I managed to get in the lab once or twice a week but sometimes not for the whole week. With the ease of COVID restrictions, guidelines were changed to two-person occupancy in the lab, which made it possible to accelerate my work. But, due to the second COVID wave (November 2020 to February 2021), lab occupancy returned to a single person again.

In the mid of 2021, the laser system at the core of my project started to degrade. Despite having a maintenance contract with the manufacturer (based in Germany), in-person maintenance was not possible due to the spike in 3rd COVID wave. This resulted in delays in establishing the components at fault – this took approximately two months. Due to the uncertainty from COVID and eventually the complete failure of the laser, we shipped the laser system back to the manufacturer company, Xiton, in Germany. The repair, shipping and re-installation took a further five months (November 2021-March 2022) – longer than expected due to extended lead times on replacement components due to COVID closures. Once laboratory work restarted, we observed variations in the

device fabrication parameters due to changes in laser beam dimension, spatial profile and beam quality. An additional two months were spent recalibrating and resolving the device parameters. This significantly slowed the progress toward validating the theory and models developed during the initial phase of my project. In August 2022, I contracted COVID the impact was great due to my pre-existing health condition (asthma). I had to stay home for four weeks and did not manage to work due to high temperature, shortness of breath and low oxygen saturation level. All these extended delays due to experimental faults and COVID-related hurdles have significantly affected my practical work and progress towards completion. In total, I have lost 13 months of lab work time.

If experimental disruptions and delays could have been avoided, I would have likely been able to demonstrate a complete and efficient device for circular 1 cm^2 Gaussian beam for integrated free-space beam delivery.

6.6 References

[1] M. Gagné and R. Kashyap, "New nanosecond Q-switched Nd:VO_4 laser fifth harmonic for fast hydrogen-free fiber Bragg gratings fabrication," *Optics Communications*, vol. 283, no. 24, pp. 5028–5032, 2010.

[2] C. Sima, J. C. Gates, H. L. Rogers, P. L. Mennea, C. Holmes, M. N. Zervas, and P. G. R. Smith, "Ultra-wide detuning planar Bragg grating fabrication technique based on direct UV grating writing with electro-optic phase modulation," *Optics express*, vol. 21, no. 13, pp. 15 747–15 754, 2013.

[3] S. Pissadakis and M. Konstantaki, "Grating inscription in optical fibres using 213 nm picosecond radiation: A new route in silicate glass photosensitivity," in *Proceedings of 2005 7th International Conference Transparent Optical Networks, 2005.*, IEEE, vol. 1, 2005, pp. 337–342.

Appendices

Appendix 1

FHD recipes

Wafer identifier number: PX 57 Fabricated at ORC			
Underclad	15 µm thermal oxide (Buffer layer)		
Core	Date	15/03/2018	
	Run number	PX57	
	Wafer position	2	
	Average refractive index – 1553 nm	1.4454	
	Average thickness	4.3 µm	
	Torch gas flows	H_2 O_2 Ar	5 5 8
	Process gas flow	$SiCl_4$ $GeCl_4$ PCl_3 BCl_3	60 21 - 22
Overclad	Date	16/03/2018	
	Run number	PX58	
	Wafer position	2	
	Average refractive index	1.4454	
	Average thickness	15.1 µm	
	Torch gas flows	H_2 O_2 Ar	6.5 1.5 8
	Process gas flow	$SiCl_4$ $GeCl_4$ PCl_3 BCl_3	137 - 31 70

Wafer identifier number: PX 194 Fabricated at ORC			
Underclad	15 μm thermal oxide (Buffer layer)		
Core	Date	10/09/2019	
	Run number	PX194	
	Wafer position	2	
	Average refractive index – 1553 nm	1.4485	
	Average thickness	3.3 μm	
	Torch gas flows	H_2	5
		O_2	5
		Ar	8
	Process gas flow	$SiCl_4$	60
		$GeCl_4$	23
		PCl_3	-
		BCl_3	20
Overclad	Date	17/09/2019	
	Run number	PX200	
	Wafer position	2	
	Average refractive index	1.4468	
	Average thickness	15.6 μm	
	Torch gas flows	H_2	6.5
		O_2	1.5
		Ar	8
	Process gas flow	$SiCl_4$	138
		$GeCl_4$	-
		PCl_3	31
		BCl_3	70

Wafer identifier number: PX 198 Fabricated at ORC			
Underclad	15 µm thermal oxide (Buffer layer)		
Core	Date	12/09/2019	
	Run number	PX198	
	Wafer position	2	
	Average refractive index – 1553 nm	1.4447	
	Average thickness	4.2 µm	
	Torch gas flows	H_2	5
		O_2	5
		Ar	8
	Process gas flow	$SiCl_4$	60
		$GeCl_4$	21
		PCl_3	-
		BCl_3	20.9
Overclad	Date	17/09/2019	
	Run number	PX200	
	Wafer position	2	
	Average refractive index	1.4468	
	Average thickness	15.6 µm	
	Torch gas flows	H_2	6.5
		O_2	1.5
		Ar	8
	Process gas flow	$SiCl_4$	138
		$GeCl_4$	-
		PCl_3	31
		BCl_3	70

Appendix 2

List of publications

Journal publications

- Paul C. Gow, **Q. Salman Ahmed**, Paolo L. Mennea, Rex H. S. Bannerman, Alexander Jantzen, Christopher Holmes, James C. Gates, Corin B. E. Gawith, and Peter G. R. Smith. "213 nm laser written waveguides in Ge-doped planar silica without hydrogen loading." **Optics Express** 28, no. 21 (2020): 32165-32172.

- Paul C. Gow, **Q. Salman Ahmed**, James C. Gates, Peter G. R. Smith, and Christopher Holmes. "Microwave consolidation of UV photosensitive doped silica for integrated photonics." **Optical Materials Express**, 11, no. 6 (2021):1835-1841

- **Q. Salman Ahmed**, Paul C. Gow, Christopher Holmes, Paolo L. Mennea, James W. Field, Rex H.S. Bannerman, Devin H. Smith, Corin B.E. Gawith, Peter G.R. Smith and James C. Gates. "Direct UV written waveguides and Bragg gratings in doped planar silica using a 213 nm laser." **Electronics Letters**, 57, no. 8 (2021):331-333

- Dong-Woo Ko, **Q. Salman Ahmed**, James W. Field, James C. Gates, and Peter Horak. "Out-of-plane beam shaping with UV-written tilted Bragg gratings for beam delivery on quantum chips." **Optics Express** 30, no. 25 (2022): 44628-44639.

- **Q. Salman Ahmed**, James W. Field, Christopher Holmes, Swe Zin Oo, Paolo L. Mennea, Rex HS Bannerman, Rod Cecil, Glenn Churchill, Corin B. E. Gawith, Peter G. R. Smith, Paul C. Gow, and James C. Gates. "Investigation into the writing dynamics of planar Bragg gratings using pulsed 213 nm radiation." **Optical Materials Express** 13, no. 2 (2023): 495-503.

Conferences proceedings

- Paul C. Gow, Rex H.S. Bannerman, Paolo L. Mennea, **Q. Salman Ahmed**, Christopher Holmes, Alexander Jantzen, James C. Gates, and Peter G.R. Smith. "Direct UV writing of integrated photonics devices with 213 nm laser light." Photonics Online Meetup 2020. 07 - 09 Jan 2020 (**Poster presentation**). .

- **Q. Salman Ahmed**, Paul C. Gow, P. L. Mennea, R. H. S. Bannerman, D. H. Smith, Christopher Holmes, James C. Gates, and Peter GR Smith. "Direct 213 nm UV written Bragg gratings and waveguides in planar silica without hydrogen loading." In Integrated Photonics Research, Silicon and Nanophotonics, pp. IW2A-4. Optical Society of America, 2020 (**Oral presentation**).

- Paul C. Gow, Christopher Holmes, **Q. Salman Ahmed**, James C. Gates and Peter. G. R. Smith. "Microwave Consolidation of Photosensitive Planar Glass Layers." In Integrated Photonics Research, Silicon and Nanophotonics, pp. IW2A-3. Optical Society of America, 2020 (**Oral presentation**).

- **Q. Salman Ahmed**, James W. Field, Paul C. Gow, Christopher Holmes, Dong-Woo Ko, Peter Horak, Corin B. E. Gawith, Peter GR Smith, and James C. Gates. "Holographically fabricated blazed gratings for out-of-plane coupling in integrated optics." In CLEO: Science and Innovations, pp. STh4P-3. Optica Publishing Group, 2022 (**Oral presentation**).

- **Q. Salman Ahmed**, James W. Field, Paul C. Gow, Christopher Holmes, Dong-Woo Ko, Peter Horak, Corin BE Gawith, Peter GR Smith, and James C. Gates. "Holographically fabricated blazed chirped gratings for out-of-plane integrated beam focusing." In Bragg Gratings, Photosensitivity and Poling in Glass Waveguides and Materials, pp. BTu1A-7. Optica Publishing Group, 2022 (**Oral presentation**).

- **Q. Salman Ahmed**, James W. Field, Paul C. Gow, Swe Zin Oo, Christopher Holmes, Rex H. S. Bannerman, Paolo L. Mennea, Corin B. E. Gawith, Peter G. R. Smith, and James C. Gates. "Photosensitivity response of pulsed 213 nm light in planar Bragg grating writing." In Bragg Gratings, Photosensitivity and Poling in Glass Waveguides and Materials, pp. BM3A-6. Optica Publishing Group, 2022 (**Oral presentation**).

- **Q. Salman Ahmed**, James W. Field, Paul C. Gow, Christopher Holmes, Rex H. S. Bannerman, Paolo L. Mennea, Corin B. E. Gawith, Peter G. R. Smith, and James C. Gates. "Investigation into multi-pass exposure of 213 nm pulsed UV writing for improved writing response." In Integrated Photonics Research, Silicon and Nanophotonics, pp. JTu2A-33. Optica Publishing Group, 2022 (**Poster presentation**).

- Paul C. Gow, Alexander Jantzen, **Q. Salman Ahmed**, James W. Field, Christopher Holmes, James C. Gates, and Peter GR Smith. "2D Holographic Transmission Gratings UV Written in a Suspended Silica Membrane." In Bragg Gratings, Photosensitivity and Poling in Glass Waveguides and Materials, pp. BTu1A-3. Optica Publishing Group, 2022 (**Oral presentation**).

- Dong-Woo KO, **Q. Salman Ahmed**, James W. Field, James C. Gates, and Peter Horak. "Efficiency of UV-written out-of-plane gratings for beam delivery on quantum chips." In Optical Devices and Materials for Solar Energy and Solid-state Lighting, pp. JTu2A-37. Optica Publishing Group, 2022 (**Poster presentation**).

- **Q. Salman Ahmed**, James W. Field, Dong-Woo Ko, Peter Horak, Christopher Holmes, Corin B. E. Gawith, Peter G. R. Smith, Paul C. Gow, and James C. Gates. "Holographically fabricated 2D grating coupler for integrated large beam delivery." In CLEO/Europe-EQEC 2023 (**Accepted for oral presentation**).

- **Q. Salman Ahmed**, James W. Field, Paul C. Gow, Christopher Holmes, Rex H. S. Bannerman, Paolo L. Mennea, Corin B. E. Gawith, Peter G. R. Smith, and James C. Gates. "Improved photosensitive response of doped silica to a 213 nm pulsed laser using a multi-pass writing approach. " In CLEO/Europe-EQEC 2023 (**Accepted for poster presentation**).

- Dong-Woo Ko, **Q. Salman Ahmed**, James W. Field, James C. Gates, and Peter Horak. "Arbitrary 3D beam delivery from planar optical waveguides for quantum technology." In CLEO/Europe-EQEC 2023 (**Accepted for poster presentation**).

- Rex H. S. Bannerman, James W. Field, **Q. Salman Ahmed**, Paul C. Gow, James C. Gates, Peter G. R. Smith, and Corin B. E. Gawith. "DUV laser written gratings on zinc doped lithium niobate waveguides". In CLEO/Europe-EQEC 2023 (**Accepted for oral presentation**).

Future papers

- **Q. Salman Ahmed**, James W. Field, Dong-Woo Ko, Peter Horak, Christopher Holmes, Corin B. E. Gawith, Peter G. R. Smith, Paul C. Gow, and James C. Gates. "Holographically fabricated blazed grating couplers for out-of-plane free space beam delivery." (**Drafting**).
- **Q. Salman Ahmed**, James W. Field, Dong-Woo Ko, Peter Horak, Christopher Holmes, Corin B. E. Gawith, Peter G. R. Smith, Paul C. Gow, and James C. Gates. "Holographically fabricated grating coupler for large-area integrated beam delivery." (**Drafting**).